Microstructural non-linear finite-element analysis of rat myocardium with hydrogel biomaterial inclusions

Uzair Manack

Supervisors: Dr. Benjamin Alheit, A/Prof. Malebogo Ngoepe

Thesis presented for the degree of
MASTER OF SCIENCE IN ENGINEERING

In the Department of Mechanical Engineering
UNIVERSITY OF CAPE TOWN

March 2025

Plagiarism Declaration

I, Uzair Manack, hereby declare that I know the meaning of plagiarism and declare that all the work in the document, save for that which is properly acknowledged, is my own. This thesis/dissertation has been submitted to the Turnitin module (or equivalent similarity and originality checking software) and I confirm that my supervisor has seen my report and any concerns revealed by such have been resolved with my supervisor.

Signed by candidate

Uzair Manack

Abstract

Hydrogel biomaterial injectate therapies have emerged as a promising treatment modality for myocardial infarction (MI). Studies conducted on small and large animal models have yielded positive results in improving cardiac function and reducing adverse ventricular remodelling post-MI. These therapies have also recently entered phase I and II human clinical trials, with limited positive results, but no significant adverse effects.

Computational modelling has been used extensively to investigate the potential effects of hydrogel injectate therapies, due to the risk-free and repeatable nature of these tests. Macroscale cardiac computational models are used to investigate the full-scale behaviour of the heart, while microscale models yield information on the behaviour of the cardiac microstructure. In order to reduce computational expense, many existing studies make use of idealisations regarding the macroscale or microscale cardiac geometry, as well as the physical behaviour of both the cardiac tissue and hydrogel injectate. The aim of the current study was to develop a computational framework that reduced the need for idealisations of the cardiac microstructural geometry, evaluated the validity of the assumption that both the cardiac tissue and hydrogel injectate could be described as elastic solids, and provided a basis for extension to more complex descriptions of material behaviour.

A realistic microstructural finite-element (FE) mesh was reconstructed from high-resolution confocal microscopy imaging data of rat myocardium. The reconstructed mesh did not necessitate idealisations of the cardiac tissue structure or the distribution of the hydrogel injectate. To investigate the mechanical response of the microstructure, under the assumption that both the cardiac tissue and hydrogel behaved as elastic solids, an FE solver was developed using the open-source FE library deal.II. The solver was capable of implementing both isotropic and anisotropic hyperelastic material models, and applying thermodynamically-admissible boundary conditions to the microstructure. Suitable boundary conditions were derived from the results of an existing macroscale FE model of rat myocardium, and used to investigate the mechanical response of the microstructure under five possible loading scenarios.

The results indicated that, under certain loading conditions, the observed stresses in the microstructure significantly exceeded reasonable elastic limits for the materials. This provides an indication that the assumption of elastic material behaviour is not always suitable when conducting *in silico* investigations of cardiac tissue and hydrogel injectate, and serves as a justification for the use of alternative descriptions of material behaviour. Furthermore, the framework was shown to be capable of implementing both static and time-dependent boundary conditions. This functionality provides the basis for the framework to be extended to more advanced models such as viscoelasticity and poroelasticity, which have been implemented in other studies using the deal.II library.

Acknowledgements

I would like to express my deepest gratitude to everyone who contributed to the completion of this thesis, without whom this work would not have been possible.

Firstly, I would like to thank my family: my sister Ammaarah Manack, my father Anwar Manack, and most especially my mother Dr. Fathima Peerbhay. Their constant encouragement and support, throughout the development of this thesis and the preceding coursework, were invaluable. Without their love and belief in me, this work would not have been possible.

Next I would like to thank my supervisors, Dr. Benjamin Alheit and Associate Professor Malebogo Ngoepe. Their expertise and guidance, both technical and personal, enabled the work presented in this thesis as well as my own personal and professional development. Your passion and dedication to your fields have served as a source of inspiration for me.

Thanks are also owed to Mark Trew, who is based at the Cardiac Structure and Imaging Group at the Auckland Bioengineering Institute, University of Auckland, New Zealand, for providing confocal imaging data of rat myocardium; and to Dodzi Motchon and Absalom Maluleke, for graciously providing the results of their PhD studies for use in this thesis.

Finally, I would like to thank Professor Arnaud Malan, who generously contributed to providing funding this project as part of his South African Research Chairs Initiative grant, through the National Research Foundation.

Contents

List of Figures

List of Tables

Chapter 1

Introduction and Literature Review

1.1 Problem identification

Cardiovascular disease (CVD) is the leading cause of death worldwide, with an estimated 17.9 million deaths due to CVD in 2019 alone (World Health Organization 2021). Deaths due to CVD represent approximately 32 % of global deaths, and 85 % of deaths due to CVD are the result of myocardial infarctions (heart attacks) and cerebrovascular accidents (strokes) (World Health Organization 2021). Furthermore, deaths in low- and middle-income countries represent more than 75 % of global deaths due to CVD (World Health Organization 2021). Projections of burden of disease estimate that by 2030, CVD will become the leading cause of death in low-income African countries, surpassing deaths due to HIV/AIDS (Celermajer et al. 2012), and that despite a decline in age-standardised CVD mortality rates, the overall number of CVD cases has continued to rise due to population growth and an ageing population (Nedkoff et al. 2023). Younger populations in developing countries are also disproportionately affected by CVD when compared to those of developed countries (Celermajer et al. 2012; Nedkoff et al. 2023). Furthermore, CVD is the leading cause of death in South Africa, with an estimated 85 525 fatalities in 2018 (of 452 345 deaths due to all causes), representing approximately 18.9 % of total deaths (World Heath Organization 2022). In 2020, there were an estimated 13 046 deaths due to acute myocardial infarction (MI) in South Africa (Statistics South Africa 2024), representing approximately 35 people per day. Ischaemic heart disease is forecasted to continue to be the leading cause of disease burden in the future (Institute for Health Metrics and Evaluation 2024).

Myocardial cell death as a result of prolonged ischaemia is the pathological definition of MI (Thygesen et al. 2018). Myocardial ischaemia occurs when inadequate blood flow leads to an imbalance between the supply and demand of oxygen to the myocardial tissue, and is the initial step in the development of MI (Thygesen et al. 2018). Ischaemia most commonly occurs due to the formation of atherosclerotic plaque (i.e. a blocking of the coronary arteries), or the erosion of the coronary artery endothelium (inner cellular lining) (Reed et al. 2017). Several factors affect the severity of ischaemia, including the nature of the vessel occlusion (partial or complete), the duration of the occlusion, and the amount of myocardial tissue supplied (Reed et al. 2017). Infarcted myocardium experiences a behavioural change from being active and contractile, to being passive and non-contractile, immediately after occlusion (Kortsmit et al. 2013). A resulting remodelling of the infarcted and non-infarcted myocardium takes place, however this process often fails to restore complete heart function, and may result in end-stage heart failure (Kortsmit et al. 2013). Furthermore, ventricular dilation occurring as a result of adverse remodelling is worsened by a positive feedback loop with increasing left ventricle (LV) wall stresses (Kortsmit et al. 2013). Despite recent treatment advances, acute MI is still responsible for more than a third of annual deaths in developed nations and, globally, affects more than 7 million individuals per year (Reed et al. 2017).

Current treatments for MI include reperfusion and revascularisation therapies, both of which aim to restore blood flow to ischaemic tissue. The two most prominent forms of reperfusion therapy are Fibrinolytic Therapy (FT) and Primary Percutaneous Coronary Intervention (P-PCI) (Reddy et al. 2015). FT involves the use of medications, more specifically thrombolytic agents, to induce fibrinolysis and dissolve clots (Reed et al. 2017; Cleveland Clinic 2022). P-PCI, also known as coronary angioplasty, is a surgical procedure wherein a balloon-tipped catheter is inserted into a blocked artery and used to unblock the artery while allowing for the placement of a stainless-steel mesh, known as a stent (NHS n.d.). P-PCI improves blood flow through the vessel and is considered a superior treatment to FT, however, not all hospitals are capable of performing P-PCI (Reddy et al. 2015). In recent decades, reperfusion therapies have been progressively improved, and in-hospital mortality due to acute MI has declined from 15 % to around 7.5 % (Braunwald 2012). However, there are issues facing reperfusion therapies, as despite reducing ischaemic cell death, it can also cause injury to the surviving myocardium (Braunwald 2012). This can occur through a number of paradoxical tissue responses (Kalogeris et al. 2016), or by the development of the so-called "no reflow" phenomenon, whereby normal blood flow to the tissue is not restored, despite there no longer being any vessel obstruction (Annibali et al. 2022). The primary form of revascularisation therapy is coronary artery bypass grafting (CABG), an invasive surgery whereby a piece of a healthy blood vessel is used to bypass a blocked vessel (John Hopkins Medicine n.d.). Given the limitations and risks associated with reperfusion and revascularisation therapies, alternative approaches have been investigated.

Biomaterial injectate therapies and stem cell therapies have gained attention in recent years as alternatives to currently available MI treatments (Henning 2012; Reddy et al. 2015; Y. Zhu et al. 2017; Ashammakhi et al. 2019; T. Wu et al. 2022). Heart failure therapies using intramyocardially-injected biomaterials have reached phase II clinical trials (Y. Zhu et al. 2017), and have been shown to limit adverse LV remodelling following MI (Sabbah et al. 2013) and improve cardiac function (Singelyn et al. 2012). One major advantage of biomaterial therapies is their minimally invasive nature, reducing the risk of complications as well as reducing costs (Ashammakhi et al. 2019). Additionally, stem cell therapies aiming to regenerate damaged myocardial tissue have been investigated, with mixed results from clinical trials (Henning 2012; Reddy et al. 2015). Ongoing research focuses on using different types of stem cells, and optimal delivery parameters (Henning 2013; Yan et al. 2024). Combinatorial therapies, wherein cellular therapies are combined with biomaterial therapies, are also the subject of ongoing research (L. L. Wang et al. 2017; Ashammakhi et al. 2019). Despite these advancements, *in vivo* studies are often constrained by ethical concerns, high costs, and limited experimental control, while *in vitro* studies may not fully capture whole-organism behaviour (Colquitt et al. 2011). *In silico* models, which use computational models to investigate pharmacological and physiological processes, aim to address these limitations by enabling controlled, repeatable, and cost-effective simulations (Colquitt et al. 2011).

The use of computational models in investigating MI therapies allows for an understanding of the underlying heart mechanics, specifically, how biomaterial injectate therapies affect cardiac function (Legner et al. 2014). Risk-free testing, repeatability of testing, and the ability to isolate specific physiological mechanisms represent advantages of *in silico* modelling over *in vivo* and *in vitro* experiments (Owen et al. 2018). Furthermore, medical imaging techniques can be used to develop patient-specific models and assist in planning therapies (Haddad et al. 2018).

The need for accurate and reliable cardiovascular computational models, many of which use the finite-element (FE) method, has been a major research focus in recent decades (Wall et al. 2006; Wenk et al. 2011; Kortsmit et al. 2013; Legner et al. 2014; Haddad et al. 2018; Owen et al. 2018). Despite significant advancements, these models still face many limitations, in part due to the complex geometrical, multi-physics, and multi-scale nature of the behaviour of the cardiovascular system.

1.2 Biomaterial injectate therapies for MI

1.2.1 Background

Biomaterial injectate therapies have gained attention in the past two decades as an alternative to currently available treatments for MI. The first investigation into the effects of biomaterial injectate alone (i.e. without cellular additions) was conducted by Christman et al. (2004), showing a reduction in LV wall thinning and improved cardiac function in rat specimens when using a fibrin glue biomaterial injectate. Subsequent studies on small animal models yielded similar results in limiting adverse LV remodelling and improving cardiac function (Dai et al. 2005; Landa et al. 2008; Kadner et al. 2012; Singelyn et al. 2012; Wassenaar et al. 2016). Furthermore, studies conducted on large animal models (porcine, canine, and ovine) reported a reduction in infarct scar tissue (Bastings et al. 2014), and improved LV wall thicknesses and function (Sabbah et al. 2013; Seif-Naraghi et al. 2013; Dorsey et al. 2015; Rodell et al. 2016). Biomaterial injectate therapies have also entered phase I and II human clinical trials (Frey et al.

2014; Y. Zhu et al. 2017; Sedlakova et al. 2024).

Various types of biomaterial injectates have been investigated in terms of their impact on improving cardiac function following MI. These materials can be grouped into three main categories: natural-based hydrogels, synthetic hydrogels, and hybrid (i.e. a combination of natural and synthetic) hydrogels (Sepantafar et al. 2016). Natural-based hydrogels encompass materials derived from natural sources such as fibrin (Christman et al. 2004), collagen (Dai et al. 2005), alginate (Landa et al. 2008), Matrigel (Kofidis et al. 2005), hyaluronic acid (Ifkovits et al. 2010), chitosan (Lu et al. 2009), and decellularised extracellular matrices (dECM) (Singelyn et al. 2012). Synthetic hydrogels refer to those fabricated using synthetic polymers such as polyethylene glycol (PEG), polycaprolactone (PCL), polyvinyl alcohol (PVA), and polylactic acid (PLA) among others (Lin et al. 2009; Asti et al. 2014). Studies have also made use of a combination of natural and synthetic hydrogels, for example PEG combined with: collagen (Singh et al. 2013), gelatine (Fu et al. 2012), fibrinogen (Martino et al. 2013), hyaluronic acid (Skaalure et al. 2014), and alginate (Jeon et al. 2014). ECM-polyethylene glycol (Grover et al. 2014), ECM-fibrin (Williams et al. 2015), and alginate-chitosan (Deng et al. 2015) are further examples of hybrid hydrogels.

Many parameters involved in the application of hydrogel injectate therapies have been investigated in recent research. For example, Kadner et al. (2012) showed that the timing of the injectate delivery affects the remodelled cardiac structure. Hydrogel delivered immediately after infarction showed no observable improvements, while hydrogel delivered one week after infarction resulted in a reduction in adverse LV remodelling and an improvement in cardiac function (Kadner et al. 2012). Furthermore, using a finite-element model of a rat heart, Wise et al. (2016) indicated the possible existence of a threshold injectate volume above which biomaterial injections hinder, rather than aid, therapeutic effects. The optimal mechanism for biomaterial delivery is also of interest. Biomaterial cardiac patches have been shown to improve cardiac function in rat and porcine specimens (Huang et al. 2020), however application of these patches usually requires invasive surgery (D. Zhu et al. 2021). To overcome this limitation, alternative delivery routes such as epicardial (direct injection onto the outer surface of the heart), intracoronary (delivery via the coronary arteries), and endocardial (injection into the heart muscle using a catheter) injections have been explored (Johnson et al. 2013; Saludas et al. 2017).

1.2.2 Natural biomaterials

Biomaterials derived from natural sources have the advantages of high bioactivity, biocompatibility, and biodegradability (Sepantafar et al. 2016; Li et al. 2019). However, the disadvantages of natural biomaterials include lower mechanical strength, the potential for batch-to-batch variations, and the possibility of inducing an immune response (Hasan et al. 2015). Sedlakova et al. (2024) identified 23 clinical trials conducted between 2012 and 2022, all of which made use of natural biomaterials. Of the 23 clinical trials identified by Sedlakova et al. (2024), 16 made use of alginate-based materials, a natural hydrogel commonly used in studies investigating biomaterial therapies for MI.

Alginate biomaterial injectates have also been utilised in small and large animal models (Johnson et al. 2013). Landa et al. (2008) used an alginate-based material injected into rat specimens 7 days after infarction and observed a significant increase in scar tissue thickness, in addition to a reduction in adverse cardiac remodelling. Similarly, Leor et al. (2009) and Sabbah et al. (2013) tested alginate biomaterial injectates in porcine and canine specimens, respectively, and both reported a reduction in adverse LV remodelling after treatment.

1.2.3 Synthetic biomaterials

A major advantage in using synthetic hydrogels is the level of control available over their composition and physical properties (Tous et al. 2011; Saludas et al. 2017). Properties such as tensile strength, elastic modulus, and degradation rate can be predicted and reproduced under controlled conditions (Asti et al. 2014). However, synthetic biomaterials are less likely to promote tissue regeneration as compared to natural biomaterials, resulting from lower levels of bioactivity (Do et al. 2015; Saludas et al. 2017). Furthermore, although many synthetic polymers are considered biocompatible and have been approved by the Food and Drug Association for certain human applications (Place et al. 2009; Saludas et al. 2017), they are still considered less satisfactory compared to natural biomaterials (Sarig et al. 2011; Sepantafar et al. 2016), and are more likely to trigger inflammatory responses (Nelson et al. 2011).

Of the polymers commonly used in the development of synthetic hydrogels, PEG is particularly notable for its versatility and excellent biocompatibility (Saludas et al. 2017). However, investigations into injection therapies involving the use of PEG hydrogel alone have yielded limited positive results (Dobner et al. 2009; Rane et al. 2011; Kadner et al. 2012; Johnson et al. 2013). Dobner et al. (2009), using PEG hydrogel injected into infarcted regions in male Wistar rats, observed reduced adverse remodelling 2- and 4-weeks following MI; however, 3 months following MI, the remodelling had progressed to be in-line with the control sample. Similarly, Rane et al. (2011) used PEG hydrogel injectate in female Sprague Dawley rats, delivered 1 week after total occlusion of the left coronary artery, and observed an increase in infarct wall thickness compared to the control. However, cardiac function in both the polymer and control groups decreased compared to the baseline (Rane et al. 2011). Kadner et al. (2012), using male Wistar rats, observed that PEG hydrogel delivered 1 week after MI resulted in a significant increase in infarct scar thickness and a reduction in pathological remodelling. Other studies have made use of PEG copolymers and yielded beneficial results (Jiang et al. 2009; T. Wang et al. 2009a; J. Wu et al. 2011; Johnson et al. 2013). For example, J. Wu et al. (2011) observed a significant preservation of scar thickness, a reduction in pathological remodelling, and an improvement in ventricular function, when using a PEG copolymer injectate delivered 1 week after MI in Sprague Dawley rat specimens.

1.2.4 Hybrid biomaterials

Hybrid hydrogels combine the advantages of both natural and synthetic hydrogels, thereby allowing for the provision of biological properties as well as controlled mechanical strength and degradation profiles (Xu et al. 2015). Several studies have developed various types of hybrid hydrogels for biological applications (Fu et al. 2012; Martino et al. 2013; Singh et al. 2013; Grover et al. 2014; Jeon et al. 2014; Skaalure et al. 2014; Deng et al. 2015; Williams et al. 2015). For example, Grover et al. (2014) synthesized a hybrid biomaterial using porcine dECM and PEG hydrogel. The incorporation of PEG hydrogel increased the stiffness and decreased the degradation rate of the resulting biomaterial, while still allowing for the material to be injectable (Grover et al. 2014).

1.2.5 Factors affecting distribution and retention of biomaterial injectate

Several studies have identified low levels of biomaterial retention following injectate therapies for MI as a subject of interest (Hou et al. 2005; George et al. 2008; Hale et al. 2008; Nakamuta et al. 2009; Le Visage et al. 2012; Rustad et al. 2012). In particular, the optimal cell delivery route and optimal injection timing have been identified as potentially important factors (Nakamuta et al. 2009). For example, Hou et al. (2005) investigated the effect of peripheral blood mononuclear cells delivered to infarcted porcine models through intramyocardial (IM), intracoronary (IC) and intravenous (IV) delivery routes. The study concluded that the majority of the delivered cells were not retained within the heart for all delivery modalities, with a significant percentage of the cells being distributed to the lungs (Hou et al. 2005). Nakamuta et al. (2009) made use of bone marrow cells delivered to adult rats via 4 different routes. The study observed that the IM delivery route led to improved cardiac cell retention as compared to the remaining 3 delivery routes (Nakamuta et al. 2009). Furthermore, when the IM injection was performed 7 days after MI, the observed cell retention was significantly improved compared to injections 1, 2, and 3 days after MI (Nakamuta et al. 2009). Additionally, when using an IM injection performed 3 days after MI, the inclusion of an injectable fibrin polymer scaffold led to a 2.5 times increase in the number of transplanted cells retained in the myocardium 24 hours after injection (Nakamuta et al. 2009). Kadner et al. (2012) focused on the effects of injection timing, using a PEG hydrogel injected into infarcted rat specimens both immediately and 7 days after MI. The study concluded that only the delayed delivery resulted in a reduction in adverse cardiac remodelling and an improvement in cardiac function (Kadner et al. 2012). Similarly, studies investigating delayed hydrogel injections delivered in rabbits 4 days after MI (T. Wang et al. 2009b), and rats 2 weeks after MI (Fujimoto et al. 2009), observed clear improvements in cardiac function and ejection fraction. These findings highlight the importance of optimising both the delivery route and timing of biomaterial injections to enhance retention and improve therapeutic outcomes for MI.

1.2.6 Challenges in understanding the mechanism of action of hydrogel injectate therapies

Despite promising outcomes from investigations into the use of hydrogel injection therapies as a treatment for MI, the underlying mechanism of action remains unclear (Sack et al. 2020). This lack of understanding restricts the ability of translational research to refine and adapt therapy protocols in a way that maximises their potential effectiveness (Sack et al. 2020). Sack et al. (2020) provides an excellent example of the value of *in silico* modelling approaches in investigating the complex interactions between hydrogel biomaterial and the cardiac environment into which it is injected. The *in silico* models developed in their study were able to realistically simulate *in vivo* function with $> 99\,\%$ accuracy and suggested that the solidified hydrogel provides support to the LV mid-wall, substantially reducing adverse remodelling when compared to the untreated control (Sack et al. 2020). As noted by Quarteroni et al. (2017), modelling the cardiovascular system presents significant challenges due to its complexity, multi-scale dynamics, and the demand for stable, reliable, and efficient computational methods.

1.3 Computational modelling of cardiac mechanics

1.3.1 Background

The heart is comprised of a mixture of various biological components, including muscle fibres, collagen fibres, coronary vessels, blood, and interstitial fluid (Mackerle 2005). Furthermore, the series of pressure changes that occur within the heart, known as the cardiac cycle, can be divided into diastole (ventricular filling) and systole (ventricular contraction) (Pollock et al. 2017), and the heart can be decomposed into mechanically active (contractile) and passive components (Lamata et al. 2014). As a result of this complexity, numerical simulation of the cardiovascular system is not a simple problem (Mackerle 2005). However, there is significant promise that the combination of novel hierarchical continuum models, new imaging modalities, and modern simulation tools will provide greater understanding into the pathways of cardiac disease and guide the design of new treatment methodologies (Göktepe et al. 2010).

The method of approach to computational cardiovascular mechanics used by Guccione et al. (2010), consists of four major steps. First, the studying of the anatomy of the heart to determine its geometric configurations. Second, the determination of the mechanical properties of the cardiovascular tissue. Third, the derivation of the necessary partial differential or integral governing equations from the laws of physics, continuum mechanics, and the constitutive equations of the cardiovascular tissue. And fourth, the understanding of the boundary conditions of the heart (Guccione et al. 2010). Each step incurs its own challenges, for example, in determining the mechanical properties of cardiovascular tissue: the tissue is unable to be isolated for testing, the size of available tissue specimens is too limited, and there is difficulty in maintaining the tissue in its normal living condition (Guccione et al. 2010). Furthermore, cardiovascular tissue exhibits anisotropic and non-linear stress-strain relationships. Nevertheless, constitutive models have been proposed that are motivated by the microstructure of the myocardium (Holzapfel et al. 2009), and parameters for such models have been estimated using data from *ex vivo* experiments (Sommer et al. 2015; Guan et al. 2019). As per Guccione et al. (2010), once the boundary value problem has been posed at the end of the approach, mathematical and computational algorithms can be used to find an approximate solution. Validation of the models can then be done using various experimental approaches, such as imaging-based approaches for patients. Should the models and the experiments disagree, the cause of the discrepancy then needs to be examined, and the theory, or the experiment, or both, may be improved. This results in an iterative process wherein the improvements in experiment and theory continue until there is an acceptable agreement between the two. If the computational models and experimental results are in agreement, the model can then be used in predicting the system's physiological behaviour under different conditions (Guccione et al. 2010). The following section elaborates on the issues of geometry development and constitutive modelling necessary for this approach.

1.3.2 Geometry development

A major breakthrough in cardiac computational modelling came in the development of new imaging modalities able to provide structural and functional information of cardiac tissue (Lopez-Perez et al. 2015). Imaging modalities such as echocardiography, cardiac magnetic resonance imaging (MRI), and computed tomography (CT) have seen dramatic improvements in their capabilities and rapid expansion of their applications in recent years (Lamata et al. 2014). Refinements in these medical imaging methods have vastly improved our ability to image manifestations of cardiovascular disease (Wann et al. 2010). These imaging methods provide a significantly safer and easier route for detecting various heart conditions in comparison to invasive techniques (Blankstein 2012).

The development of realistic cardiac models from *in vivo* or *ex vivo* information has been made possible through the evolution of medical imaging modalities (Lopez-Perez et al. 2015). For example, advancements in MRI and diffusion tensor MRI (DT-MRI) technologies have led to a new level of anatomically accurate cardiac models (Gurev et al. 2011; Sack et al. 2016; Sack et al. 2018). MRI and DT-MRI are able to detail an individual heart's ventricular geometry, in addition to fibre and laminar sheet structure (Helm et al. 2005; Gurev et al. 2011). The need to balance the accuracy of a model with computational expense considerations often leads to anatomical simplifications (Sack et al. 2016). Simplified LV geometries, such as those used by (Janz et al. 1972; Streeter et al. 1973; Arts et al. 1979) were, until recently, the primary tool used to investigate cardiac mechanics (Sack et al. 2016). The development of the first realistic biventricular model was done by Nielsen et al. (1991), this model was then extended by Stevens et al. (2003) (Sack et al. 2016). The first full heart model, featuring all four chambers of the heart, the four valves, and connecting large vessels, was developed by the Living Heart Project (Baillargeon et al. 2014; Sack et al. 2016).

Cardiac geometry and function also depend on the contribution of features at a vast range of length-scales, including the cellular (10 µm to 100 µm), mesostructural (100 µm to 1 mm), and whole-organ (1 mm to 100 mm) levels (Wilson et al. 2022). To address these complexities, studies such as Wilson et al. (2022) and Motchon et al. (2023) have adopted a microstructural modelling approach. Sirry et al. (2013) developed a detailed microstructural geometry of myocardium with PEG hydrogel inclusions, reconstructed from cardiac MRI data. Motchon et al. (2023) made use of *ex vivo* microcomputed tomography (µCT) imaging data to develop a whole-organ scale finite-element geometry, followed by the extraction of a tissue block which was used for microstructural computational studies.

In recent years, patient-specific modelling, involving the development of individualised computational models based on patient-specific data, has gained research attention due to its potential to improve diagnosis, inform surgical training platform design, and optimise clinical treatments by predicting therapeutic and surgical treatment outcomes (Neal et al. 2010; Sack et al. 2016).

1.3.3 Constitutive modelling

Constitutive models describe the mechanical behaviour of materials through the use of mathematical models derived using physical concepts and experimental evidence (Marino 2019). The predictive capabilities of computational models significantly depend on the accuracy of constitutive models (Marino 2019). Moreover, two of the main components of a patient-specific cardiovascular model are the constitutive models used for the active and passive materials (Krishnamurthy et al. 2013).

For passive cardiac behaviour, the most widely used constitutive law, as per Sack et al. (2016), was developed by Holzapfel et al. (2009), wherein the following strain energy function Ψ is proposed:

$$\Psi = \underbrace{\frac{a}{2b}\exp[b(I_1-3)]}_{\text{isotropic term}} + \underbrace{\sum_{i=f,s}\frac{a_i}{2b_i}\left\{\exp[b_i(I_{4i}-1)^2]-1\right\}}_{\text{anisotropic term}} + \underbrace{\frac{a_{fs}}{2b_{fs}}\left\{\exp[b_{fs}I_{8fs}^2]-1\right\}}_{\text{coupling term}}.$$

Here, a and b terms are material parameters and I terms are invariants of the right Cauchy-Green tensor defined in Equation (2.2.8). In particular, I_1 is an isotropic term, while I_{4i} represents the stretch of anisotropic component i and I_{8fs} represents the interaction of anisotropic components f and s. This was the first model that was completely invariant-based, orthotropic, convex, and characterized by microstructurally motivated material parameters (Göktepe et al. 2010). Homogenous simple shear tests, using explanted cardiac tissue, have been used to demonstrate the excellent performance of this model (Dokos et al. 2002; Holzapfel et al. 2009; Göktepe et al. 2010).

The most common approach, as per Sack et al. (2016), to incorporating the active contractile cardiac behaviour into a mathematical description was introduced by Guccione et al. (1993). The approach relies on the contribution of the active stress to the overall stress being additive, usually along the local fibre orientation (Sack et al. 2016). The proposed model considers (among other factors) sarcomere length, time after onset of contraction, intracellular calcium concentration, and maximum isometric tension. In this model, the active tension in the myocardium is given by:

$$T_0 = T_{\max} \underbrace{\frac{Ca_0^2}{Ca_0^2 + ECa_{50}^2}}_{\text{calcium concentration}} C_t, \quad C_t = \underbrace{\frac{1}{2}(1 - \cos\omega)}_{\text{contraction time}} .$$

Where $T_{\max}$ is the maximum isometric tension, Ca_0 is the peak intracellular calcium concentration, and ECa_{50} is the length-dependent calcium sensitivity. The internal variable C_t scales the tension evolution, with ω as a time-dependent phase variable governing the contraction cycle.

In the event of MI, cardiac muscle tissue is lost and replaced with scar tissue; the mechanical properties of this scar tissue play an important part in cardiac function post-infarction (Fomovsky et al. 2010). In a study conducted over 12 weeks in infarcted porcine models, McGarvey et al. (2015) noted that average infarct stiffness was approximately 20 times that of normal passive myocardium when measured 1 week after MI. The same study noted that, 12 weeks after MI, the infarct stiffness had decreased to approximately 3 times that of normal passive myocardium (McGarvey et al. 2015). Sack et al. (2018) introduced a constitutive model capable of describing both healthy and failing porcine cardiac specimens, through the introduction of a parameter representing the volume fraction of healthy tissue. The resulting model allows for homogenised, pathological tissue to be described using an isochoric (volume-preserving) strain energy function $\bar{\Psi}$, and a volumetric (shape-preserving) strain energy function Ψ_{vol} (Sack et al. 2018):

$$\bar{\Psi} = \underbrace{\frac{\bar{a}}{2b}\exp[b(\bar{I}_1 - 3)]}_{\text{isotropic term}} + \underbrace{\sum_{i=f,s} \frac{\bar{a}_i}{2b_i}\left\{\exp[b_i(\bar{I}_{4i} - 1)^2] - 1\right\}}_{\text{anisotropic term}} + \underbrace{\frac{\bar{a}_{fs}}{2b_{fs}}\left\{\exp[b_{fs}\bar{I}_{8fs}^2] - 1\right\}}_{\text{coupling term}},$$

$$\bar{a}_i = a_i \underbrace{[h + (1 - h)p]}_{\text{pathological scaling}} ,$$

$$\Psi_{\text{vol}} = \underbrace{\frac{1}{D}\left(\frac{J^2 - 1}{2} - \ln(J)\right)}_{\text{volumetric term}} .$$

Where J is the determinant of the deformation gradient given by Equation (2.2.3), and the $\bar{I}$ terms are the invariants of the isochoric right Cauchy-Green tensor defined in Equation (2.2.8). The $\bar{a}_i$ terms represent parameters governing healthy and pathological tissue homogenisation, with h representing the volume fraction of healthy tissue, and p scaling the passive response based on pathology. The b terms are material parameters contributing to the isotropic and anisotropic stiffness responses, and D is a material parameter which defines material compressibility.

1.4 Computational mechanics in MI and biomaterial therapies

The finite-element (FE) method has been shown to be a useful tool in modelling cardiac mechanics, and in investigating many parameters needed to optimise biomaterial injection therapies, such as biomaterial properties, injection volume, injection location, and injection timing (Kortsmit et al. 2013). Computational models have been used to describe the mechanical effects of biomaterial injection, due to the complexities and limitations associated with real-time, *in vivo* measurements (Y. Zhu et al. 2017). For example, Wall et al. (2006), using an FE model of an infarcted ovine LV, investigated the short-term effect of material injection on cardiac function as a function of injectate volume, injectate stiffness, and injection location. The study found that fractional changes (0.5 to 5%) in myocardial wall thickness resulting from injection may help to reduce myofibre stresses, and that this effect was most pronounced with multiple border wall zone injections, as well as dependent on injectate volume and stiffness (Wall et al. 2006).

Many studies have investigated the importance of injection patterns and injectate distribution in biomaterial injection therapies (Wenk et al. 2009; Kortsmit et al. 2013; Miller et al. 2013; Kortsmit et al. 2014).

Wenk et al. (2009) developed an FE-based method which aimed to automatically optimise injection patterns based on an objective function with various weighting factors. In the study, the injected material was represented using spherical polymeric inclusions embedded into the myocardium (Wenk et al. 2009). Using FE models, Kortsmit et al. (2013) investigated the effects of a more realistic, layered biomaterial distribution on cardiac function. Kortsmit et al. (2014) and Miller et al. (2013) compared the effects of both layered and bulk distributions. Kortsmit et al. (2014) found that layered and bulk distributions decreased average myofibre stress by 99 % and 97 %, respectively, during the ischaemic stage, and by 70 % and 36 %, respectively, during the remodelling stage. The study also found that LV ejection fraction increased by 77 % (layered distribution) and 25 % (bulk distribution) during the ischaemic stage, and by 61 % (layered distribution) and 63 % (bulk distribution) during remodelling (Kortsmit et al. 2014).

Further studies have investigated the impact of biomaterial injectate therapies on myocardial stresses (Kichula et al. 2014; Lee et al. 2014; Legner et al. 2014; H. Wang et al. 2017). Kichula et al. (2014) conducted biomaterial injection experiments in ovine LV myocardium, and used MRI techniques to generate data on the resulting injection volume and shape. This information was then implemented in an FE model used to investigate myocardial wall stresses (Kichula et al. 2014). The resulting simulations showed an approximate 14 % reduction in global average fibre stress, and an approximate 26 % reduction in the transmural (representing a local change in stress) average as a result of the injections (Kichula et al. 2014). H. Wang et al. (2017) focused on the effects of injection stiffness and volume on ventricular wall thickness and stress. Their results indicated that larger volumes and higher stiffnesses resulted in the greatest stress reduction, although improvements appeared to taper once the biomaterial stiffness reached 50 kPa (H. Wang et al. 2017). Wise et al. (2016) used a rat heart FE model in investigating the effects of injectate volume and infarct size on treatment efficiency, and hypothesized the existence of an optimal biomaterial volume or volume range dependent on infarct size. The results of the study found that an increase in injection volume from 25 % to 50 % of the infarct wall volume increased the beneficial effects on ventricular function and infarct wall mechanics (Wise et al. 2016). However, these beneficial effects did not increase further when the volume was increased to 75 % (Wise et al. 2016). The study concluded that a threshold volume may exist, beyond which treatment efficacy does not further increase, but may in fact decrease. They further concluded that the efficacy of biomaterial injectates in reducing infarct wall stresses increased with infarct size (Wise et al. 2016).

There are promising benefits to patient-specific models, including personalised diagnosis, treatment planning, and therapy design (Sack et al. 2016). Significant advancements in patient-specific computational cardiac mechanics include high-quality imaging techniques, increases in computational resources, geometrically realistic multi-physics models, and more easily available structural and functional data of the heart (Sack et al. 2016). However, a patient-specific, high-resolution computational cardiac model using data from an individual patient has not yet been developed (Sack et al. 2016).

1.5 Rationale

Accurately modelling the geometrical features of the cardiac system presents significant challenges, some of which have been identified in the preceding sections. As a result, many studies make use of idealisations when modelling cardiac structures and hydrogel injectate inclusions. These simplifications reduce computational expenses and model complexities, however they also reduce the accuracy and predictive capabilities of these models. Further challenges exist due to the multi-scale nature of the cardiac system, where the cardiac microstructure varies considerably across the whole-organ scale. These microstructural variations lead to difficulties in accurately simulating the full-scale behaviour of the heart, and often lead to additional simplifications in existing literature. Additional complexity exists in the multi-physics nature of cardiac function, which includes, among others, fields such as fluid dynamics, solid mechanics, and electrophysiology. Consequently, many existing studies focus on certain aspects of this multi-physics behaviour, which again reduces model complexity at the cost of model accuracy and predictive capacity. Owen et al. (2018), Morris et al. (2016), and Trayanova et al. (2023) provide reviews of cardiovascular computational models which focus on solid mechanics, fluid mechanics, and electrophysiology, respectively.

Additional limitations exist in modelling the behaviour of hydrogel injectate, which is comprised of both solid and fluid constituents (Feng et al. 2020). This results in material behaviour that is neither completely fluid-like, nor completely solid-like. Many studies avoid this complexity by analysing the injectate as either a non-Newtonian fluid, as seen in Ngoepe et al. (2019), or as a hyperelastic solid, as seen in Motchon et al. (2023). Few studies analyse the intermediate behaviour of the injectate during the gelation process, or the potential of the injectate, post-gelation, to behave as a viscoelastic material. A poroelastic material model, described in Feng et al. (2020), has demonstrated the most complete ability so far in describing the behaviour of hydrogel injectate, however this model has not yet seen use in any cardiovascular computational modelling studies.

Ideally, a comprehensive model of the cardiac system would capture both macroscale and microscale geometric detail, as well as the multi-physics interactions between solid mechanics, fluid mechanics, and electrophysiology. However, such a model is not currently feasible, both in terms of the complexity of its development, as well as the computational resources that would be required to use it. A more practical approach is to begin with the simplest possible model, by making use of idealisations, and to systematically assess the conditions under which those idealisations become inadequate. The limits of these idealisations can then be addressed by incrementally adding additional levels of complexity to the model, until the predictions made by the model are in acceptable agreement with observed experimental results.

Given the uncertain nature of the behaviour of hydrogel injectate in cardiac tissue, it would be useful to have a modelling framework that initially assumes elastic material behaviour, while providing a basis for extension to more complex descriptions of material behaviour such as viscoelasticity and poroelasticity. Such a framework would allow investigation into whether the assumption of elastic material behaviour is sufficient, and if it is not, under which conditions the observed stresses exceed reasonable elastic limits. This would provide a clear rationale for incorporating more complex material models if necessary, ensuring a balance between accuracy and computational efficiency.

1.6 Aims and objectives

Aims

The broad goal of this work is to develop a computational framework for modelling the mechanical effects of hydrogel injectate accurately, beginning with the simplifying assumption of elastic material behaviour. The framework should aim to improve upon the current state of the art by:

1. Using geometric descriptions of the injectate that are not idealisations but, rather, are direct reconstructions from medical imaging data;
2. Incorporating appropriate non-linear material models for the myocardium and hydrogel;
3. Applying boundary conditions that are representative of the cardiac cycle and well founded in thermodynamic principles.

Additionally, the framework should be implemented in such a way that it is extensible and can be further developed to include, for example, poroelasticity, electrophysiology, and new constitutive models. This way, as the state of the art in myocardial modelling advances, the framework can be extended to incorporate these advancements.

Objectives

To achieve these aims, the following objectives have been formulated:

1. To develop a representative microstructural geometry comprised of myocardium and hydrogel injectate.
2. To implement isotropic and anisotropic hyperelastic material models, which allow for the variation of material parameters.
3. To develop appropriate boundary conditions which can be used to replicate the actions of the cardiac cycle.
4. To demonstrate the capabilities of the developed framework using a range of input conditions.

Chapter 2

Methodology

The following chapter details the methodologies employed in addressing the objectives of this study. To investigate the mechanical response of a myocardium tissue block with hydrogel inclusions under various loading conditions, a modelling framework was developed. Detail will be provided regarding the following aspects of the development of this framework:

1. The development of microstructural finite-element meshes which can be used for *in silico* modelling purposes. These include a realistic microstructural mesh derived from confocal microscopy imaging data of rat myocardium, as well as an idealised mesh representing a myocardial tissue block with a cylindrical hydrogel inclusion.
2. The development of a finite-element solver which was capable of incorporating non-linear hyperelastic material models, applying thermodynamically-admissible boundary conditions, and solving problems with multiple material domains.
3. An application example which demonstrated the utility of the developed framework, by using boundary conditions which were derived from the results of an existing, macroscale, *in silico* cardiac model. A parametric study was conducted spanning a range of possible loading conditions, as well as a range of possible hydrogel injectate material parameters.

Ethical considerations

The methods of the present study did not include any interactions with human participants or the use of any data, experimental or otherwise, related to human participants. Furthermore, the methods of the study do not involve the collection of data from animal specimens in any way, and instead make use of secondary data which has been made available to the research group (CERECAM). In cases where third-party, secondary data was permitted to be used, the originators were properly acknowledged and accredited. This includes the confocal microscopy imaging dataset made available by Sands et al. (2005), as well as the results of the macroscale FE model made available by Motchon et al. (2023) and Absalom Maluleke (unpublished PhD study).

2.1 Geometry development

2.1.1 Background on the multi-scale structure of cardiac tissue

In the case of cardiac tissue, there are heterogeneities that occur at a length scale far smaller than that of the entire cardiac structure. The directions of the cardiac muscle fibres (cardiomyocytes) and the structures of the laminar sheets are examples of these heterogeneities that can be identified at the microstructural level, as seen in Figure 2.1. Certain anisotropic material models, such as the one proposed by Holzapfel et al. (2009), make use of a right-handed orthonormal set of basis vectors comprised of a fibre axis $\boldsymbol{f}_0$, coinciding with the orientation of the cardiomyocytes, a sheet axis $\boldsymbol{s}_0$, which lies in the plane of the cardiomyocyte layer and is perpendicular to the fibre axis, and a sheet-normal axis $\boldsymbol{n}_0$, which is orthogonal to the other two axes.

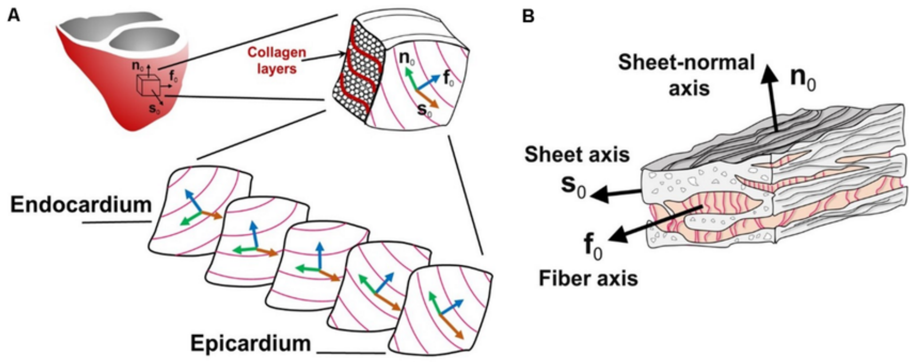

Figure 2.1: Schematic diagram of the microstructural organisation of cardiac tissue showing: (A) the variation in muscle fibre orientation and laminar sheet structure across the heart wall and (B) the layered organisation of cardiomyocytes and the collagen fibres between them, with a right-handed orthonormal co-ordinate system consisting of a fibre axis $\boldsymbol{f}_0$, sheet axis $\boldsymbol{s}_0$, and sheet-normal axis $\boldsymbol{n}_0$ (Nguyen et al. 2020).

Of relevance to this study is the fact that the left ventricular wall is primarily comprised of cardiomyocytes, which occupy approximately 70 % of the volume, with the remaining 30 % consisting of various interstitial components (Holzapfel et al. 2009). LeGrice et al. (1995) found that adjacent cardiomyocytes are bound together by collagen fibres to form laminar sheet structures, which are separated by cleavage planes, as illustrated in Figure 2.2.

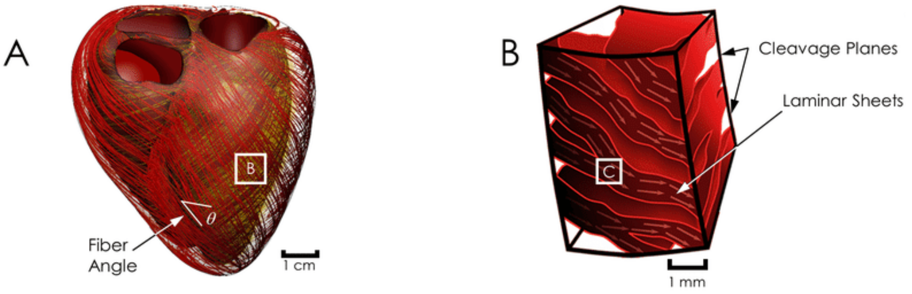

Figure 2.2: Schematic diagram of: (A) the biventricular cardiac anatomy with fibre orientations, (B) a myocardial tissue block illustrating the arrangement of cardiomyocytes into laminar sheets separated by cleavage planes (Miller et al. 2022).

In this study, two assumptions were made with regard to the nature of the cardiac structure at the 100 µm to 1 mm level, in order to facilitate the development of a finite-element mesh and a corresponding set of orthonormal basis vectors needed for anisotropic material models:

1. The cleavage planes were assumed to be “void” regions where hydrogel biomaterial could potentially settle post-injection. A similar assumption was made by Ngoepe et al. (2019). This assumption is further supported by Pope et al. (2008), which found that collagen cords in the cardiac mid-wall appear to be sparsely distributed.

2. The mean fibre axis $\boldsymbol{f}_0$ and sheet-normal axis $\boldsymbol{n}_0$ directions were assumed to correspond with the longest and shortest axes of the cleavage planes respectively. This assumption was supported by the findings of Wilson et al. (2022).

2.1.2 Description of available confocal microscopy data

The geometry used for the simulations conducted in this study was derived from *ex vivo* confocal microscopy imaging data of a rat heart tissue block, provided by the University of Auckland (Sands et al. 2005). In their study, a tissue block from the left ventricular wall of the heart was examined, resulting in a set of 2D image slices. A visualisation of the entire tissue block, reconstructed from these slices, is shown in Figure 2.3. The tissue block has dimensions of 4.25 mm, 1.12 mm, and 0.88 mm in the radial, longitudinal, and circumferential directions respectively.

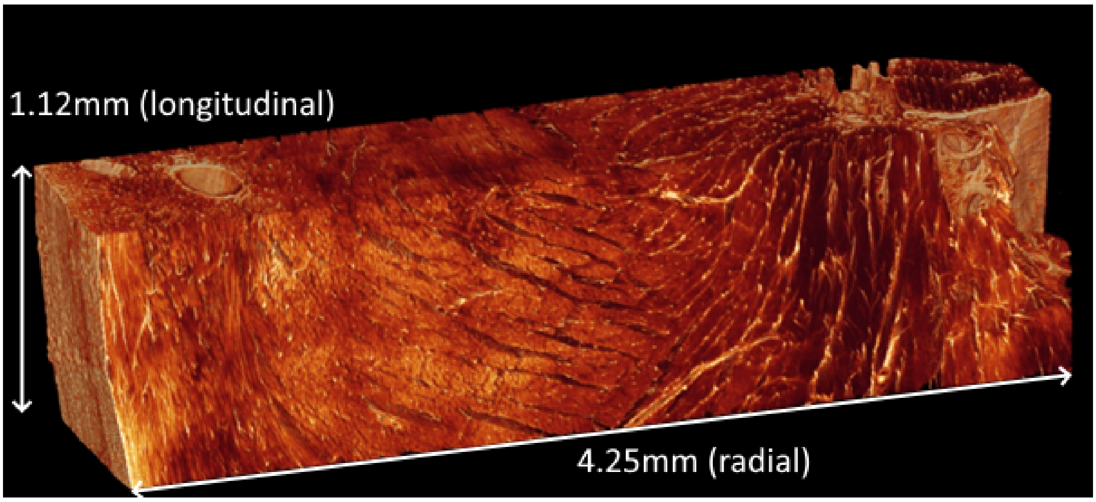

Figure 2.3: Reconstruction of the original 3D micro-CT imaging dataset (Sands et al. 2005).

The dataset is comprised of 365 2D greyscale images, each with pixel intensity values ranging from 0 (black) to 255 (white). An example of a single image from the dataset can be seen in Figure 2.4. The tissue block was assumed to be comprised of two material domains: one in which myocardial tissue is present and one in which myocardial tissue is not present. The latter of these domains describes both interstitial cavities in the tissue block, such as the cleavage planes, as well as internal blood vessels.

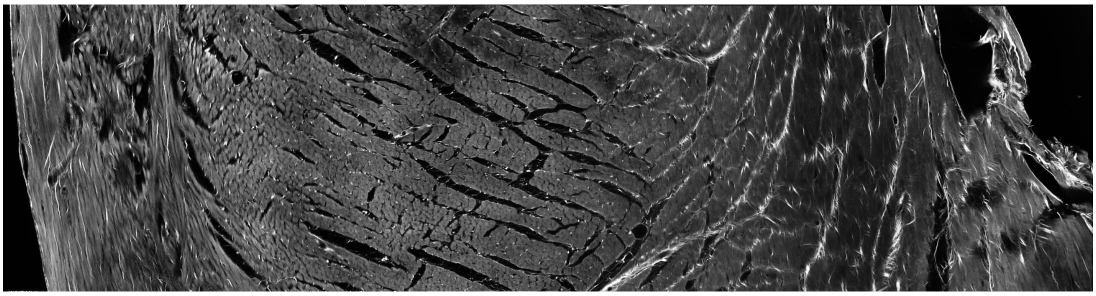

Figure 2.4: Example of a single 2D image slice from the Sands et al. (2005) dataset.

The imaging data does not directly contain descriptions of the material domains, nor does it contain descriptions of the orientations of the fibre $\boldsymbol{f}_0$, sheet $\boldsymbol{s}_0$ or sheet-normal $\boldsymbol{n}_0$ axes. As such, additional processing was needed to obtain reasonable descriptions of the material domains and the directions of the axes. Furthermore, the imaging dataset does not include a precise description of the location of the extracted tissue block within the LV wall; as a result, the orientation of the tissue block and its position relative to the full cardiac geometry were not considered in this study.

2.1.3 Development of a realistic microstructural mesh from confocal microscopy imaging data

In order to develop a finite-element mesh from the available confocal microscopy image dataset, it was necessary to segment each image to determine the myocardial tissue and void regions. This was accomplished by preprocessing the set of 2D images and then investigating two image segmentation techniques: global thresholding and region-growing.

Preprocessing

This study chose to focus on the laminar sheet structure of myocardial tissue, which features cleavage planes where hydrogel injectate could potentially settle. To do so, the 2D images were cropped to focus on a region of interest (ROI) which captured the laminar sheet structure of the tissue block. Additionally, to aid the segmentation process, the contrast of each image was improved using Contrast Limited Adaptive

Histogram Equalisation (CLAHE). This was done using the built-in CLAHE functionality of the open-source image processing library OpenCV; the authors of this library have asked for it to be cited as (Bradski 2000).

Image segmentation techniques

Following the preprocessing of the images, global thresholding and region-growing segmentation techniques were investigated in order to distinguish the myocardium and void regions. What follows is a description of each technique, as well as their main advantages and disadvantages.

Global thresholding using the Otsu method

As per Jardim et al. (2023), one of the simplest techniques used to segment an image into two regions is thresholding, where the image is split into two groups of pixels: those with values below the threshold and those with values equal to or above it. Their paper identified the Otsu method as one of the most commonly used forms of global thresholding, whereby the threshold value is determined by maximising the variance between pixel intensity classes. They further noted that this method performs well when the pixel values in the image have a bimodal distribution, but struggles in cases where the image features noise or inhomogeneous lighting (Jardim et al. 2023). Implementation of Otsu global thresholding was accomplished using the built-in functionality of the OpenCV library.

Region-growing segmentation

Region-growing segmentation is a commonly used technique whereby image regions are distinguished based on pixel intensity and edge information (Alzahrani et al. 2021). This involves the selection of a set of seed points in the original image, which are then grown iteratively according to a predefined similarity criterion. The neighbouring pixels of each seed point are evaluated against the similarity criterion. If they satisfy the criterion, they are said to belong to the region of the seed point and their own neighbouring pixels are then checked. This process continues until no more pixels satisfy the similarity criterion for region expansion. Region-growing techniques work well in identifying areas of the image with similar characteristics, and perform better on images with obvious edges (Jasim et al. 2021). However they can be computationally demanding and sensitive to noise in the image data (Jasim et al. 2021).

This study implemented a region-growing segmentation algorithm using the built-in functionality of the OpenCV library. Seed points were selected using a global thresholding method where all pixels with a value below 15 were selected as seed points. The similarity criterion used was a pixel intensity difference of 50; if a pixel's intensity differed from its neighbour's intensity by more than this amount, it was not added to the region. The seed point threshold value and similarity criterion were determined through trial-and-error, and aimed to ensure adequate coverage of major cleavage planes while preventing excessive region growth.

Mesh generation using segmented imaging data

Image segmentation provided a set of 2D binary images comprised of detected void regions and detected tissue regions, with pixel intensity values of 0 (black) and 1 (white) respectively. These images were stacked to form a 3D image dataset containing 106 762 500 voxels (from 365 2D slices, each being 650 by 450 pixels). To reduce the number of finite elements needed for full representation, and to ensure that the simulations described in Section 2.3.2 were computationally feasible, the 3D image dataset was truncated to be of size 160 by 160 by 160 pixels, reducing the size of the dataset to 4 096 000 voxels. As stated previously, the assumption was made that void regions had been filled with hydrogel following an injection of hydrogel material into the cardiac area. A finite-element mesh was then generated from the truncated 3D image dataset, using the mesh generation capabilities of the open-source C++ library deal.II, described in Section 2.2.2. Each cell of the mesh corresponded to a voxel of the truncated 3D image dataset, and the myocardial tissue regions and hydrogel regions were distinguished using deal.II cell material identifiers.

The generated realistic microstructural mesh had a size of 160 cells in the x, y, and z directions. This corresponds to dimensions of 0.386 mm in each of the longitudinal, radial, and circumferential directions of the original tissue block seen in Figure 2.3.

Myocardial fibre directions

Implementation of the anisotropic, hyperelastic material model proposed by Holzapfel et al. (2009) required the definition of the fibre axis $\boldsymbol{f}_0$, sheet axis $\boldsymbol{s}_0$, and sheet-normal axis $\boldsymbol{n}_0$. It was then necessary to determine an appropriate set of axes, corresponding to the generated finite-element microstructural mesh. For this purpose, the mean fibre directions within the geometry were assumed to be aligned with the longest axes of the cleavage planes (i.e. hydrogel injectate regions), as per Wilson et al. (2022).

In determining appropriate fibre directions, a larger subset of the segmented, binarised 3D image dataset was used. This subset was of size 352 by 352 by 352 pixels, and provided information on the orientations of the cleavage planes over a larger domain than the one used to develop the previously described finite-element mesh.

The geometry of the cleavage planes was analysed using its two-point correlation function $\mathcal{S}$; that is:

$$\mathcal{I}\left(\boldsymbol{x}\right) = \begin{cases} 1 & \text{if } \boldsymbol{x} \text{ in cleavage plane}\,, \\ 0 & \text{otherwise}\,, \end{cases} \qquad \mathcal{S}\left(\boldsymbol{r}\right) = \frac{1}{|\Omega|}\int_{\Omega} \mathcal{I}\left(\boldsymbol{x}\right)\mathcal{I}\left(\boldsymbol{x}+\boldsymbol{r}\right)\,\mathrm{d}\Omega\,. \tag{2.1.1}$$

Here, $\mathcal{I}$ is the indicator function and $\boldsymbol{r}$ is the shift vector. Further detail on two-point correlation functions and their use in describing aggregate features in heterogenous materials can be found in Torquato et al. (2002, Sec. 2.2.5). This function provides the probability that two points with relative position $\boldsymbol{r}$ will both be located in the cleavage planes if placed randomly in the microstructure. Intuitively, points connected by a shift vector $\boldsymbol{r}$ that is parallel with the longest axis of the cleavage planes are most likely to both be located in a cleavage plane, and the converse is true for $\boldsymbol{r}$ that is parallel with the shortest axis of the cleavage planes. This was used to determine the statistically longest and shortest directions of the cleavage planes, which were assumed to correspond to the $\boldsymbol{f}_0$ and $\boldsymbol{n}_0$ axes, respectively. To do so, $\boldsymbol{r}$ was defined in terms of spherical co-ordinates; that is:

$$\boldsymbol{r} = \begin{bmatrix} r\sin\left(\theta\right)\cos\left(\phi\right) \\ r\sin\left(\theta\right)\sin\left(\phi\right) \\ r\cos\left(\theta\right) \end{bmatrix}\,, \tag{2.1.2}$$

And the orientation of $\boldsymbol{f}_0$ and $\boldsymbol{n}_0$, respectively, was found using:

$$\left(\theta,\phi\right)_{\boldsymbol{f}_0} = \underset{\theta,\phi}{\arg\max}\int_{-w}^{w}\mathcal{S}\left(\boldsymbol{r}\left(r,\theta,\phi\right)\right)\,\mathrm{d}r\,, \qquad \left(\theta,\phi\right)_{\boldsymbol{n}_0} = \underset{\theta,\phi}{\arg\min}\int_{-w}^{w}\mathcal{S}\left(\boldsymbol{r}\left(r,\theta,\phi\right)\right)\,\mathrm{d}r\,. \tag{2.1.3}$$

Here, $\left(\theta,\phi\right)_{\boldsymbol{f}_0}$ and $\left(\theta,\phi\right)_{\boldsymbol{n}_0}$ are the orientations of $\boldsymbol{f}_0$ and $\boldsymbol{n}_0$, respectively, and w is a user-chosen bandwidth; chosen here as $w = 10$ pixels. Finally, the sheet axis $\boldsymbol{s}_0$ was calculated as the cross-product of the $\boldsymbol{f}_0$ and $\boldsymbol{n}_0$, since the fibre axes must form an orthonormal set:

$$\boldsymbol{s}_0 = \boldsymbol{f}_0 \times \boldsymbol{n}_0\,. \tag{2.1.4}$$

The resulting orthonormal set of fibre directions was determined to be:

$$\boldsymbol{f}_0 = \begin{bmatrix} -0.95199538 \\ 0.30601061 \\ -0.00789337 \end{bmatrix}\,, \quad \boldsymbol{n}_0 = \begin{bmatrix} 0.33220323 \\ 0.87674863 \\ -0.34778276 \end{bmatrix}\,, \quad \boldsymbol{s}_0 = \begin{bmatrix} 0.09950472 \\ 0.33370978 \\ 0.93631836 \end{bmatrix}\,. \tag{2.1.5}$$

2.1.4 Development of an idealised mesh

In addition to the realistic microstructural mesh, an idealised mesh was developed, representing a myocardial tissue block with a cylindrical hydrogel injectate inclusion. The simplified mesh was developed to allow for a wider range of the developed program's capabilities to be demonstrated in the application example (Section 2.3), such as the ability to apply a set of time-varying boundary conditions. Demonstration of this capability using the realistic microstructural mesh was not feasible, due to the number of degrees-of-freedom and the consequent computational time requirements.

The idealised mesh was comprised of 163 840 elements and 513 315 corresponding degrees-of-freedom, and was of unit length, width, and height. The diameter of the cylindrical inclusion was set as half the overall width. Since the idealised mesh was not derived from any form of imaging data, the mesh does not have any corresponding real-world dimensions. It is important to note that this mesh was highly idealised for demonstration purposes, and was not intended to represent a realistic cardiac microstructure.

2.2 Finite-element solver development

The following section provides a description of the finite-element solver which was developed as part of this study. The solver makes use of the open-source C++ finite-element library, deal.II, whose authors have asked for it to be cited as Arndt et al. (2021) and Africa et al. (2024). Detail will be provided with regard to the following:

1. The theoretical preliminaries necessary for the development of the solver. These include essential descriptions of the relevant continuum mechanics, finite-element, and computational homogenisation theory.

2. An overview of the deal.II C++ library, which is open-source and available free of charge for private, academic, and commercial use under the GNU Lesser General Public License (Arndt et al. 2021; Africa et al. 2024).

3. A description of the finite-element solver which was developed in this study.

2.2.1 Theoretical preliminaries

The following section provides essential descriptions of the theory required to develop the solver, as well as descriptions of the notation used in this study. It is important to note that the descriptions provided in this section are summarised and are not intended to represent an in-depth treatment of all of the relevant theory. Essential kinematic descriptions and notations are presented, followed by the definition of the boundary value problem (BVP) that was relevant to this study. The variational form of the equilibrium equation is then presented, followed by its linearised, discretised form. Subsequently, the relevant constitutive modelling theory is covered, regarding isotropic and anisotropic constitutive models which make use of an isochoric (volume preserving) and volumetric (shape preserving) split of the deformation gradient. Finally, the purpose and essential principles of computational homogenisation are provided, including a description and justification for kinematically uniform boundary conditions (KUBCs) which are used throughout the remainder of this study.

Continuum mechanics

<u>Kinematics</u>

Each point $\boldsymbol{X}$ in the ***material domain*** of a body $\Omega_0 \subset \mathbb{R}^3$ is mapped to a unique point $\boldsymbol{x}$ in the ***current domain*** $\Omega \subset \mathbb{R}^3$ at a given time t by the ***motion*** $\varphi\left(\boldsymbol{X}, t\right)$. The displacement $\boldsymbol{u}$ and deformation gradient $\boldsymbol{F}$ are then defined, respectively, as:

$$\boldsymbol{u} := \boldsymbol{x} - \boldsymbol{X}\,, \qquad \boldsymbol{F} := \frac{\partial \varphi}{\partial \boldsymbol{X}}\,. \tag{2.2.1}$$

The Jacobian J is defined as the ratio of an infinitesimal volume element in the current domain $\mathrm{d}v$ to its counterpart in the material domain $\mathrm{d}V$; that is:

$$J := \frac{\mathrm{d}v}{\mathrm{d}V}\,. \tag{2.2.2}$$

Furthermore, it can be shown that:

$$J = \det\left(\boldsymbol{F}\right)\,. \tag{2.2.3}$$

It is occasionally useful to multiplicatively decompose the deformation gradient $\boldsymbol{F}$ into an isochoric part $\bar{\boldsymbol{F}}$ and a volumetric part $\boldsymbol{F}_{vol}$. This allows for the separation of the isochoric and volumetric parts of the behaviour of a material, which will be discussed in further detail in Section 2.2.1 - "Constitutive modelling". The isochoric component of the deformation gradient $\bar{\boldsymbol{F}}$ is volume preserving, and as such the determinant of $\bar{\boldsymbol{F}}$ is necessarily equal to one.

$$\boldsymbol{F} = \boldsymbol{F}_{vol}\bar{\boldsymbol{F}}\,, \tag{2.2.4}$$

$$\boldsymbol{F}_{vol} := J^{\frac{1}{3}}\boldsymbol{I}\,, \tag{2.2.5}$$

$$\bar{\boldsymbol{F}} := J^{-\frac{1}{3}}\boldsymbol{F}\,, \tag{2.2.6}$$

$$\det\left(\bar{\boldsymbol{F}}\right) = 1\,. \tag{2.2.7}$$

The right Cauchy-Green tensor $\boldsymbol{C}$ and its isochoric counterpart $\bar{\boldsymbol{C}}$ are defined, respectively, as:

$$\boldsymbol{C} := \boldsymbol{F}^T\boldsymbol{F}\,, \qquad \bar{\boldsymbol{C}} := \bar{\boldsymbol{F}}^T\bar{\boldsymbol{F}}\,. \tag{2.2.8}$$

Additionally, the following shorthand expressions for various gradient terms are defined:

$$\mathrm{Grad}\,(\bullet) : = \frac{\partial \bullet}{\partial \boldsymbol{X}}\,, \qquad \mathrm{grad}\,(\bullet) : = \frac{\partial \bullet}{\partial \boldsymbol{x}} \tag{2.2.9}$$

$$\mathrm{Div}\,(\bullet) : = \frac{\partial \bullet_i}{\partial X_i}\,, \qquad \mathrm{div}\,(\bullet) : = \frac{\partial \bullet_i}{\partial x_i}\,. \tag{2.2.10}$$

Here, and throughout the study the Einstein summation convention on repeated indices is invoked.

Boundary value problem definition

In the absence of traction boundary conditions and inertial and body forces, the displacement $\boldsymbol{u} \in H^1$ can be solved for by satisfying the following equations:

$$\text{Equilibrium:} \qquad \mathrm{div}\,(\boldsymbol{\sigma}) = \boldsymbol{0} \qquad \text{on } \Omega\,, \tag{2.2.11}$$

$$\text{Dirichlet BC:} \qquad \boldsymbol{u} = \bar{\boldsymbol{u}} \qquad \text{on } \Gamma\,, \tag{2.2.12}$$

$$\text{Constitutive equation:} \qquad \boldsymbol{\sigma} = \hat{\boldsymbol{\sigma}}\,(\mathrm{Grad}\,(\boldsymbol{u})) \qquad \text{on } \Omega\,. \tag{2.2.13}$$

Here, Equation (2.2.11) is the point-wise equilibrium equation that must be satisfied on the entire domain, Equation (2.2.12) represents prescribed displacement values $\bar{\boldsymbol{u}}$ on the boundary Γ, and Equation (2.2.13) defines the material response through a constitutive law relating stress to the deformation gradient.

In order to find an approximate solution the problem represented by Equations (2.2.11) to (2.2.13) the problem was first cast into a functional form, using methods as described in Bonet et al. (2008), to arrive at the following:

$$\delta w = \int_{\Omega} \mathrm{grad}\,(\delta \boldsymbol{v}) : \boldsymbol{\sigma}\,\mathrm{d}\Omega = 0\,. \tag{2.2.14}$$

Here, δw is 'virtual work' and $\delta \boldsymbol{v}$ is the 'virtual velocity'. It can be shown that, when $\boldsymbol{u}$ is sufficiently smooth, finding $\boldsymbol{u}$ that satisfies Equation (2.2.14) for all $\delta \boldsymbol{v} \in \{\boldsymbol{q} |\, \boldsymbol{q} \in H^1,\, \boldsymbol{q}|_\Gamma = \boldsymbol{0}\}$ is equivalent to solving the original BVP given by Equations (2.2.11) to (2.2.13).

In order to find approximate solutions to Equation (2.2.14) using the finite-element method, this study makes use of a Newton-Raphson iterative scheme. In preparation for this, the following linearisation is introduced:

$$\mathrm{L}\delta w\,[\Delta \boldsymbol{u}] = \delta w + \mathrm{D}\delta w\,[\Delta \boldsymbol{u}]\,, \tag{2.2.15}$$

Where:

$$\mathrm{D}\delta w\,[\Delta \boldsymbol{u}] = \int_{\Omega_0} \left[\mathrm{grad}\,(\Delta \boldsymbol{u})^T\,\mathrm{grad}\,(\delta \boldsymbol{v})\right] : \boldsymbol{\tau} + \mathrm{grad}_s\,(\delta \boldsymbol{v}) : \mathbb{c} : \mathrm{grad}_s\,(\Delta \boldsymbol{u})\,\mathrm{d}\Omega_0\,, \tag{2.2.16}$$

And:

$$\mathrm{grad}_s\,(\bullet) := \frac{1}{2}\left[\mathrm{grad}\,(\bullet) + \mathrm{grad}\,(\bullet)^T\right]\,. \tag{2.2.17}$$

The Kirchhoff stress tensor $\boldsymbol{\tau}$, and spatial elasticity tensor $\mathbb{c}$ are defined in Equations (2.2.25) to (2.2.27), and Equations (2.2.33) to (2.2.35), respectively.

Finite-element discretisation

The solution, increment in solution, and virtual velocity are then approximated as a linear combination of piecewise defined shape functions ϕ multiplied by nodal values; that is:

$$\boldsymbol{u} \approx \sum_i \phi_i \boldsymbol{u}^i \,, \qquad \Delta\boldsymbol{u} \approx \sum_i \phi_i \Delta\boldsymbol{u}^i \,, \qquad \delta\boldsymbol{v} \approx \sum_i \phi_i \delta\boldsymbol{v}^i \,, \tag{2.2.18}$$

Where $\bullet^i$ denotes a nodal value. The gradients of these fields are then accordingly approximated as:

$$\operatorname{grad}(\boldsymbol{u}) \approx \sum_i \boldsymbol{u}^i \otimes \operatorname{grad}(\phi_i) \ , \tag{2.2.19}$$

$$\operatorname{grad}(\Delta\boldsymbol{u}) \approx \sum_i \Delta\boldsymbol{u}^i \otimes \operatorname{grad}(\phi_i) \ , \tag{2.2.20}$$

$$\operatorname{grad}(\delta\boldsymbol{v}) \approx \sum_i \delta\boldsymbol{v}^i \otimes \operatorname{grad}(\phi_i) \ . \tag{2.2.21}$$

In order to find an approximate solution to Equation (2.2.14) a Newton-Raphson scheme is used; this is done by substituting Equations (2.2.19) to (2.2.21) into Equation (2.2.15) and iteratively solving for $\Delta\boldsymbol{u}$ that sets Equation (2.2.15) to zero $\forall\,\delta\boldsymbol{v}$. Since $\delta\boldsymbol{v}$ is arbitrary, this is equivalent to finding $\Delta\boldsymbol{u}$ that satisfies:

$$\begin{aligned} \boldsymbol{0} = & \underbrace{\int_{\Omega_0} \boldsymbol{\tau} \operatorname{grad}(\phi_i) \, \mathrm{d}\Omega_0}_{\delta w} \\ & + \underbrace{\sum_j \int_{\Omega_0} \left[\left[\operatorname{grad}(\phi_i) \cdot \boldsymbol{\tau} \operatorname{grad}(\phi_j) \right] \boldsymbol{I} + \operatorname{grad}(\phi_i) \cdot \mathbb{c} \cdot \operatorname{grad}(\phi_j) \right] \, \mathrm{d}\Omega_0 \Delta\boldsymbol{u}^j}_{\mathrm{D}\delta w[\Delta\boldsymbol{u}]} \ . \end{aligned} \tag{2.2.22}$$

Where: Ω_0 represents the undeformed domain, $\boldsymbol{\tau}$ represents the second-order Kirchhoff stress tensor, $\operatorname{grad}(\phi)$ represents the shape function gradient with respect to the directions of the spatial configuration, $\boldsymbol{I}$ represents the second-order identity tensor, $\mathbb{c}$ represents the fourth-order spatial elasticity tensor, and $\Delta\boldsymbol{u}$ represents the change in the displacement solution for the current iteration of the non-linear solution.

Constitutive modelling

In addition to Equation (2.2.22) which results from the equilibrium equation we require constitutive laws relating the stress and strain behaviours of a given material. The combination of the set of governing equations and the constitutive equations allows us to form a complete boundary value problem from which we can determine all unknown quantities using the FE method (Alheit 2022).

The calculation of the Kirchhoff stress tensor $\boldsymbol{\tau}$ and the spatial elasticity tensor $\mathbb{c}$ depends on the constitutive model chosen for the relevant material. The domain chosen for this study is comprised of myocardial tissue and hydrogel, and as such a constitutive model must be chosen for each. The myocardial tissue was treated using an isochoric-volumetric split variation of the anisotropic hyperelastic constitutive model presented in Holzapfel et al. (2009), which has been widely adopted in literature when modelling the behaviour of passive myocardium (Sack et al. 2018). The present study did not include a description of the behaviour of active myocardium. The hydrogel was treated using an isochoric-volumetric split variation of an isotropic Neo-Hookean hyperelastic constitutive model; an approach also adopted by Wise et al. (2016). It then becomes necessary to derive the equations for computing the Kirchhoff stress tensor $\boldsymbol{\tau}$ and spatial elasticity tensor $\mathbb{c}$ for each of these constitutive models. This requires the calculation of the first and second scalar derivatives of the strain energy function with respect to the invariants. The following section provides an overview of the form of constitutive models which use an isochoric-volumetric split of the deformation gradient, and subsequently, the derivation of the Kirchhoff stress tensor and spatial elasticity tensor for the constitutive models used for the myocardium and hydrogel.

The material response of a given constitutive model is governed by a strain energy function in terms of the invariants of the right Cauchy-Green tensor, which has been defined in Equation (2.2.8):

$$\Psi = \Psi\left(\boldsymbol{C}\right) . \tag{2.2.23}$$

In the case of a constitutive model which uses an isochoric-volumetric split, the strain energy function is postulated as the superposition of an isochoric (volume-preserving) $\bar{\Psi}$ and volumetric (shape-preserving) Ψ_{vol} strain energy function. The isochoric strain energy function then depends only on the invariants of $\bar{\boldsymbol{C}}$, as defined in Equation (2.2.8), whereas the volumetric strain energy function depends only on the Jacobian J:

$$\Psi = \bar{\Psi}\left(\bar{\boldsymbol{C}}\right) + \Psi_{vol}\left(J\right) . \tag{2.2.24}$$

The Kirchhoff stress can then be calculated as the sum of an isochoric and volumetric component:

$$\boldsymbol{\tau} = \bar{\boldsymbol{\tau}} + \boldsymbol{\tau}_{vol} , \tag{2.2.25}$$

Where the isochoric and volumetric Kirchhoff stress are given by (Alheit 2022, Eq. 4.80) as:

$$\bar{\boldsymbol{\tau}} = 2 \sum_{\substack{m=1 \\ m\neq 3}}^{8} \frac{\partial \bar{\Psi}}{\partial \bar{I}_m} \left[\bar{\boldsymbol{A}}_m + q_m \bar{I}_m \boldsymbol{I} \right] , \tag{2.2.26}$$

$$\boldsymbol{\tau}_{vol} = J \frac{\partial \Psi_{vol}}{\partial J} \boldsymbol{I} . \tag{2.2.27}$$

Here q_m is defined such that the standard invariants are related to their isochoric counterparts as:

$$\text{(no sum)}\ \bar{I}_m = \det\left(\boldsymbol{C}\right)^{q_m} I_m , \tag{2.2.28}$$

leading to:

$$q_m := \begin{cases} -1/3 & m = 1, 4, 6, 8 , \\ -2/3 & m = 2, 5 , \\ 0 & m = 3, 9 . \end{cases} \tag{2.2.29}$$

When making use of an orthogonal co-ordinate system consisting of a fibre axis $\boldsymbol{f}_0$ and sheet axis $\boldsymbol{s}_0$, the isochoric invariants that were relevant to the present study are defined as:

$$\begin{aligned} \bar{I}_1 &:= \operatorname{tr}\left(\bar{\boldsymbol{C}}\right) , & \bar{I}_{4f} &:= \boldsymbol{f}_0 \cdot \bar{\boldsymbol{C}} \boldsymbol{f}_0 , \\ \bar{I}_{4s} &:= \boldsymbol{s}_0 \cdot \bar{\boldsymbol{C}} \boldsymbol{s}_0 , & \bar{I}_{8fs} &:= \boldsymbol{f}_0 \cdot \bar{\boldsymbol{C}} \boldsymbol{s}_0 . \end{aligned} \tag{2.2.30}$$

And the relevant isochoric second-order tensors $\bar{\boldsymbol{A}}_i$, are defined as:

$$\begin{aligned} \bar{\boldsymbol{A}}_1 &:= \bar{\boldsymbol{B}} , & \bar{\boldsymbol{A}}_{4f} &:= \boldsymbol{f} \otimes \boldsymbol{f} , \\ \bar{\boldsymbol{A}}_{4s} &:= \boldsymbol{s} \otimes \boldsymbol{s} , & \bar{\boldsymbol{A}}_{8fs} &:= \frac{1}{2} \left[\boldsymbol{f} \otimes \boldsymbol{s} + \boldsymbol{s} \otimes \boldsymbol{f} \right] , \end{aligned} \tag{2.2.31}$$

Where:

$$\begin{aligned} \boldsymbol{f} &= \boldsymbol{F} \boldsymbol{f}_0 , \quad \boldsymbol{s} = \boldsymbol{F} \boldsymbol{s}_0 , \\ \bar{\boldsymbol{B}} &= \boldsymbol{F} \boldsymbol{F}^T . \end{aligned} \tag{2.2.32}$$

In a manner similar to Equation (2.2.25), the spatial elasticity tensor can be calculated as the sum of an isochoric and volumetric component:

$$\mathbb{c} = \bar{\mathbb{c}} + \mathbb{c}_{vol} \,, \tag{2.2.33}$$

Where the isochoric and volumetric spatial elasticity tensors are given by (Alheit 2022, Eq. 4.61, Eq. 4.78) as:

$$\begin{aligned}\bar{\mathbb{c}} = 4 \sum_{\substack{m,n=1\\ m,n\neq 3}}^{8} \frac{\partial^2 \bar{\Psi}}{\partial \bar{I}_m \partial \bar{I}_n} \left[\bar{\boldsymbol{A}}_m \otimes \bar{\boldsymbol{A}}_n + q_m \bar{I}_m \boldsymbol{I} \otimes \bar{\boldsymbol{A}}_n + q_n \bar{I}_n \bar{\boldsymbol{A}}_m \otimes \boldsymbol{I} + q_m q_n \bar{I}_m \bar{I}_n \boldsymbol{I} \otimes \boldsymbol{I}\right] \\ + 4 \sum_{\substack{m=1\\ m\neq 3}}^{8} \frac{\partial \bar{\Psi}}{\partial \bar{I}_m} \left[\bar{\mathbb{A}}_m + q_m \left[\boldsymbol{I} \otimes \bar{\boldsymbol{A}}_m + \bar{\boldsymbol{A}}_m \otimes \boldsymbol{I} - \bar{I}_m \boldsymbol{I} \odot \boldsymbol{I}\right] + q_m^2 \bar{I}_m \boldsymbol{I} \otimes \boldsymbol{I}\right] \,,\end{aligned} \tag{2.2.34}$$

$$\mathbb{c}_{vol} = J \left[\frac{\partial \Psi_{vol}}{\partial J} + J \frac{\partial^2 \Psi_{vol}}{\partial J \partial J}\right] \boldsymbol{I} \otimes \boldsymbol{I} - 2J \frac{\partial \Psi_{vol}}{\partial J} \boldsymbol{I} \odot \boldsymbol{I} \,. \tag{2.2.35}$$

Here the symmetric tensor product $\odot$ is defined as:

$$\boldsymbol{A} \odot \boldsymbol{B} := \frac{1}{2} \left[A_{ik} B_{jl} + A_{jk} B_{il}\right] \boldsymbol{e}_i \otimes \boldsymbol{e}_j \otimes \boldsymbol{e}_k \otimes \boldsymbol{e}_l \,. \tag{2.2.36}$$

And the relevant isochoric fourth-order tensors are defined as:

$$\bar{\mathbb{A}}_p := \mathbb{0} \,, \quad p = 1, 4f, 4s, 8fs \,. \tag{2.2.37}$$

Hydrogel constitutive model

The isotropic Neo-Hookean hyperelastic constitutive model used for the hydrogel has the following isochoric $\bar{\Psi}$ and volumetric Ψ_{vol} strain energy functions, where G and D are material parameters:

$$\bar{\Psi} = G \left[\bar{I}_1 - 3\right] \,, \tag{2.2.38}$$

$$\Psi_{vol} = \frac{1}{D} \left[J^2 + \frac{1}{J^2} - 2\right] \,. \tag{2.2.39}$$

The first isochoric invariant $\bar{I}_1$ and Jacobian J are given by Equation (2.2.30) and Equation (2.2.3) as:

$$\begin{aligned}\bar{I}_1 &= \operatorname{tr}\left(\bar{\boldsymbol{C}}\right) \,, \\ J &= \det\left(\boldsymbol{F}\right) \,.\end{aligned}$$

The non-zero scalar first derivatives of the strain energy functions are:

$$\frac{\partial \bar{\Psi}}{\partial \bar{I}_1} = G \,, \quad \frac{\partial \Psi_{vol}}{\partial J} = \frac{2}{D} \left[J - J^{-3}\right] \,. \tag{2.2.40}$$

And the only non-zero scalar second derivative is:

$$\frac{\partial^2 \Psi_{vol}}{\partial J \partial J} = \frac{2}{D}\left[1 + 3J^{-4}\right] . \tag{2.2.41}$$

For the Neo-Hookean case, the only relevant invariant is $\bar{I}_1$, which corresponds to the isochoric second-order tensor given by Equation (2.2.31) as:

$$\bar{\boldsymbol{A}}_1 = \bar{\boldsymbol{B}}$$

Where $\bar{\boldsymbol{B}}$ is the isochoric left Cauchy-Green tensor.

The corresponding isochoric fourth-order tensor is given by Equation (2.2.37) as:

$$\bar{\mathbb{A}}_1 = \mathbb{O}$$

Combining Equations (2.2.25) to (2.2.27), (2.2.29), (2.2.31) and (2.2.40) leads to the expression of the Kirchhoff stress for the Neo-Hookean case as:

$$\boldsymbol{\tau} = 2G\left[\bar{\boldsymbol{B}} - \frac{1}{3}\bar{I}_1 \boldsymbol{I}\right] + \frac{2}{D}\left[J^2 - J^{-2}\right]\boldsymbol{I} . \tag{2.2.42}$$

Combining Equations (2.2.29), (2.2.31), (2.2.33) to (2.2.35), (2.2.37), (2.2.40) and (2.2.41) leads to the expression of the spatial elasticity tensor for the Neo-Hookean case as:

$$\begin{aligned} \mathbb{c} = 4G\left[\left[-\frac{1}{3}\right]\left[\boldsymbol{I}\otimes\bar{\boldsymbol{B}} + \bar{\boldsymbol{B}}\otimes\boldsymbol{I} - \bar{I}_1 \boldsymbol{I}\odot\boldsymbol{I}\right] + \left[-\frac{1}{3}\right]^2 \bar{I}_1 \boldsymbol{I}\otimes\boldsymbol{I}\right] \\ + \left[\frac{4}{D}\left[J^2 + J^{-2}\right]\right]\boldsymbol{I}\otimes\boldsymbol{I} - \left[\frac{4}{D}\left[J^2 - J^{-2}\right]\right]\boldsymbol{I}\odot\boldsymbol{I} . \end{aligned} \tag{2.2.43}$$

It is worth noting the following elastic parameter relations between the shear modulus G, compressibility D, Young's modulus E and Poisson's ratio ν:

$$E = \frac{9G}{3 + GD}, \quad \nu = \frac{3 - 2GD}{6 + 2GD} . \tag{2.2.44}$$

The Young's modulus E and Poisson's ratio ν are used throughout the remainder of this study, as they provide a simpler physical intuition in terms of material stiffness and the degree of material incompressibility. Higher values of E represent higher material stiffnesses, and incompressibility is increasingly enforced as $\nu \to 0.5$.

Myocardium constitutive model

The anisotropic hyperelastic model used for the myocardium has the following isochoric $\bar{\Psi}$ and volumetric Ψ_{vol} strain energy functions, as per Holzapfel et al. (2009) and Sack et al. (2018, Eq. 1, Eq. 2):

$$\begin{aligned} \bar{\Psi} = \frac{a}{2b}\exp\left[b(\bar{I}_1 - 3)\right] + \frac{a_f}{2b_f}(\exp\left[b_f(\bar{I}_{4f} - 1)^2\right] - 1) \\ + \frac{a_s}{2b_s}(\exp\left[b_s(\bar{I}_{4s} - 1)^2\right] - 1) + \frac{a_{fs}}{2b_{fs}}(\exp\left[b_{fs}\bar{I}_{8fs}^2\right] - 1) , \end{aligned} \tag{2.2.45}$$

$$\Psi_{vol} = \frac{1}{D}\left[\frac{J^2-1}{2} - \ln\left(J\right)\right] , \tag{2.2.46}$$

Where a, b, a_f, a_s, a_{fs}, b_{fs}, D are positive material constants. The model uses a right-handed orthonormal co-ordinate system consisting of a fibre axis $\boldsymbol{f}_0$, sheet axis $\boldsymbol{s}_0$ and sheet-normal axis $\boldsymbol{n}_0$. The relevant invariants are given by Equation (2.2.30) as:

$$\begin{aligned} \bar{I}_1 &= \mathrm{tr}\left(\bar{\boldsymbol{C}}\right) , & \bar{I}_{4f} &= \boldsymbol{f}_0 \cdot \bar{\boldsymbol{C}}\boldsymbol{f}_0 , \\ \bar{I}_{4s} &= \boldsymbol{s}_0 \cdot \bar{\boldsymbol{C}}\boldsymbol{s}_0 , & \bar{I}_{8fs} &= \boldsymbol{f}_0 \cdot \bar{\boldsymbol{C}}\boldsymbol{s}_0 . \end{aligned}$$

The non-zero scalar first derivatives of the strain energy functions are:

$$\begin{aligned} \frac{\partial\bar{\Psi}}{\partial\bar{I}_1} &= \frac{a}{2}\exp\left[b(\bar{I}_1-3)\right] , \\ \frac{\partial\bar{\Psi}}{\partial\bar{I}_{4f}} &= a_f(\bar{I}_{4f}-1)\exp\left[b_f(\bar{I}_{4f}-1)^2\right] , \\ \frac{\partial\bar{\Psi}}{\partial\bar{I}_{4s}} &= a_s(\bar{I}_{4s}-1)\exp\left[b_s(\bar{I}_{4s}-1)^2\right] , \\ \frac{\partial\bar{\Psi}}{\partial\bar{I}_{8fs}} &= a_{fs}\bar{I}_{8fs}(\exp\left[b_{fs}\bar{I}_{8fs}^2\right] , \\ \frac{\partial\Psi_{vol}}{\partial J} &= \frac{1}{D}\left[J - J^{-1}\right] . \end{aligned} \tag{2.2.47}$$

And the non-zero scalar second derivatives of the strain energy functions are:

$$\begin{aligned} \frac{\partial^2\bar{\Psi}}{\partial\bar{I}_1\partial\bar{I}_1} &= \frac{ab}{2}\exp\left[b(\bar{I}_1-3)\right] , \\ \frac{\partial^2\bar{\Psi}}{\partial\bar{I}_{4f}\partial\bar{I}_{4f}} &= a_f(\exp\left[b_f(\bar{I}_{4f}-1)^2\right])(1+2b_f(\bar{I}_{4f}-1)^2 , \\ \frac{\partial^2\bar{\Psi}}{\partial\bar{I}_{4s}\partial\bar{I}_{4s}} &= a_s(\exp\left[b_s(\bar{I}_{4s}-1)^2\right])(1+2b_s(\bar{I}_{4s}-1)^2) , \\ \frac{\partial^2\bar{\Psi}}{\partial\bar{I}_{8fs}\partial\bar{I}_{8fs}} &= a_{fs}(\exp\left[b_{fs}\bar{I}_{8fs}^2\right])(1+2b_{fs}\bar{I}_{8fs}^2) , \\ \frac{\partial^2\Psi_{vol}}{\partial J\partial J} &= \frac{1}{D}\left[1 + J^{-2}\right] . \end{aligned} \tag{2.2.48}$$

The partial first derivatives of the relevant invariants with respect to $\boldsymbol{C}$ are:

$$\begin{aligned} \frac{\partial\bar{I}_1}{\partial\boldsymbol{C}} &= \boldsymbol{I} , & \frac{\partial\bar{I}_{4f}}{\partial\boldsymbol{C}} &= \boldsymbol{f}_0\otimes\boldsymbol{f}_0 , \\ \frac{\partial\bar{I}_{4s}}{\partial\boldsymbol{C}} &= \boldsymbol{s}_0\otimes\boldsymbol{s}_0 , & \frac{\partial\bar{I}_{8fs}}{\partial\boldsymbol{C}} &= \frac{1}{2}\left[\boldsymbol{f}_0\otimes\boldsymbol{s}_0 + \boldsymbol{s}_0\otimes\boldsymbol{f}_0\right] . \end{aligned} \tag{2.2.49}$$

And the partial second derivatives of the relevant invariants with respect to $\boldsymbol{C}$ are:

$$\frac{\partial^2\bar{I}_p}{\partial\boldsymbol{C}\partial\boldsymbol{C}} = \mathbb{0} , \quad p = 1, 4f, 4s, 8fs . \tag{2.2.50}$$

From equation (2.2.31), the relevant isochoric, second-order tensors $\bar{\boldsymbol{A}}_i$ are:

$$\bar{\boldsymbol{A}}_1 = \bar{\boldsymbol{B}}\,, \qquad \bar{\boldsymbol{A}}_{4f} = \boldsymbol{f} \otimes \boldsymbol{f}\,,$$
$$\bar{\boldsymbol{A}}_{4s} = \boldsymbol{s} \otimes \boldsymbol{s}\,, \quad \bar{\boldsymbol{A}}_{8fs} = \frac{1}{2}\left[\boldsymbol{f} \otimes \boldsymbol{s} + \boldsymbol{s} \otimes \boldsymbol{f}\right]\,.$$

Where:

$$\boldsymbol{f} = \boldsymbol{F}\boldsymbol{f}_0\,, \quad \boldsymbol{s} = \boldsymbol{F}\boldsymbol{s}_0\,. \tag{2.2.51}$$

From equation (2.2.37), the relevant isochoric, fourth-order tensors $\mathbb{A}_i$ are:

$$\bar{\mathbb{A}}_1 = \bar{\mathbb{A}}_{4f} = \bar{\mathbb{A}}_{4s} = \bar{\mathbb{A}}_{8fs} = \mathbb{0}\,.$$

Combining Equations (2.2.25) to (2.2.27), (2.2.29), (2.2.31) and (2.2.47) leads to the expression of the Kirchhoff stress tensor, and combining Equations (2.2.29), (2.2.31), (2.2.33) to (2.2.35), (2.2.37), (2.2.47) and (2.2.48) leads to the expression of the spatial elasticity tensor for the anisotropic case. The final expressions have been omitted for conciseness.

Computational homogenisation

Given a material with a known heterogenous microstructure, homogenisation is an approach which aims to determine the equivalent effective macroscale properties of the material (Yvonnet 2019). Computational homogenisation provides a framework whereby these effective properties can be evaluated computationally, as opposed to analytically. One of the primary advantages of using a computational homogenisation approach, as opposed to including direct representations of the microstructure in a macroscale model, is that explicit descriptions of all the heterogeneities in a material can be avoided, drastically reducing computational expense (Yvonnet 2019). In order to adopt a computational homogenisation approach, one must abide by certain core principles, most notably the Hill-Mandel Principle, which leads to restrictions of the types of boundary conditions that can be used. This section provides a summary of the key considerations relating to computational homogenisation that were relevant for the present study.

To begin, it is convenient to define the volume averaging operator $\langle\bullet\rangle$ as the integral over the material domain Ω_0 divided by the volume as:

$$\text{Volume average:} \qquad \langle\bullet\rangle = \frac{1}{|\Omega_0|}\int_{\Omega_0} \bullet \,\mathrm{d}\Omega_0 \tag{2.2.52}$$

The homogenisation approach adopted in this study assumes a separation of length scales, that is, the characteristic length of the microstructure L_m was assumed to be much smaller than that of the macroscale structure L_M:

$$\text{Separation of scales:} \qquad L_m \ll L_M \tag{2.2.53}$$

Saeb et al. (2016) noted that, so long as macro-gradients remain small and there is no occurrence of material failure, this assumption is particularly valid. Under the separation of scales assumption, it is then valid to postulate the following relation between the macroscale and microscale deformation gradients (Souza Neto et al. 2015, Eq. 8):

$$\text{Deformation gradient relation:} \qquad \boldsymbol{F}_M = \langle \boldsymbol{F}_m \rangle \tag{2.2.54}$$

Crucially, the energy equivalence between the microscale and the macroscale is stipulated by the Hill-Mandel Principle. In their study, Souza Neto et al. (2015) rephrased the Hill-Mandel Principle into the following variational form, where $\boldsymbol{P}_M$ and $\boldsymbol{P}_m$ are the macroscale and microscale first Piola-Kirchhoff stress, respectively (Souza Neto et al. 2015, Eq. 22):

$$\text{Hill-Mandel Principle (variational form):} \qquad \boldsymbol{P}_M : \delta \boldsymbol{F}_M = \langle \boldsymbol{P}_m : \delta \boldsymbol{F}_m \rangle \tag{2.2.55}$$

Their study further noted that the following relation, regarding the first Piola-Kirchhoff stress at the macroscale and microscale, could be obtained as a consequence of their variational formulation of the Hill-Mandel Principle (Souza Neto et al. 2015, Eq. 24):

$$\text{First PK stress relation:} \qquad \boldsymbol{P}_M = \langle \boldsymbol{P}_m \rangle \tag{2.2.56}$$

In practice, this requires the careful selection of boundary conditions which have been shown to satisfy the Hill-Mandel Principle of Equation (2.2.55), and allow us to prescribe a chosen volume averaged deformation gradient or first Piola-Kirchhoff stress to a given microstructure. Examples of such boundary conditions are kinematically uniform boundary conditions (KUBCs), periodic boundary conditions, and constant traction boundary conditions, given as:

$$\text{KUBCs:} \qquad \boldsymbol{u} = [\boldsymbol{F}_M - \boldsymbol{I}]\, \boldsymbol{X} \qquad \text{on the boundary } \Gamma\,, \tag{2.2.57}$$

$$\text{Periodic:} \qquad \boldsymbol{u}^+ - \boldsymbol{u}^- = [\boldsymbol{F}_M - \boldsymbol{I}] \left[\boldsymbol{X}^+ - \boldsymbol{X}^-\right] \qquad \text{on the boundary } \Gamma\,, \tag{2.2.58}$$

$$\text{Constant traction:} \qquad \bar{\boldsymbol{t}} = \boldsymbol{P}_M \boldsymbol{N} \qquad \text{on the boundary } \Gamma\,. \tag{2.2.59}$$

Where $\boldsymbol{F}_M$ and $\boldsymbol{P}_M$ represent a prescribed macroscale deformation gradient and first Piola-Kirchhoff stress tensor respectively, $\boldsymbol{X}$ denotes the position vector in the material configuration, $\boldsymbol{u}$ represents the displacement field, and $\boldsymbol{N}$ is the outward unit normal to the boundary in the material configuration. The superscripts $(+)$ and $(-)$ in the periodic boundary condition denote corresponding points on opposite faces of the microstructure.

The concept of a representative volume element (RVE) refers to a sample of the microstructure that is large enough such that the apparent (i.e. observed) behaviour of the homogenised material is invariant to the boundary conditions applied to the RVE. In practice, this often requires expansion of the selected microstructural domain, until the response of the selection converges under all applied boundary conditions. When this convergence point is reached, the apparent behaviour of the RVE is said to represent the effective behaviour of the macroscale structure. It is important to note that the present study did not focus on iteratively expanding the microstructural domain, in order to ensure that the simulations described in Section 2.3.2 remained computationally feasible. Furthermore, it should be noted that the remainder of the study makes use of KUBCs, defined in Equation (2.2.57). This choice was made as KUBCs are the simplest to implement computationally, and can be used as long as one is able to prescribe a macroscale deformation gradient. Further detail on how prescribable macroscale deformation gradients were determined is provided in Section 2.3.1.

2.2.2 The deal.II finite-element library

The deal.II FE library is a free, open-source C++ library which aims to support the creation of FE codes. It provides documented tools enabling the solution of various partial differential equations (PDEs) using the FE method. Figure 2.5 provides an outline on how the main groups of deal.II classes interact.

Short descriptions of the core deal.II modules are as follows, detailed descriptions can be found on the deal.II website[1]:

- **Manifold** – Provides a means of describing the geometry of the domain using differential geometry. It is distinct from a standard mesh object as one does not have to discretise the domain.

---

[1] `https://dealii.org/developer/doxygen/deal.II/index.html`

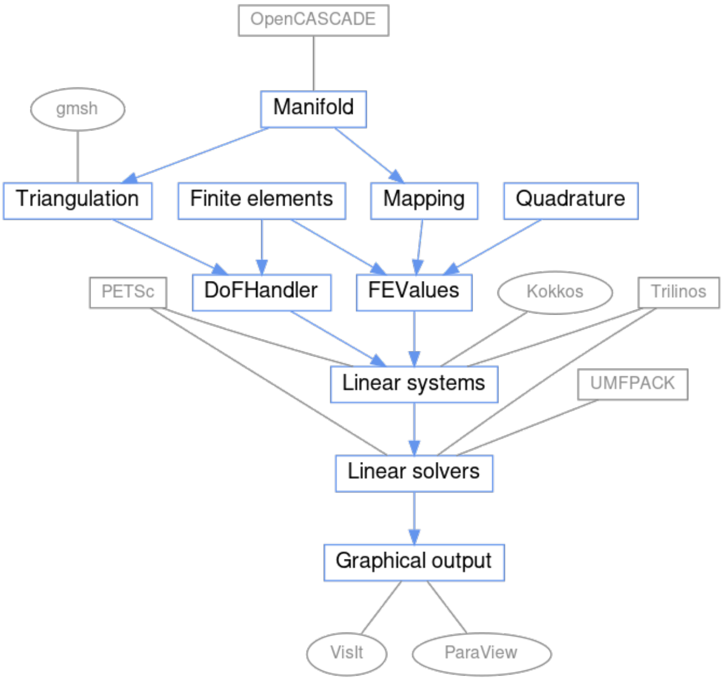

Figure 2.5: Overview of the deal.II code library. Core modules are outlined in blue; greyed-out modules represent optional external modules. The tree structure of the diagram represents the order of operations followed to produce an FE solution, as well as the dependency relations between modules.

- **Triangulation** – Collections of cells and their boundary objects. Triangulation classes store the geometric and topological properties of a mesh.
- **Finite elements** – Describes a finite-element space on a reference cell, as well as shape function values and gradients at points on a reference cell.
- **Mapping** – Describes how to map the reference cell to the real cell, and vice versa.
- **Quadrature** – Describes quadrature points and weights on the unit cell.
- **DoFHandler** – Allocates and enumerates the degrees-of-freedom of the system.
- **FEValues** – Computes the mapping of reference cell values that are required for assembly of the discrete system to a given real cell.
- **Linear systems** – Data structures for storing the system matrix and right-hand side.
- **Linear solvers** – Provides classes which solve a linear system of equations.
- **Graphical output** – Allows the generation of output files for visualisation.

2.2.3 Design and features of developed FE solver

The FE solver which was developed in this study consists of various classes, which can be grouped in terms of their function. Figure 2.6 provides a high-level overview of the structure of the FE program, including descriptions of each class group, as well as dependency relations between them.

A more extensive overview of the program, which includes the key members and member functions of the core classes (i.e. those used to generate the results included in this study), can be seen in Figure 2.7. Many class members, member functions, and member function arguments have been omitted for visual conciseness.

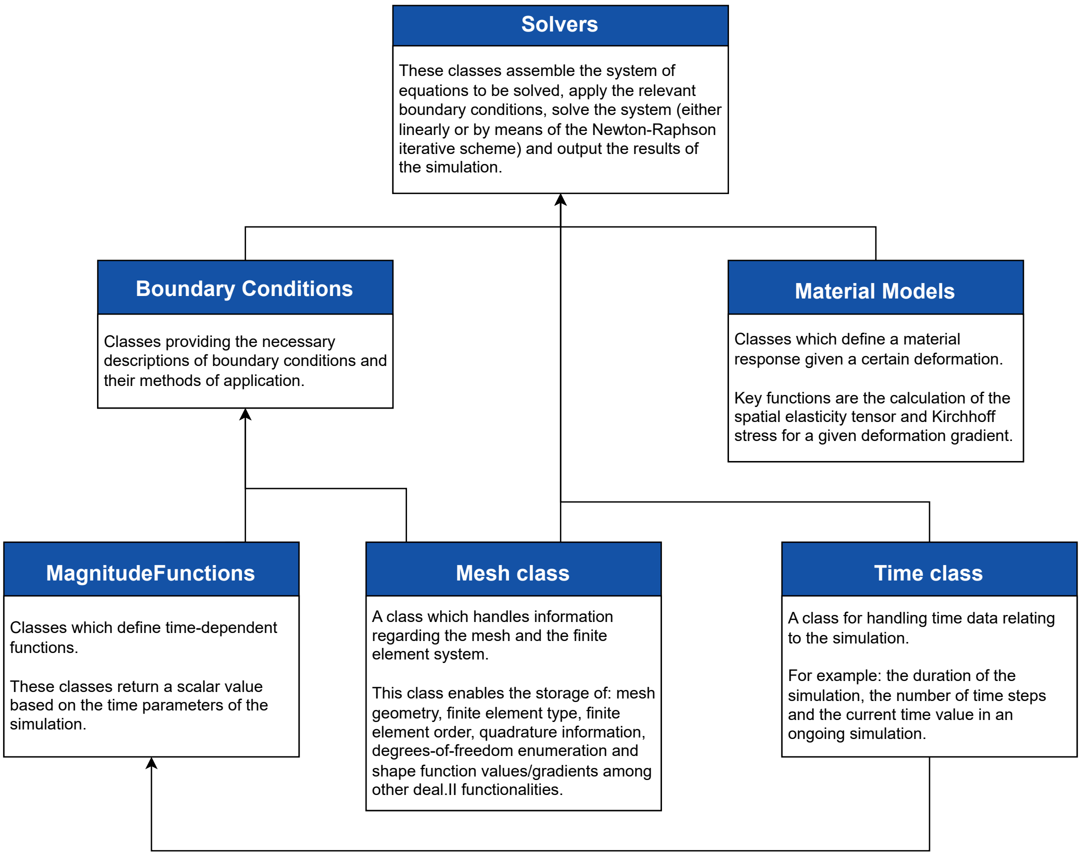

Figure 2.6: High-level overview of the developed program.

Detailed program description

The program is comprised of a set of classes, each with its own set of members (i.e. variables) and functions (also known as member functions). The relationship between the core classes of the program can be seen in Figure 2.7, which indicates how classes depend on each other, and which classes inherit members and functions from other classes. Ultimately, the `NLSolver` class provides the solutions to a given simulation problem. However, it depends on the existence of the remaining classes in order to function properly, as indicated by the directional arrows seen in Figure 2.7. This section describes the purpose of each class in the program. Detail is provided with regard to both the core classes and the remaining classes, the latter of which illustrate the functionalities of the program beyond the results generated in this study.

Mesh and Time classes

The `Mesh` class stores the mesh and finite-element system data for a simulation, as well as the global numbering of the system's degrees-of-freedom. Consolidating this information allows other classes to access it without storing it themselves. The `KinematicUniform` boundary condition class, as well as the `Solver` and `NLSolver` classes, rely on the data stored in the `Mesh` class.

Similarly, the `Time` class consolidates time-related data, such as the total simulation duration, the time step size, and the current time. The functions of the class allow the retrieval of this data, as well as the ability to increment the system to the next time step. Figure 2.8 provides an overview of the `Mesh` and `Time` classes.

MagnitudeFunction classes

The developed program is capable of handling time-dependent simulations, where parameters can change across time steps, and a solution is calculated at each time step. The `Time` class enables these simulations by managing time data. Additionally, a class was needed to output a dynamic scalar value

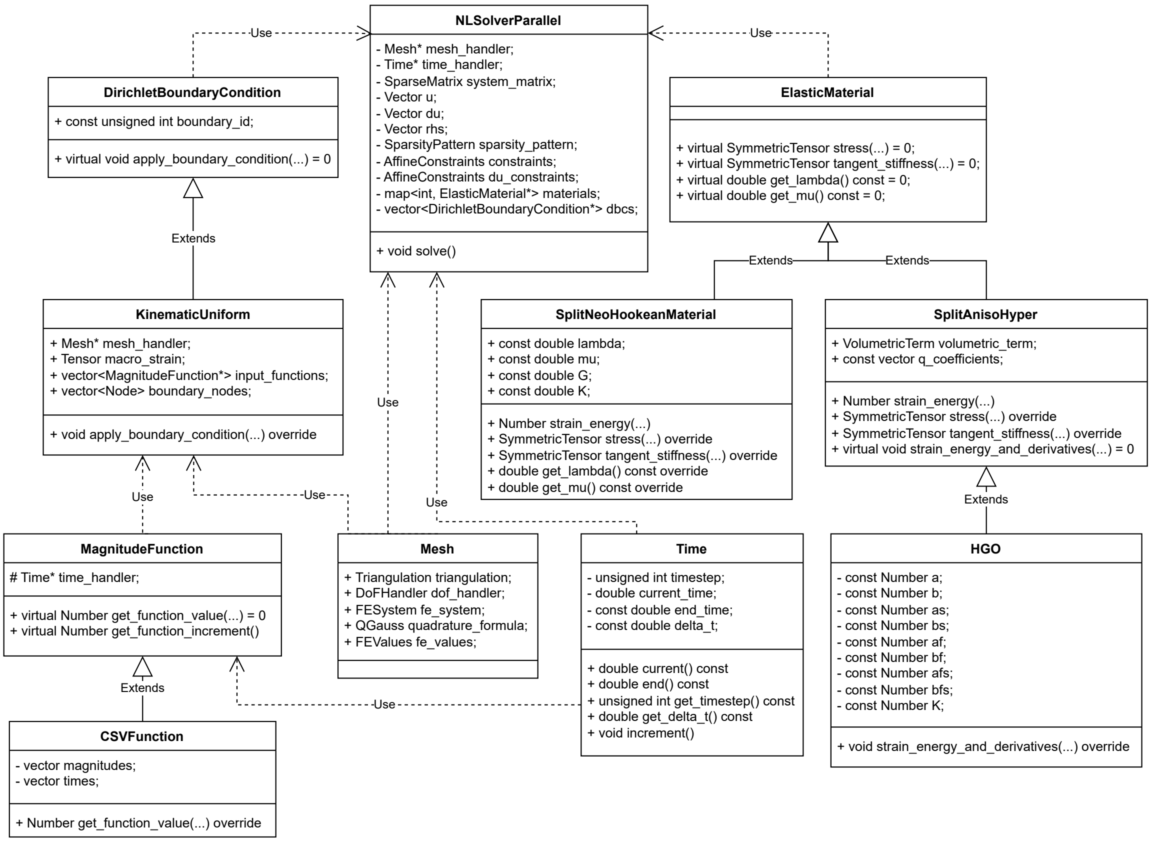

Figure 2.7: Unified Modelling Language (UML) overview of the core classes of the developed program. Solid lines marked "Extends" indicate inheritance relationships and dashed lines marked "Use" indicate dependency relationships.

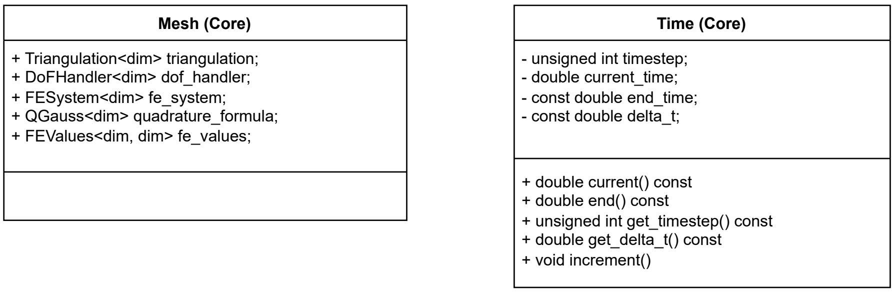

Figure 2.8: UML diagram of the `Mesh` and `Time` classes.

based on the current time-state of the simulation. The `MagnitudeFunction` classes provide this functionality by retrieving time data from the `Time` class and returning a corresponding scalar value. For example, the `RampFunction` class, a child class of `MagnitudeFunction`, returns a linearly interpolated value between predefined start and end values, based on the current time and total simulation duration. The `CSVFunction` class allows for a set of magnitude values and a set of time values, extracted from a comma-separated value (CSV) file, to be used. The `CSVFunction` class retrieves the current simulation time and returns the corresponding function magnitude. If the current simulation time is not included in the original set of time data, a linearly-interpolated function magnitude is returned using the nearest available time and magnitude values. These classes enable the definition of time-dependent functions, which can be used, for example, to define time-dependent boundary conditions. Figure 2.9 provides an overview of the `MagnitudeFunction` classes.

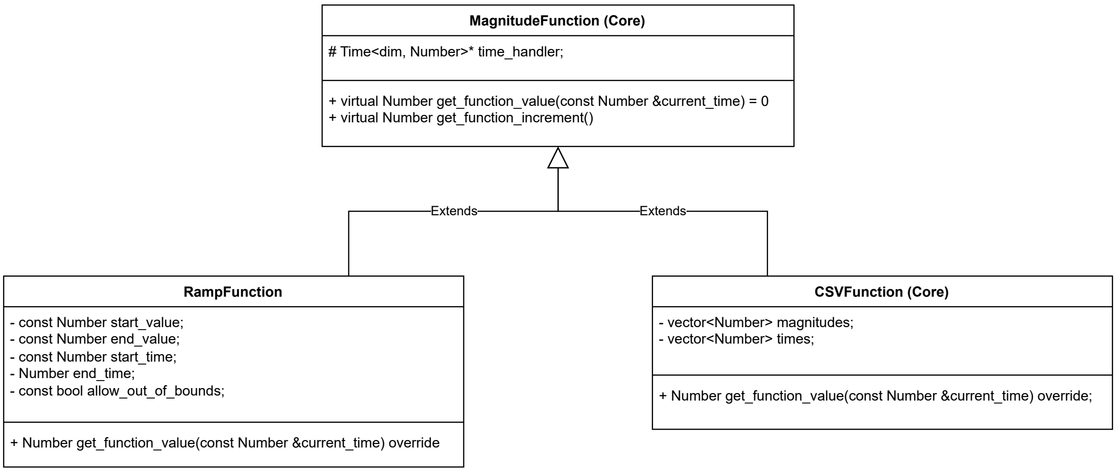

Figure 2.9: UML diagram of the `MagnitudeFunction` classes.

Boundary condition classes

For the case study simulations detailed in Section 2.3.2, only Dirichlet boundary conditions, specifically kinematic uniform boundary conditions, were required. The `DirichletBoundaryCondition` parent class allows the application of these boundary conditions, by identifying the relevant boundary, and applying the necessary constraints to the corresponding degrees-of-freedom. It includes child classes for different types of boundary conditions: `Fixed`, `Prescribed`, `Slider`, and `KinematicUniform`. The `Fixed` child class constrains the displacement of all degrees-of-freedom on the boundary to zero. The `Prescribed` child class constrains the displacement of the relevant degrees-of-freedom to a specified value, which can be made time-dependent using `MagnitudeFunction` classes. The `Slider` child class prevents displacement of the degrees-of-freedom in one co-ordinate direction, allowing movement in the plane of the remaining two directions. The `KinematicUniform` child class implements kinematically uniform boundary conditions, described by Equation (2.2.57), by applying a predefined macroscopic strain tensor to the system. This macroscopic strain tensor can also be made time-dependent using `MagnitudeFunction` classes. Figure 2.10 provides an overview of the boundary condition classes.

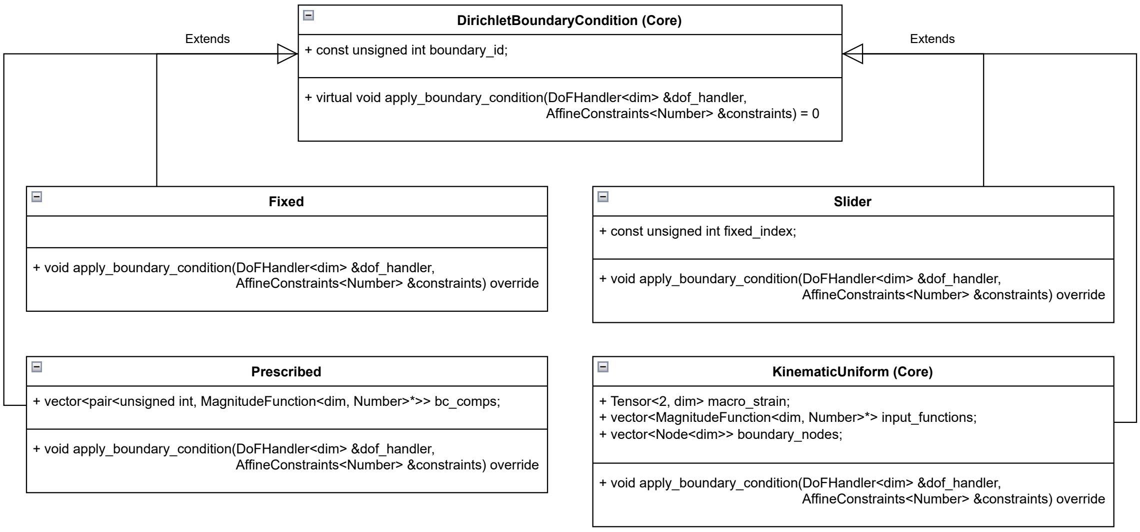

Figure 2.10: UML diagram of the boundary condition classes.

Material model classes

In addition to the mesh geometry and boundary condition definitions, constitutive models describing the stress-strain relationship of a material are necessary in assembling the FE system. The material classes in the program calculate the spatial elasticity and Kirchhoff stress tensors based on the material model and deformation gradient. Section 2.2.1 - "Constitutive modelling" details how the expressions for these tensors are derived from the material model's strain energy function. In the non-linear FE assembly process, these tensors are used to calculate the global tangent stiffness matrix and residual vector for the current Newton-Raphson iteration. In the linear case, the global stiffness matrix and right-hand side vector depend only on the Lamé parameters λ and μ, rather than the deformation gradient.

For this study, isotropic and anisotropic hyperelastic materials were considered. The `ElasticMaterial` parent class provides the two material parameters (λ and μ) as well as the spatial elasticity tensor and Kirchhoff stress tensor for a given deformation gradient. The `LinearElasticMaterial` child class represents a linear elastic material model and returns constant tensors independent of the deformation gradient. The `NeoHookeanMaterial` child class represents a compressible hyperelastic Neo-Hookean material model, with tensors that depend on the deformation gradient. The `SplitNeoHookeanMaterial` child class represents a Neo-Hookean model that uses an isochoric-volumetric split of the deformation gradient, given by Equations (2.2.38) and (2.2.39), where the additional parameter, K, is the bulk modulus of the material, given by the following relation:

$$K = \frac{E}{3(1-2\nu)} \,. \tag{2.2.60}$$

The `LinearElasticMaterial`, `NeoHookeanMaterial` and `SplitNeoHookeanMaterial` classes all behave isotropically.

The `SplitAnisoHyper` parent class allows for the implementation of anisotropic, hyperelastic material models which use an isochoric-volumetric split of the deformation gradient. This is reflected in the inclusion of the additional `structural_vectors` argument representing, for example, fibre directions, to the functions responsible for calculating the Kirchhoff stress tensor and spatial elasticity tensor. The `HGO` class, a child class of `SplitAnisoHyper`, implements a variation of the material model developed by Holzapfel et al. (2009), using an isochoric-volumetric split of the deformation gradient, as given by Equations (2.2.45) and (2.2.46).

Further detail on the implementation of the core `SplitNeoHookeanMaterial` and `HGO` classes can be found in Section 2.2.1 - "Constitutive modelling", where the expressions for the Kirchhoff stress and spatial elasticity tensors have been derived. Figure 2.11 provides an overview of the material model classes.

Solver classes

The two solver classes, `Solver` and `NLSolver`, are responsible for assembling and solving the FE system at each time step of the simulation. These classes make use of shared memory parallelisation, allowing the assembly and solving procedures to be executed efficiently using multiple processor cores. Both solvers require information regarding the geometry, boundary conditions, and material models, which are provided by the `Mesh`, `DirichletBoundaryCondition`, and `ElasticMaterial` classes respectively. The `Solver` class implements a linear solution process by assembling the system of equations, applying the boundary conditions, solving the linear system, and outputting the results of the simulation. In contrast, the `NLSolver` class employs a Newton-Raphson iterative solution scheme, where the solution is refined through repeated linear solving steps until the residual falls within a predefined tolerance. At the end of each time step, both solvers output the displacement solution and the calculated system stresses. Both the linear and non-linear solvers employ the conjugate gradient method. Figure 2.12 provides an overview of the solver classes.

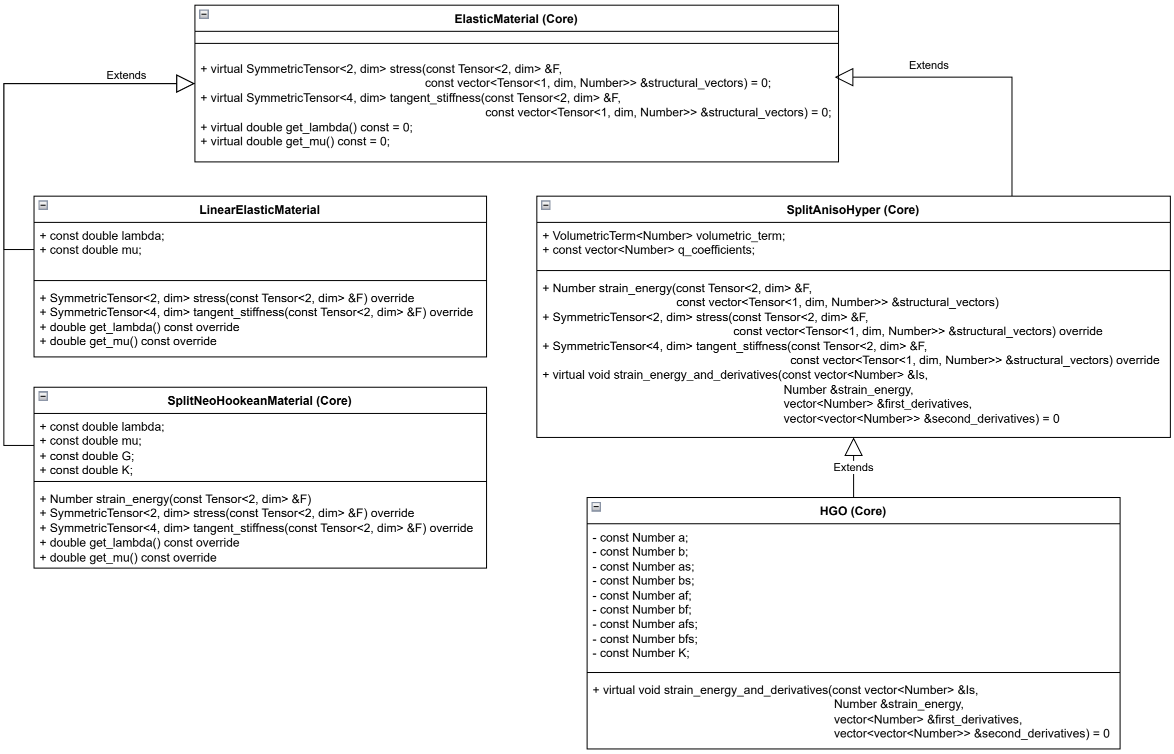

Figure 2.11: UML diagram of the material model classes.

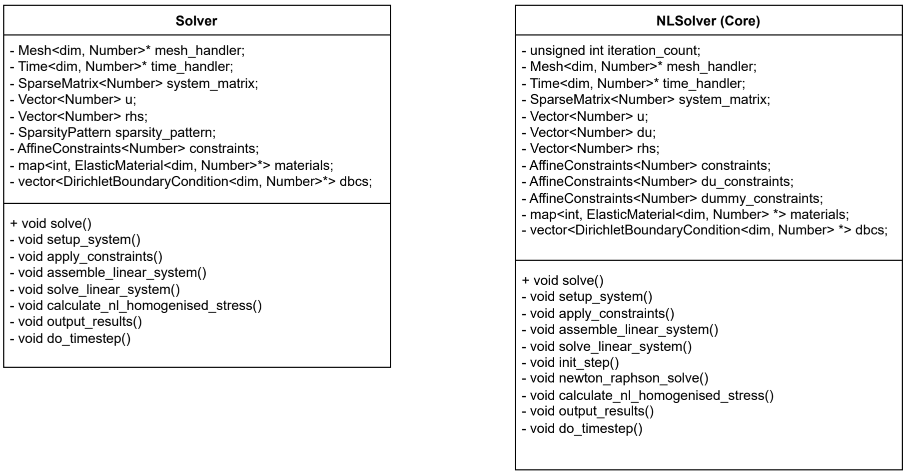

Figure 2.12: UML diagram of the linear and non-linear solver classes.

2.3 Application of developed framework

This section presents an application example which demonstrates how the developed geometries and finite-element solver can be used in investigating the microstructural mechanical response of myocardium with hydrogel injectate inclusions. This application example was intended to provide examples of the results and insights that the developed framework can produce, as well as to determine paths for extension and further development.

The first step in developing the application example was to determine boundary conditions which were suitable for application to the microstructural geometries, and which aimed to replicate loading cases which could reasonably be expected to occur during the cardiac cycle (defined here as the time from one peak diastole to the next). This was done by extracting and processing the results of an existing, macroscale, FE model from Motchon et al. (2023) and Absalom Maluleke (unpublished PhD study), which were made available for this study. The second step was the development of two computational case studies intended to demonstrate the capabilities of the developed computational tools. The first of these cases makes use of the idealised geometry described in Section 2.1.4, and the second makes use of the realistic geometry described in Section 2.1.3. Detail will be provided with regard to how a set of suitable boundary conditions was obtained, as well as the purpose and structure of each case study.

2.3.1 Obtaining boundary conditions

With macroscopic strain data representing the heart's behaviour during the cardiac cycle, KUBCs can be applied to a microstructural RVE to determine the corresponding stress response. For this purpose, an existing, macroscale, FE model of a rat heart, from Motchon et al. (2023) and Absalom Maluleke (unpublished PhD study), was used. The model was developed by the Department of Human Biology of the University of Cape Town using the finite-element software ABAQUS. In their work, medical imaging data, acquired from *ex vivo* microcomputed tomography scans of a rat heart, were used to develop a biventricular cardiac geometry model. Using the software package SimpleWare ScanIP, the geometry was discretised into quadratic tetrahedron elements and exported to ABAQUS/CAE. The final geometry used to develop the FE model, as seen in Figure 2.13, was truncated to exclude the two upper chambers of the heart. A zero displacement boundary condition was then applied to the base nodes, while a linearly increasing pressure boundary condition was applied to the left and right ventricular chambers. Further detail on the development of this macroscale model can be found in Motchon et al. (2023).

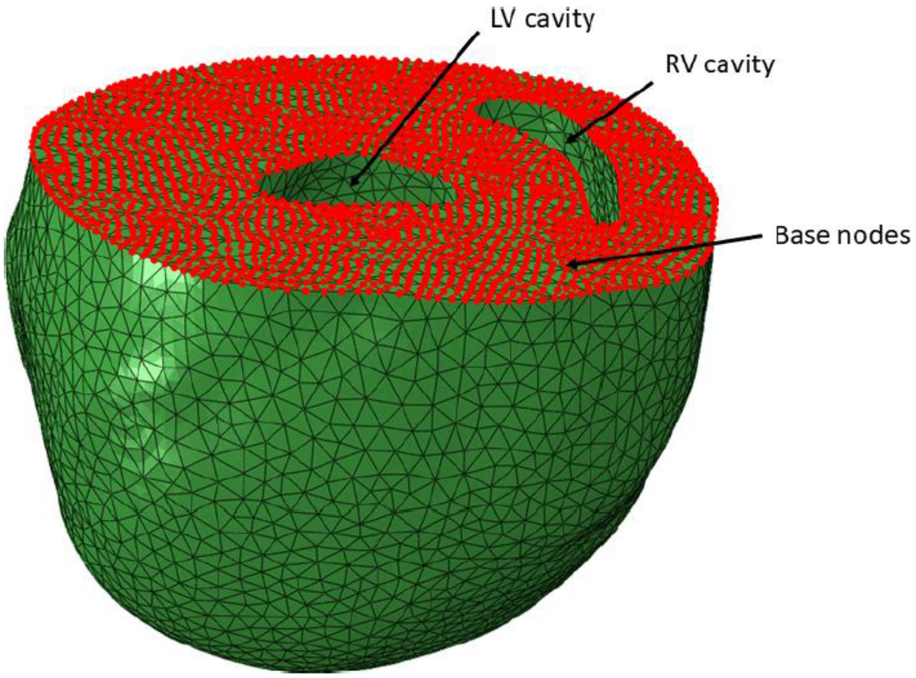

Figure 2.13: Biventricular cardiac geometry of the existing macroscopic ABAQUS model (Motchon et al. 2023) and Absalom Maluleke (unpublished PhD study).

In the present study, time-dependent cardiac strain data were extracted from the macroscale model at each quadrature point. The resulting dataset included spatial logarithmic strain tensor components for 2 180 104 quadrature points over 61 time steps (representing three cardiac cycles with a total time of 2.34 s). For compatibility with the intended KUBC implementation, the spatial stretch tensor corresponding to each spatial logarithmic strain tensor was calculated using the following relation from Bonet et al. (2008, Eq. 4.51):

$$\boldsymbol{e}^{(0)} = \sum_{\alpha=1}^{3} \ln \lambda_\alpha \boldsymbol{n}_\alpha \otimes \boldsymbol{n}_\alpha = \ln \boldsymbol{V} \,. \tag{2.3.1}$$

Where the spatial stretch tensor $\boldsymbol{V}$ is related to the deformation gradient $\boldsymbol{F}$ by Bonet et al. (2008, Eq. 4.36):

$$\boldsymbol{F}\boldsymbol{F}^T = \boldsymbol{V}^2\,. \tag{2.3.2}$$

To address the computational expense of processing the entire macroscopic dataset, a representative sampling method was implemented to develop boundary conditions for a set of computational case studies. A k-means clustering algorithm was applied to partition the 2 180 104 sets of $\boldsymbol{V}$ tensor data into five clusters. Three invariants, I_1, I_2 and I_3, were used as the criteria for the clustering algorithm, where:

$$\begin{aligned} I_1 &= \operatorname{tr}\left(\boldsymbol{V}^2\right)\,, \\ I_2 &= \frac{1}{2}\left[\operatorname{tr}\left(\boldsymbol{V}^2\right)^2 - \operatorname{tr}\left(\boldsymbol{V}^4\right)\right]\,, \\ I_3 &= \det\left(\boldsymbol{V}^2\right)\,. \end{aligned} \tag{2.3.3}$$

As a result, kinematically-similar sets of quadrature point data were constructed. From these, the five cluster centres were chosen as test cases for use with the microstructural geometries developed in this study.

2.3.2 Case studies

Demonstration of the capabilities of the developed computational tools was accomplished through a set of case studies. The first of these case studies was conducted on the idealised mesh described in Section 2.1.4, and was intended to demonstrate the capacity of the developed program in solving problems with time-dependent boundary conditions, as well as the fact that different combinations of isotropic and anisotropic material models can be used. The second case study was conducted on the realistic mesh described in Section 2.1.3. This case study made use of five single strain state boundary conditions (i.e. not time-dependent), derived from the maxima of the five KUBC cluster centres. For each of the five single strain state boundary conditions, three hydrogel material parameter combinations were tested. The following section outlines the material parameters used for the case studies, and subsequently provides a more detailed description of each case study.

Material model parameters

For the anisotropic hyperelastic material model used for the myocardium, defined by Equations (2.2.45) and (2.2.46), the parameters in Table 2.1, adapted from Sack et al. (2018) and Motchon et al. (2023), were used. The bulk modulus K was chosen to be roughly 1000 times the largest linear term a_i, a guideline also used by Sack et al. (2018) and Göktepe et al. (2010).

For the isotropic, Neo-Hookean material model used for the hydrogel injectate, defined by Equations (2.2.38) and (2.2.39), three material parameter combinations, shown in Table 2.2, were tested. Throughout the rest of this study, the terms “Lower-bound stiffness”, “Median stiffness”, and “Upper-bound stiffness” refer to the material parameter combinations shown in Table 2.2. The chosen range of hydrogel stiffnesses was adapted from a study by H. Wang et al. (2017), which conducted computational investigations on hydrogels with stiffnesses up to 100 kPa.

Table 2.1: Material parameters for the anisotropic model used to describe the myocardium.

Parameter	**Value**	**Description**
a	$0.2065\,\mathrm{kPa}$	Governs the isotropic response
b	7.61	Governs the isotropic response
a_f	$0.68\,\mathrm{kPa}$	Governs additional stiffness in the fibre direction
b_f	14.61	Governs additional stiffness in the fibre direction
a_s	$0.945\,\mathrm{kPa}$	Governs additional stiffness in the sheet direction
b_s	12.67	Governs additional stiffness in the sheet direction
a_{fs}	$5.55 \times 10^{-3}\,\mathrm{kPa}$	Governs coupling stiffness in the fibre and sheet direction
b_{fs}	3.12	Governs coupling stiffness in the fibre and sheet direction
D	$0.001\,\mathrm{kPa}^{-1}$	Compressibility, defined as $D = \frac{1}{K}$
K	$1000\,\mathrm{kPa}$	Bulk modulus, defining material incompressibility.

Table 2.2: Material parameter combinations for the hydrogel injectate.

Parameter	**Lower-bound**	**Median**	**Upper-bound**
Elastic modulus E (kPa)	5.0	50.0	100.0
Poisson's ratio ν	0.49	0.49	0.49

Case Study 1: Idealised Mesh Simulations

Overview

As described in Section 2.1.4, an idealised mesh representing a myocardial tissue block with a cylindrical hydrogel inclusion was developed. This was done to allow for a computationally feasible demonstration of how time-dependent boundary conditions can be used with the developed FE solver. In this case study, the full, time-varying set of $\boldsymbol{V}$ tensor data, across 2.34 s, of one of the KUBC cluster centres was chosen to be applied to the idealised geometry. Two material model configurations were tested. In the first, the isotropic, Neo-Hookean model given by Equations (2.2.38) and (2.2.39) was used to describe both the hydrogel and the myocardium. In the second, the isotropic, Neo-Hookean model was used to describe the hydrogel, and the anisotropic model given by Equations (2.2.45) and (2.2.46) was used to describe the myocardium.

Simulation configurations

Two simulations were conducted as part of the first case study:

- Simulation 1 - Hydrogel and myocardium modelled using an isotropic, Neo-Hookean model defined by Equations (2.2.38) and (2.2.39).
- Simulation 2 - Hydrogel modelled using an isotropic, Neo-Hookean model and myocardium modelled using an anisotropic model defined by Equations (2.2.45) and (2.2.46).

For both simulations, the applied KUBC was a time-dependent set of V tensor data from one of the cluster centres.

Summary of simulation parameters

Table 2.3 provides a summary of the parameters used for the first case study.

Table 2.3: Parameters used for the first case study, conducted on the idealised mesh.

	Simulation 1	**Simulation 2**
Mesh	Idealised mesh	Idealised mesh
Boundary Condition	KUBC using the full time-varying set of left stretch tensor data from Cluster Centre 3	KUBC using the full time-varying set of left stretch tensor data from Cluster Centre 3
Myocardium material model	Neo-Hookean model with E = 100kPa and $\nu = 0.49$.	Anisotropic model with parameters shown in Table 2.1 and fibre directions shown in Equation (2.1.5).
Hydrogel material model	Neo-Hookean model with E = 50kPa and $\nu = 0.49$	Neo-Hookean model with E = 50kPa and $\nu = 0.49$

Case Study 2: Realistic Mesh Simulations

Overview

Section 2.1.3 describes how a realistic finite-element mesh, comprised of myocardium and hydrogel injectate, was developed from confocal microscopy imaging data. This case study used the realistic mesh and applied the maximum strain states from each of the five KUBC cluster centres as the boundary conditions. This resulted in five simulation scenarios, one for each cluster centre maximum. For each of these scenarios, three hydrogel material model parameters were tested. These were the “Lower-bound”, “Median”, and “Upper-bound” stiffness cases described in Table 2.2. In total, fifteen simulations were conducted as part of this case study, all of which used the anisotropic model given by Equations (2.2.45) and (2.2.46) to describe the myocardium, and the isotropic, Neo-Hookean model given by Equations (2.2.38) and (2.2.39) to describe the hydrogel. This case study aimed to demonstrate how parametric studies could be conducted using the developed computational tools, by varying the hydrogel stiffnesses. It further looked to investigate if the observed stress response of the realistic mesh ever exceeded reasonable elastic limits. Such an outcome would provide a justification for the extension of the developed FE solver into material models beyond hyperelasticity.

Simulation scenarios

Each of the five cluster centres defines a distinct simulation scenario, with three hydrogel material parameter sets evaluated per scenario, leading to a total of fifteen simulations:

- **Scenario 1: Cluster Centre 1**
- **Scenario 2: Cluster Centre 2**
- **Scenario 3: Cluster Centre 3**
- **Scenario 4: Cluster Centre 4**
- **Scenario 5: Cluster Centre 5**

Each scenario was simulated using:

- The realistic mesh described in Section 2.1.3.
- A left stretch tensor representing the maximum strain state of the corresponding cluster centre.
- An anisotropic material model for the myocardium, defined by Equations (2.2.45) and (2.2.46), with parameters shown in Table 2.1, and fibre directions shown in Equation (2.1.5).
- An isotropic, Neo-Hookean material model for the hydrogel, defined by Equations (2.2.38) and (2.2.39).
- Three hydrogel material parameter combinations: “Lower-bound”, “Median”, and “Upper-bound”,

as defined in Table 2.2.

Summary of simulation parameters

Tables 2.4 and 2.5 provide a summary of the parameters used for the second case study.

Table 2.4: Hydrogel material parameters used in the second case study (realistic mesh simulations). Each cluster centre strain state was tested with three different hydrogel stiffness values.

Applied KUBC	**Hydrogel Stiffness Case**	**Hydrogel Parameters**	
		E (kPa)	ν
Cluster Centre 1 Maximum	Lower-bound	5.0	0.49
	Median	50.0	0.49
	Upper-bound	100.0	0.49
Cluster Centre 2 Maximum	Lower-bound	5.0	0.49
	Median	50.0	0.49
	Upper-bound	100.0	0.49
Cluster Centre 3 Maximum	Lower-bound	5.0	0.49
	Median	50.0	0.49
	Upper-bound	100.0	0.49
Cluster Centre 4 Maximum	Lower-bound	5.0	0.49
	Median	50.0	0.49
	Upper-bound	100.0	0.49
Cluster Centre 5 Maximum	Lower-bound	5.0	0.49
	Median	50.0	0.49
	Upper-bound	100.0	0.49

Table 2.5: Mesh and myocardium material parameters used in the second case study. The myocardium was modelled as an anisotropic material with predefined fibre directions.

Mesh	Realistic finite-element mesh described in Section 2.1.3
Myocardium material model	Anisotropic model defined by Equations (2.2.45) and (2.2.46), with material parameters shown in Table 2.1 and fibre directions shown in Equation (2.1.5)
Hydrogel material model	Isotropic model defined by Equations (2.2.38) and (2.2.39).

Chapter 3

Results

The following section presents the results of the geometry development and application example of the developed framework described in Chapter 2. Detail will be provided with regard to the following outcomes:

1. The results of the geometry development methods outlined in Section 2.1. These include the construction of a realistic finite-element mesh based on confocal microscopy imaging data, as well as the construction of an idealised mesh.

2. The boundary conditions that were obtained using an existing macroscale FE model of rat myocardium, as outlined in Section 2.3.1. This was done to obtain KUBCs representing cardiac strain states that could reasonably occur throughout the cardiac cycle.

3. The results of the case studies described in Section 2.3.2. These case studies were conducted to demonstrate the simulation capabilities of the developed computational tools, as well as to investigate under which circumstances the assumption of elastic material behaviour may not be sufficient. In certain instances, where the elastic material behaviour assumption appears reasonable (i.e. observed stresses do not exceed reasonable elastic limits), observations are made to deduce experimental meaning from the results.

3.1 Geometry development

3.1.1 Development of a realistic microstructural mesh from confocal microscopy imaging data

Preprocessing

Preprocessing the available confocal microscopy imaging data was accomplished through the selection of a region of interest (ROI) and Contrast Limited Adaptive Histogram Equalisation (CLAHE) enhancement of the image dataset, as described in Section 2.1.3. Capturing of the cardiac tissue structure, while excluding blood vessel detail, was done through the selection of an ROI with dimensions 1.58 mm (radial), 1.09 mm (longitudinal), and 0.88 mm (circumferential). An example of a single 2D image slice, highlighting the ROI, can be seen in Figure 3.1. The full image is 1753 by 461 pixels, and the ROI is 650 by 450 pixels.

The images were cropped to focus on the ROI, and CLAHE-enhanced to improve the ability to distinguish tissue regions from void regions, as shown in Figure 3.2.

Image segmentation techniques

An example of the results following the global thresholding and region-grown segmentation techniques, described in Section 2.1.3, can be seen in Figure 3.3.

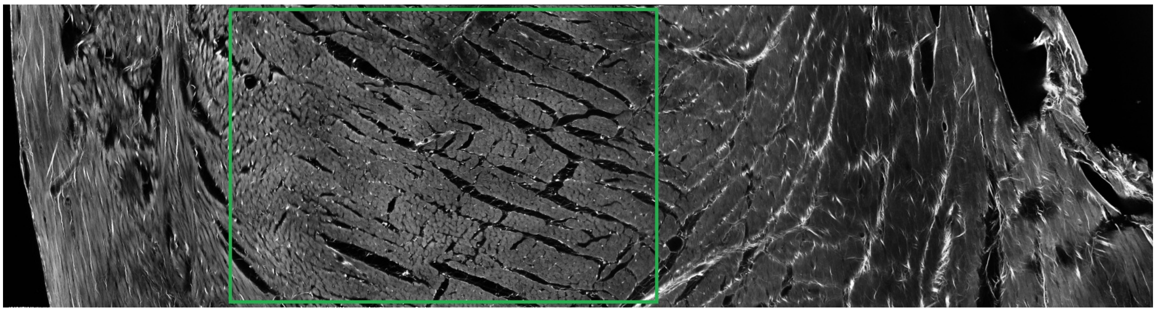

Figure 3.1: A single 2D slice from the micro-CT imaging dataset. The chosen ROI has been outlined in green.

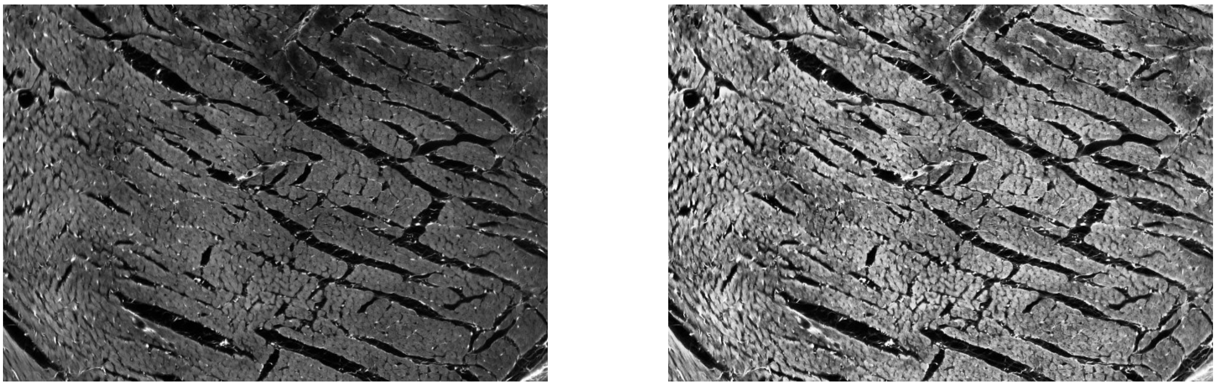

(a)

(b)

Figure 3.2: Example of a 2D image slice following the preprocessing: (a) the image after it has been cropped to focus on the ROI, (b) the cropped image after it has been CLAHE-enhanced.

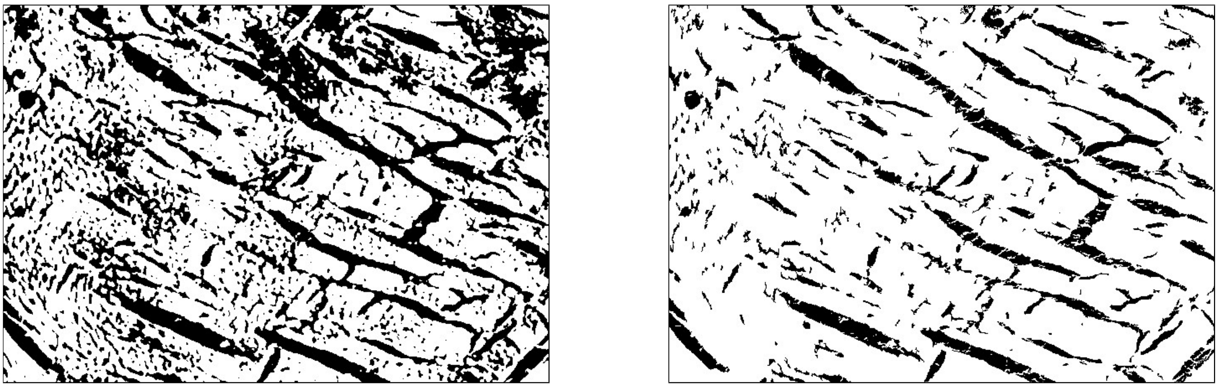

(a)

(b)

Figure 3.3: Example of a 2D image slice following image segmentation, with black pixels representing detected void regions and white pixels representing detected tissue regions: (a) the segmented image using Otsu's global thresholding method (b) the segmented image using a region-growing segmentation technique.

Each of the segmented images was compared to the preprocessed image seen in Figure 3.2b, to determine a preferential image segmentation method. Global thresholding using the Otsu's method performed well in identifying the cleavage planes and smaller gaps within the myocardial tissue. However, it led to certain regions being incorrectly detected as void, as can be seen in the upper centre and upper right sections of Figure 3.3a. The region-growing segmentation approach performed well in identifying the cleavage planes, but not as well in identifying smaller gaps within the myocardial tissue. Importantly, the region-growing segmentation approach did not lead to major misidentified void regions. This can be seen by comparing the upper centre and upper right sections of the preprocessed image in Figure 3.2b to those of the thresholded image (Figure 3.3a) and region-grown image (Figure 3.3b). Consequently, the region-grown segmented images were chosen for use in generating the realistic microstructural mesh.

Mesh generation using segmented imaging data

Using the region-grown segmented images, a realistic mesh was then generated via the process described in Section 2.1.3. The resulting mesh can be seen in Figure 3.4, where cells marked in red represent tissue, and cells marked in blue represent hydrogel. The mesh seen in Figure 3.4 has a size of 160 cells in the x, y, and z directions. This corresponds to dimensions of 0.386 mm in each of the longitudinal, radial, and circumferential directions of the original tissue block seen in Figure 2.3.

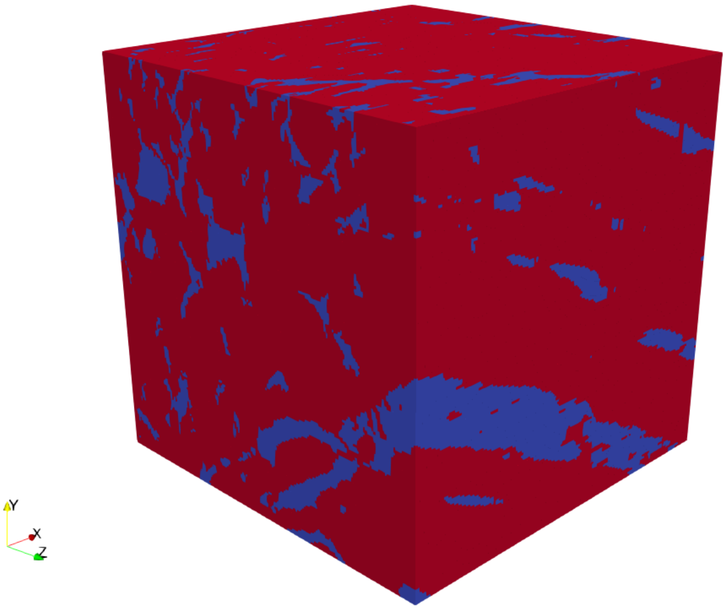

Figure 3.4: High-resolution mesh. Myocardium regions have been marked in red, and hydrogel regions have been marked in blue.

3.1.2 Myocardial fibre directions

The results of the methodology described in Section 2.1.3 - "Myocardial fibre directions" are presented here. Figure 3.5 shows the orientations of the cleavage planes for the imaging dataset used to determine appropriate fibre directions; as well as the resulting two-point correlation function, which describes the average orientation of these cleavage planes over the domain. It was observed that in Figure 3.5a, the longest axes of the cleavage planes roughly coincided with the x-axis direction, and that the two-point correlation function (Figure 3.5b) reflected this observation. It was further observed that in Figure 3.5a, the shortest axes of the cleavage planes roughly coincided with the y-axis direction, and that the two-point correlation function (Figure 3.5b) reflected this observation as well.

Using the two-point correlation function, the most and least probable relative directions for two points belonging to a cleavage plane were determined. These correspond to the most likely fibre $\boldsymbol{f}_0$ and sheet-normal $\boldsymbol{n}_0$ directions respectively. To determine these directions, the two-point correlation function was integrated along lines spanning $r \in [-10, 10]$ in spherical co-ordinates, by varying the polar angle θ and the azimuthal angle ϕ. The result of this integration can be visualised as a function of θ and ϕ (in radians), as seen in Figure 3.6. The vertical and horizontal axes represent θ and ϕ values respectively, ranging from $[0, 2\pi]$ radians.

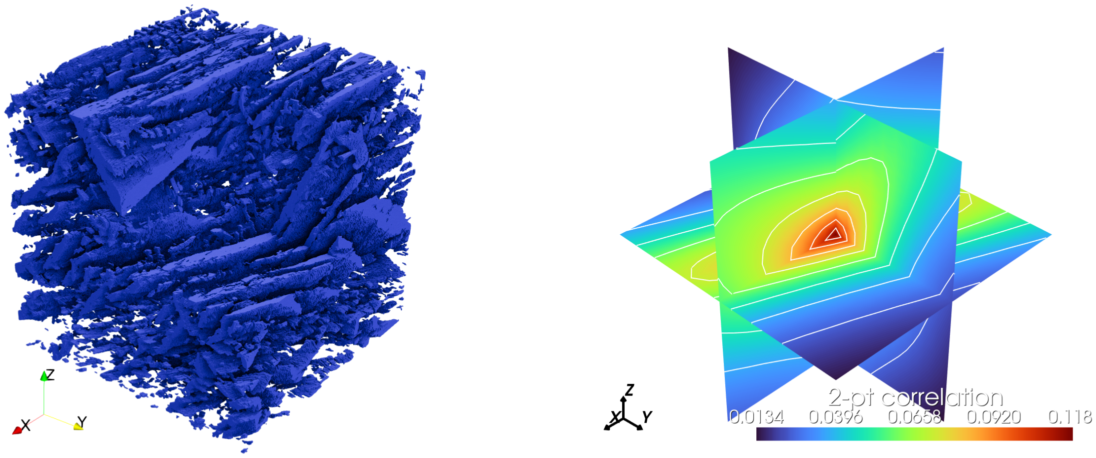

(a) (b)

Figure 3.5: Visualisations of (a) the orientations of the cleavage planes for the imaging dataset used to compute fibre directions and (b) slices of the calculated two-point correlation function, with contour lines corresponding to the average orientations of the cleavage planes.

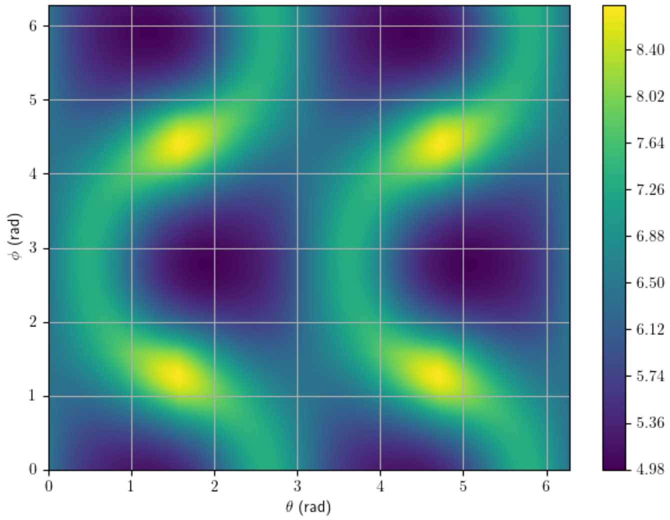

Figure 3.6: Function resulting from the integration of the two-point correlation function in spherical co-ordinates.

The θ and ϕ values which produced the maximum and minimum values for the function seen in Figure 3.6, were used to determine the fibre $\boldsymbol{f}_0$ and sheet-normal $\boldsymbol{n}_0$ directions, respectively. These are:

$$(\theta, \phi)_{\boldsymbol{f}_0} := \underset{\theta,\phi}{\arg\max} \int_{-w}^{w} \mathcal{S}\left(\boldsymbol{r}\left(r, \theta, \phi\right)\right) \,\mathrm{d}r = (4.70, 1.26) \text{ rad}, \tag{3.1.1}$$

$$(\theta, \phi)_{\boldsymbol{n}_0} = \underset{\theta,\phi}{\arg\min} \int_{-w}^{w} \mathcal{S}\left(\boldsymbol{r}\left(r, \theta, \phi\right)\right) \,\mathrm{d}r = (4.36, 5.92) \text{ rad}\,. \tag{3.1.2}$$

The sheet axis $\boldsymbol{s}_0$ was then computed as the cross-product of the $\boldsymbol{f}_0$ and $\boldsymbol{n}_0$ directions. The resulting directions were given in Equation (2.1.5) as:

$$\boldsymbol{f}_0 = \begin{bmatrix} -0.95199538 \\ 0.30601061 \\ -0.00789337 \end{bmatrix}, \quad \boldsymbol{n}_0 = \begin{bmatrix} 0.33220323 \\ 0.87674863 \\ -0.34778276 \end{bmatrix}, \quad \boldsymbol{s}_0 = \begin{bmatrix} 0.09950472 \\ 0.33370978 \\ 0.93631836 \end{bmatrix}.$$

To allow for a visualisation of the computed aggregate fibre directions against the cleavage planes of the microstructure, the fibre directions given by Equation (2.1.5) were superimposed onto the cleavage plane geometry seen in Figure 3.5a. The resulting visualisation can be seen in Figure 3.7. Figure 3.7 provides a clearer indication that the fibre axis $\boldsymbol{f}_0$ corresponds with the aggregate longest axes of the cleavage planes, and that the sheet-normal axis $\boldsymbol{n}_0$ corresponds with the aggregate shortest axes of the cleavage planes. This agreement between the axes of the cleavage planes and the computed fibre directions was not true for every cleavage plane in the geometry, as not all cleavage planes are perfectly aligned with each other. However, it provides a reasonable description of the aggregate orientations of the cleavage planes.

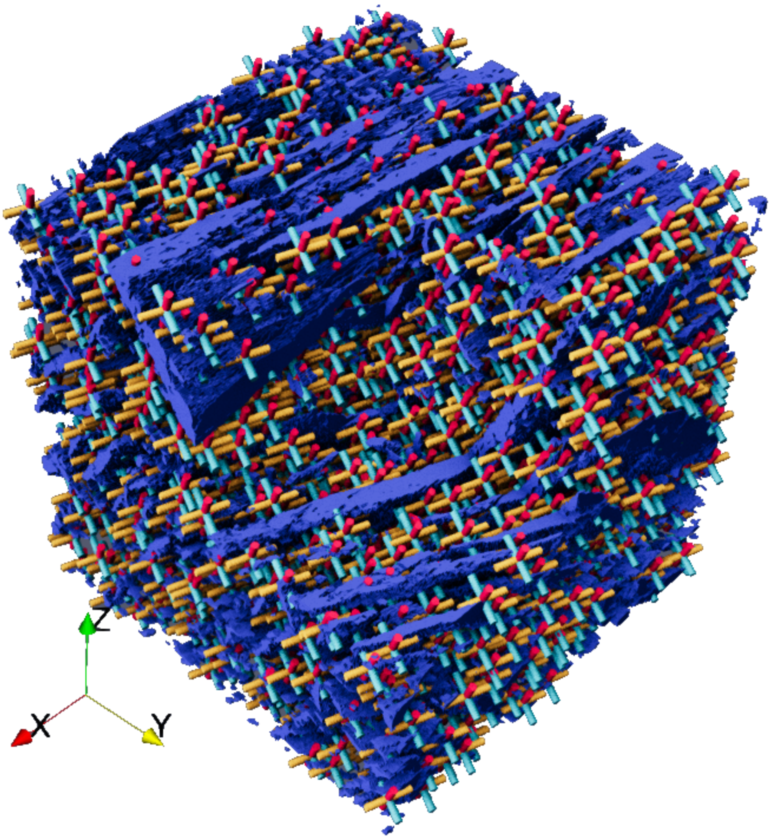

Figure 3.7: Visualisation of fibre directions obtained by the method described in Section 2.1.3 - “Myocardial fibre directions”. Here, $\boldsymbol{f}_0$, $\boldsymbol{n}_0$, and $\boldsymbol{s}_0$, are illustrated in orange, light blue, and red, respectively.

3.1.3 Development of an idealised mesh

The method described in Section 2.1.4 was used to generate an idealised mesh representing a myocardial tissue block with a cylindrical hydrogel inclusion. The resulting idealised mesh is shown in Figure 3.8, and was comprised of 163 840 elements, and 513 315 corresponding degrees-of-freedom. The overall mesh was of unit length, width, and height, and the diameter of the cylindrical inclusion was set as half the total width.

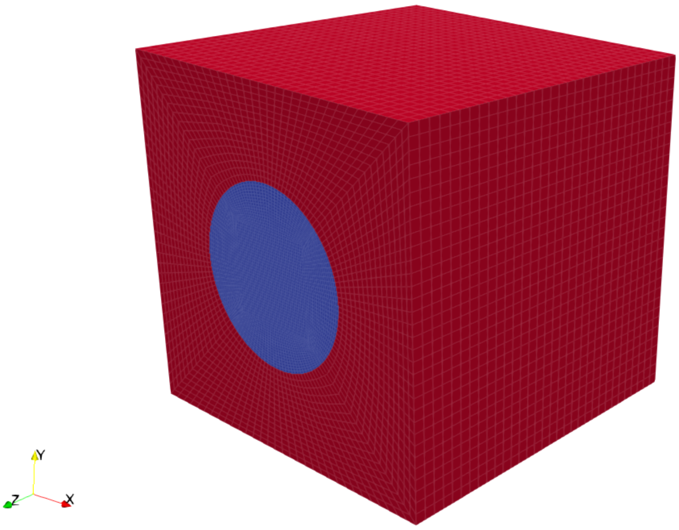

Figure 3.8: Idealised mesh of a myocardial tissue block with a cylindrical inclusion. Myocardium regions have been marked in red, and hydrogel regions have been marked in blue.

3.2 Application of developed framework

3.2.1 Obtaining boundary conditions

As described in Section 2.3.1, cardiac strain data were extracted from an existing macroscale ABAQUS model of rat myocardium, in order to develop KUBCs which could be applied to the finite-element meshes seen in Figures 3.4 and 3.8. Following a k-means clustering procedure, five cluster centres were identified and used to develop the case studies described in Section 2.3.2. For the case studies conducted on the idealised mesh, the full time-dependent dataset of Cluster Centre 3 was used. For the case studies conducted on the realistic mesh, the peak magnitude values for each of the five cluster centres was used. This was done to ensure that the simulations conducted on the realistic mesh were computationally feasible; using the full time-dependent dataset with the realistic mesh was not possible in the present study, due to the large number of elements and corresponding degrees-of-freedom. Figure 3.9 shows the spatial stretch tensor magnitudes over time for the five cluster centres, as well as the peak strain state for each cluster centre.

At the peak strain state for each cluster centre, the left stretch tensors are given in Equations (3.2.1) to (3.2.5).

$$V_{\mathrm{CC1,max}} = \begin{pmatrix} 0.861481 & 0.076443 & 0.103362 \\ 0.076443 & 1.124320 & -0.064254 \\ 0.103362 & -0.064254 & 1.055932 \end{pmatrix}, \tag{3.2.1}$$

$$V_{\mathrm{CC2,max}} = \begin{pmatrix} 0.913569 & -0.274150 & -0.040314 \\ -0.274150 & 1.239535 & 0.555825 \\ -0.040314 & 0.555825 & 1.203099 \end{pmatrix}, \tag{3.2.2}$$

$$V_{\mathrm{CC3,max}} = \begin{pmatrix} 0.855035 & -0.372873 & 0.096664 \\ -0.372873 & 1.242893 & -0.241036 \\ 0.096664 & -0.241036 & 1.130165 \end{pmatrix}, \tag{3.2.3}$$

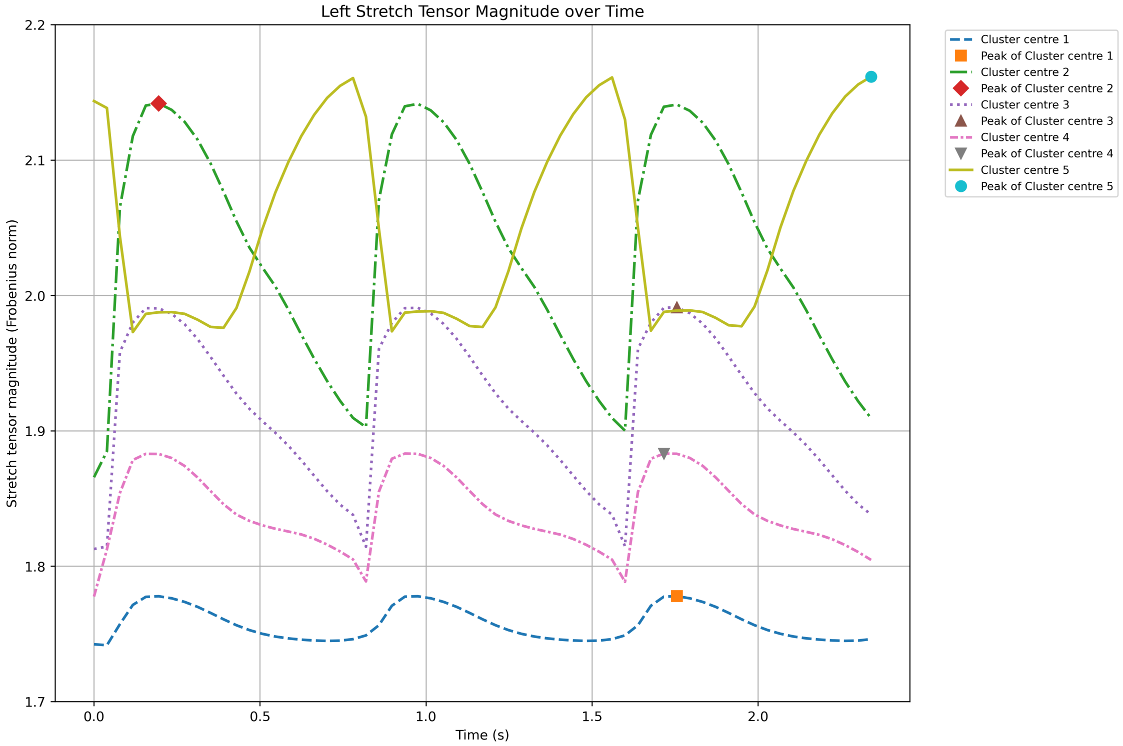

Figure 3.9: Spatial stretch tensor magnitudes (Frobenius norm) over time for the cluster centres, with peak magnitudes marked.

$$V_{\text{CC4,max}} = \begin{pmatrix} 0.851275 & -0.065039 & 0.274355 \\ -0.065039 & 1.247821 & -0.111200 \\ 0.274355 & -0.111200 & 1.040144 \end{pmatrix}, \tag{3.2.4}$$

$$V_{\text{CC5,max}} = \begin{pmatrix} 1.066346 & 0.619740 & 0.092060 \\ 0.619740 & 1.243191 & -0.083204 \\ 0.092060 & -0.083204 & 1.091142 \end{pmatrix}. \tag{3.2.5}$$

The Frobenius norms of the peak left stretch tensors for each cluster centre are shown in Equation (3.2.6).

$$\begin{aligned} ||V_{\text{CC1,max}}||_F &= 1.778335\,, \\ ||V_{\text{CC2,max}}||_F &= 2.142418\,, \\ ||V_{\text{CC3,max}}||_F &= 1.991505\,, \\ ||V_{\text{CC4,max}}||_F &= 1.883443\,, \\ ||V_{\text{CC5,max}}||_F &= 2.161518\,. \end{aligned} \tag{3.2.6}$$

3.2.2 Case studies

The following section presents the results of the computational case studies described in Section 2.3.2. Two case studies were conducted, and the simulations can be categorised as follows:

1. Case study 1 - Simulations conducted on the idealised mesh depicted in Figure 3.8, using KUBCs which describe a time-dependent set of strain states. This set of strain states was from Cluster Centre 3, which can be seen in Figure 3.9.

2. Case study 2 - Simulations conducted on the detailed microstructural mesh depicted in Figure 3.4, using KUBCs which describe a single strain state. These single strain states were chosen as the peak values shown in Figure 3.9, as described in Equations (3.2.1) to (3.2.5).

For each of these case studies, the results generated by the developed computational tool can be grouped in the following manner:

1. Results relating to the homogenised response of the FE solution. These include the homogenised deformation gradient, as well as the homogenised first Piola-Kirchhoff stress response. It is worth reiterating that the present study did not look to determine a representative size for the volume element. As such, we do not claim that the observed behaviour is the effective behaviour.

2. Results computed at the nodes and quadrature points of the FE solution. These include the displacement and strain calculated at each node; and the Kirchhoff stress calculated at each quadrature point.

Case study 1 - Idealised geometry with time-dependent KUBCs applied

Using the idealised mesh shown in Figure 3.8 and the time-dependent KUBC given by Cluster Centre 3 in Figure 3.9, two simulations were conducted, as described in Section 2.3.2. In the first, the isotropic, Neo-Hookean model described by Equations (2.2.38) and (2.2.39) was used to describe both the hydrogel injectate and the myocardium. In the second, the isotropic, Neo-Hookean model described by Equations (2.2.38) and (2.2.39) was used to describe the hydrogel injectate, and the anisotropic model described by Equations (2.2.45) and (2.2.46) was used to describe the myocardium.

Homogenised results

The components of the left stretch tensor for the KUBC and the components of the resulting homogenised deformation gradient are shown in Figure 3.10, which indicates that the applied KUBC was resolved correctly for both idealised simulations across the full time range. The components of the observed homogenised deformation gradient (dotted lines) equalled the components of the applied KUBC left stretch tensor (solid lines) for the case in which (a) only isotropic material models were used (Figure 3.10a) and (b) isotropic and anisotropic material models were used (Figure 3.10b).

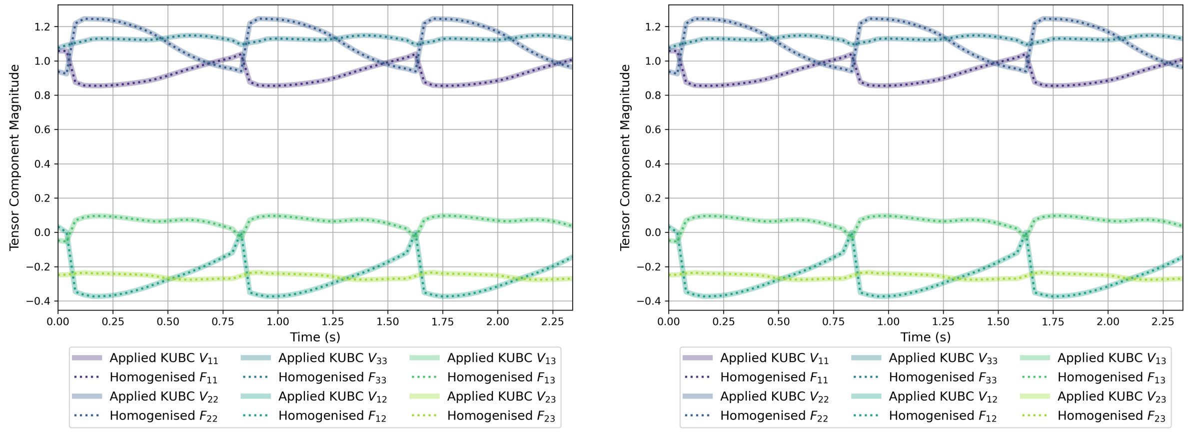

(a) (b)

Figure 3.10: Comparison of the components of the applied KUBC left stretch tensor (solid lines) and the resulting homogenised deformation gradient (dotted lines) over time using (a) only isotropic material models and (b) isotropic and anisotropic material models.

Using the homogenised deformation gradient and the homogenised first Piola-Kirchhoff stress response, the homogenised Cauchy stress response, $\boldsymbol{\sigma}_{\text{hom}}$, was calculated as:

$$\boldsymbol{\sigma}_{\text{hom}} = \frac{1}{J} \langle \boldsymbol{P}_m \rangle \, \boldsymbol{F}_M^T \, . \tag{3.2.7}$$

Where $\langle \boldsymbol{P}_m \rangle$ is the homogenised first Piola-Kirchhoff stress, $\boldsymbol{F}_M$ is the homogenised deformation gradient, and J is the determinant of the homogenised deformation gradient.

The components of the homogenised Cauchy stress tensor over time have been shown for each simulation in Figure 3.11. When the anisotropic model was introduced (Figure 3.11b), the absolute magnitudes of the observed homogenised Cauchy stress components increased. Moreover, the evolution of the stress components to and from their peak magnitudes was more gradual when the anisotropic model was introduced, as compared to when only isotropic material models were used. It is worth noting that the anisotropic model includes exponential terms, whereas the isotropic, Neo-Hookean model, does not, which may be the cause for the observed differences in the shapes of the stress responses. One possible explanation is that, when deformations are large (for example during peak ventricular contraction), the inclusion of the exponential terms may lead to significantly increased stresses when compared to models which do not include any exponential terms.

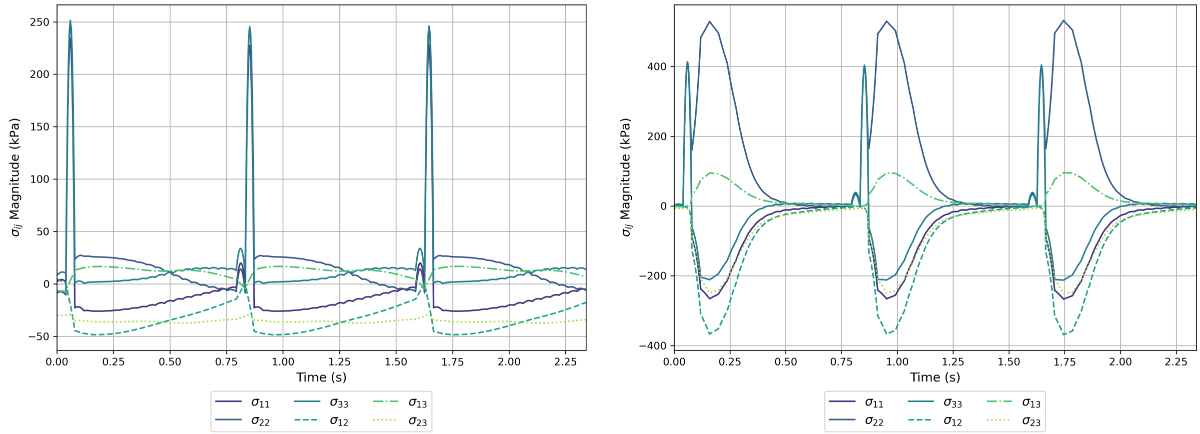

(a) (b)

Figure 3.11: Homogenised Cauchy stress components over time using (a) only isotropic material models and (b) isotropic and anisotropic material models.

The eigenvalues of the homogenised Cauchy stress tensor were calculated, and correspond to the homogenised principal stresses σ_1, σ_2 and σ_3, where $\sigma_1 \geq \sigma_2 \geq \sigma_3$. Figure 3.12 shows the homogenised principal stresses over time for each simulation. Similar observations to those made for Figure 3.11 can be made for Figure 3.12; when the anisotropic material model was introduced, the stress magnitudes increased, and the stress evolutions to and from their peak magnitudes were more gradual.

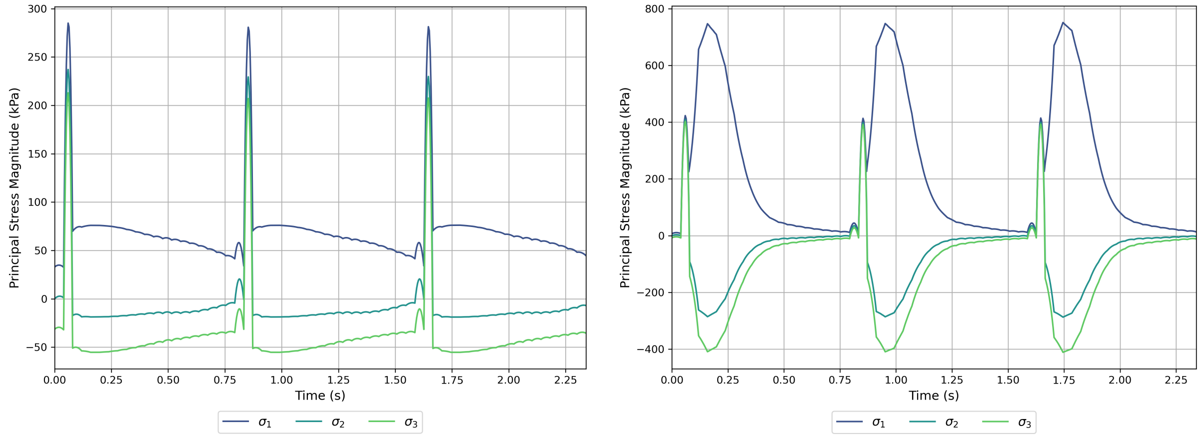

(a) (b)

Figure 3.12: Homogenised principal stresses over time using (a) only isotropic material models and (b) isotropic and anisotropic material models.

Using the homogenised principal stresses shown in Figure 3.12, the homogenised von Mises stress was calculated using Equation (3.2.8).

$$\sigma_v = \sqrt{\frac{(\sigma_1 - \sigma_2)^2 + (\sigma_2 - \sigma_3)^2 + (\sigma_3 - \sigma_1)^2}{2}}\,. \tag{3.2.8}$$

Figure 3.13 shows the homogenised von Mises stress over time for both simulations, with nine selected sampling points. These sampling points were chosen to allow the presentation of quadrature point stress results in Section 3.2.2 over a fixed number of time steps, intended to span a single cardiac cycle. The first and last sampling points were determined by calculating the local minima of the homogenised von Mises stress results at $t = 0.837$s and $t = 1.630$s. The remaining seven sampling points were linearly spaced within this interval.

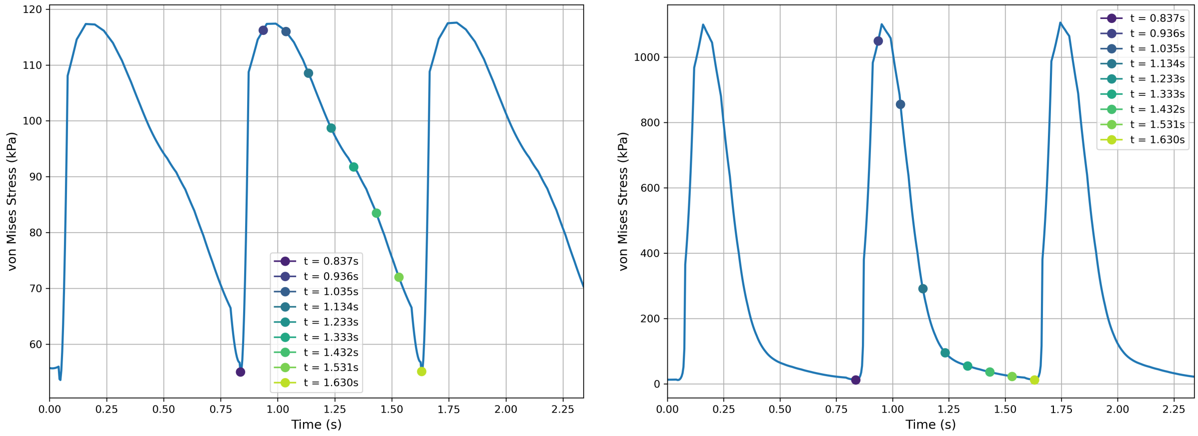

(a) (b)

Figure 3.13: Homogenised von Mises stress over time using (a) only isotropic material models and (b) isotropic and anisotropic material models.

Quadrature point-specific results

In addition to the homogenised results presented above, the developed computational tool produces a dataset at each time step containing the following information for each quadrature point:

- Global index
- Material type
- Kirchhoff stress tensor components and magnitude

Focus has been given to the distributions of the magnitudes of the Kirchhoff stress tensors, and on demonstrating how these can be extracted for each material type. These were deemed to be important in evaluating conditions under which the observed stresses exceeded reasonable elastic limits, as well as in comparing the mechanical response of the myocardium and hydrogel domains. For each of the nine sampling points shown in Figure 3.13, the Kirchhoff stress magnitudes corresponding to the hydrogel and myocardium domains were determined. Using the free, open-source Python library, SciPy, a kernel density estimate (KDE) was computed for each set of magnitudes. In brief, this provides an estimation of the probability density function of a random variable, in this case, the magnitude of the Kirchhoff stress tensor. Figure 3.14 shows the KDEs for each of the myocardium and hydrogel regions, at each of the nine sampling points defined in Figure 3.13. Intuitively, the higher the probability density, the more frequently stress magnitudes in that range occur, and the total area under each KDE is always equal to one. It should be noted that the bandwidth used to generate the KDEs seen in Figure 3.14 was the default SciPy method, which aims to produce a smooth but representative estimate of the probability density function. Additionally, to allow for the KDEs in Figure 3.14 to be shown on the same set of axes, they were scaled to be of uniform height without changing the form of the underlying distributions.

It was observed that, in Figure 3.14, the quadrature point Kirchhoff stresses were concentrated within a narrower range when only an isotropic model was used (Figure 3.14a), as opposed to when an anisotropic model was introduced for the myocardium (Figure 3.14b). It is worth reiterating that the anisotropic model included exponential terms, whereas the Neo-Hookean model did not.

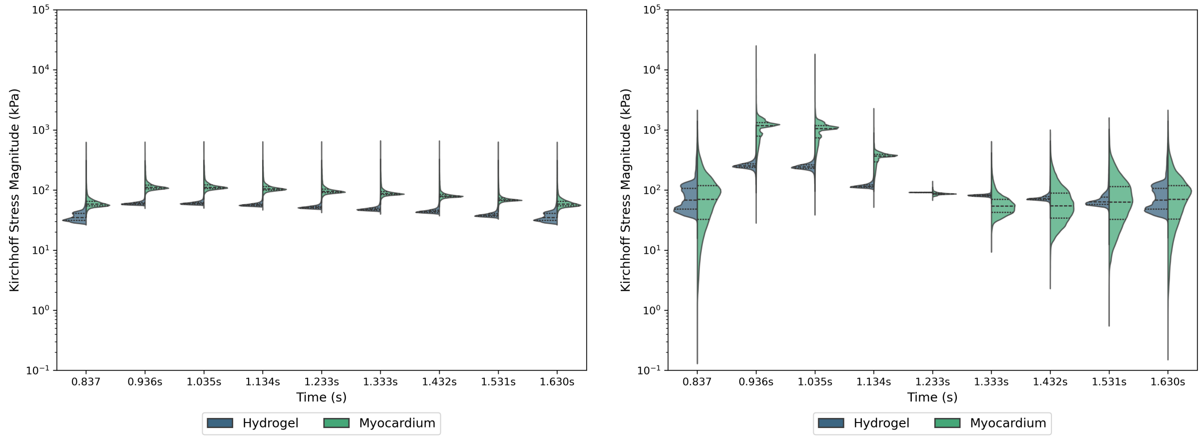

(a) (b)

Figure 3.14: Quadrature point stress distributions over one cardiac cycle using (a) only isotropic material models and (b) isotropic and anisotropic material models.

The combined set of Kirchhoff stress magnitudes across the myocardium and hydrogel regions have been shown for each sampling point in Figure 3.15, with the median values marked. In a similar manner to Figure 3.14, it was observed that, when an anisotropic model was introduced for the myocardium (Figure 3.15b), both the variation in the median Kirchhoff stress values, as well as the range of the Kirchhoff stress distribution, increased compared to the case where only isotropic models were used (Figure 3.15a).

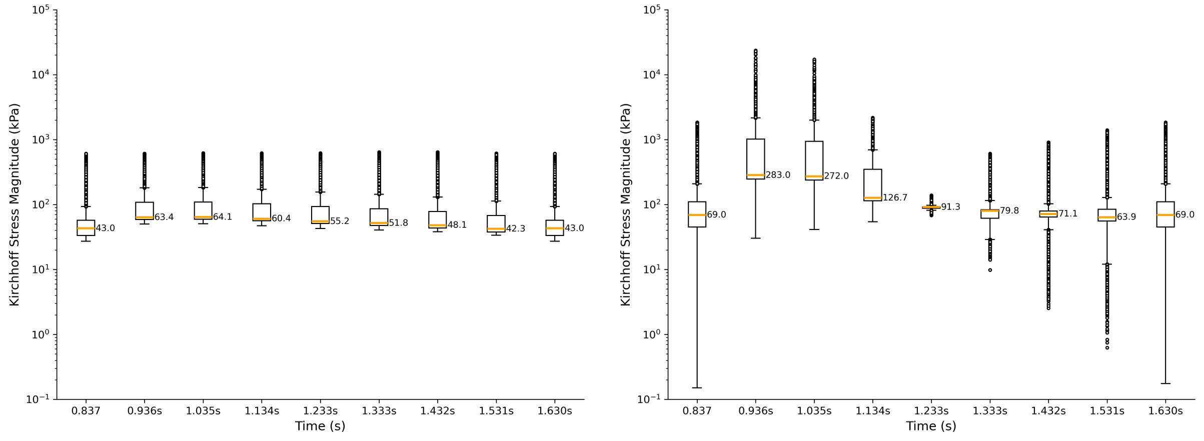

(a) (b)

Figure 3.15: Box-plot of quadrature point stress distributions over one cardiac cycle using (a) only isotropic material models and (b) isotropic and anisotropic material models.

Figure 3.16 provides a visualisation of the Kirchhoff stress magnitudes on the undeformed, idealised mesh, at the second sampling point ($t = 0.936$s). This sampling point was chosen as it most closely coincides with the peak von Mises stress shown in Figure 3.13b. It can be seen that the peak Kirchhoff stress magnitude values occur on and around the boundary between the hydrogel and myocardium regions.

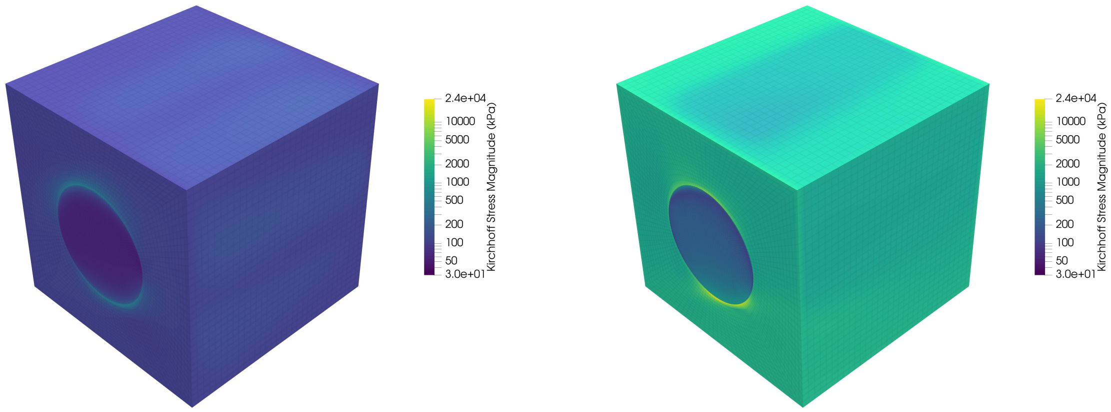

(a) (b)

Figure 3.16: Kirchhoff Stresses on the Undeformed Geometry at $t = 0.936$s using (a) only isotropic material models and (b) isotropic and anisotropic material models.

Case study 2 - Realistic geometry with single strain state KUBCs applied

Using the realistic microstructural mesh shown in Figure 3.4, five simulation scenarios, as described in Section 2.3.2 were considered. Each of these scenarios corresponds to the application of a KUBC for the maximum strain state of one of the cluster centres shown in Figure 3.9. In this section, these scenarios are referred to as “Cluster Centre 1”, “Cluster Centre 2”,…“Cluster Centre 5” representing which of the five maximum strain states shown in Figure 3.9 has been applied as the KUBC. All the simulations conducted on the realistic mesh made use of the isotropic, Neo-Hookean model given by Equations (2.2.38) and (2.2.39) in describing the hydrogel, and the anisotropic model given by Equations (2.2.45) and (2.2.46) in describing the myocardium. For each scenario, three hydrogel material parameter simulations were considered, described in Table 2.2. These are referred to as the “Lower-bound”, “Median”, and “Upper-bound” stiffness cases, corresponding to hydrogel elastic moduli of $E = 5$ kPa, $E = 50$ kPa, and $E = 100$ kPa respectively. For all hydrogel stiffness cases, the Poisson’s ratio used for the hydrogel was $\nu = 0.49$, the parameters for the anisotropic model for the myocardium were those described in Table 2.1, and the anisotropic fibre directions were those shown in Equation (2.1.5).

Homogenised results

For each simulation, the homogenised deformation gradient at the final time step was compared to the left stretch tensor of the applied KUBC. The starting deformation gradient in each simulation was the identity matrix $\boldsymbol{I}$, and application of the KUBC left stretch tensor was done through linear increments. For context, certain simulations, specifically Cluster Centre 2 and Cluster Centre 5, led to comparatively larger deformations in the myocardium. This, combined with the exponential nature of the anisotropic model used to describe the myocardium, led to unacceptably small time steps being required for the solver to completely resolve the target strain state. In these cases, the simulations were terminated prematurely, and the results at the final time step prior to termination have been reported. The “% Achieved” quantity represents to what extent the solver was able to resolve the target strain state, and was defined as follows:

$$\%\ \text{Achieved} := \frac{\|\bar{\boldsymbol{F}} - \boldsymbol{I}\|}{\|\boldsymbol{V} - \boldsymbol{I}\|} \times 100\,.$$

Where $\bar{\boldsymbol{F}}$ is the homogenised deformation gradient at the final time step and $\boldsymbol{V}$ is the target applied KUBC left stretch tensor. Table 3.1 provides a summary of the agreement between the achieved homogenised deformation gradient and the target applied KUBC left stretch tensor.

Table 3.1: Table showing the degree (%) to which the target strain state was achieved for each computational case. The values in the final column indicate the magnitude of each component of the homogenised deformation gradient result when compared to the components of the applied KUBC left stretch tensor. The elastic modulus E refers to the elastic modulus used for the isotropic, Neo-Hookean model. For all simulations, the Poisson's ratio $\nu = 0.49$ was used for the isotropic, Neo-Hookean model.

Applied KUBC	Hydrogel Stiffness Case	E (kPa)	% Achieved
Cluster Centre 1 Maximum	Lower-bound	5	100.0%
	Median	50	100.0%
	Upper-bound	100	100.0%
Cluster Centre 2 Maximum	Lower-bound	5	11.0%
	Median	50	68.8%
	Upper-bound	100	70.0%
Cluster Centre 3 Maximum	Lower-bound	5	100.0%
	Median	50	100.0%
	Upper-bound	100	100.0%
Cluster Centre 4 Maximum	Lower-bound	5	100.0%
	Median	50	100.0%
	Upper-bound	100	100.0%
Cluster Centre 5 Maximum	Lower-bound	5	16.0%
	Median	50	91.3%
	Upper-bound	100	92.0%

The results shown in Table 3.1 have been illustrated in Figure 3.17 where, for each scenario, the components of the applied KUBC left stretch tensor have been shown alongside the homogenised deformation gradient result achieved for each hydrogel stiffness case. For Cluster Centre 1 (Figure 3.17a), Cluster Centre 3 (Figure 3.17c), and Cluster Centre 4 (Figure 3.17d) the targeted KUBC tensor was fully resolved for all hydrogel stiffness cases. As such, the outcomes of each hydrogel stiffness case can be compared to each other. In the remaining Cluster Centre 2 (Figure 3.17b) and Cluster Centre 5 (Figure 3.17e) cases, the homogenised deformation gradients for each hydrogel stiffness case did not reach the same values, as indicated in Table 3.1. Therefore, in these cases, the results of the hydrogel stiffness cases cannot be directly compared to each other. However, one can still evaluate the results of these simulations to observe the stress distributions and identify any excessively large stress values, which may indicate that the assumption of elastic material behaviour is insufficient in those cases.

Figure 3.18 shows the homogenised principal stresses and homogenised von Mises stress, calculated at the final time step of each hydrogel stiffness case. For Cluster Centres 1 (Figure 3.18a), 3 (Figure 3.18c), and 4 (Figure 3.18d), the homogenised principal and von Mises stresses increased with increasing hydrogel stiffness. It is important to note that, as per Table 3.1, the stiffness cases for Figures 3.18b and 3.18e cannot be directly compared as they did not reach the same final strain state. However it can be noted that the observed principal and von Mises stresses for Cluster Centre 2 (Figure 3.18b) and Cluster Centre 5 (Figure 3.18e) were considerably larger than the remaining scenarios.

Quadrature point-specific results

For each of the simulations summarised in Table 3.1, the distributions of the quadrature point Kirchhoff stress magnitudes for the hydrogel, myocardium and total regions are illustrated in Figure 3.19. The KDEs resulting from each hydrogel stiffness case have been displayed on common stress axes for each cluster centre case. It is important to note that, as per Table 3.1, the "Lower-bound", "Median", and "Upper-bound" cases for Figures 3.19b and 3.19e did not reach the same targeted strain state.

The Kirchhoff stress magnitudes are illustrated further in the form of box-plots for the hydrogel, my-

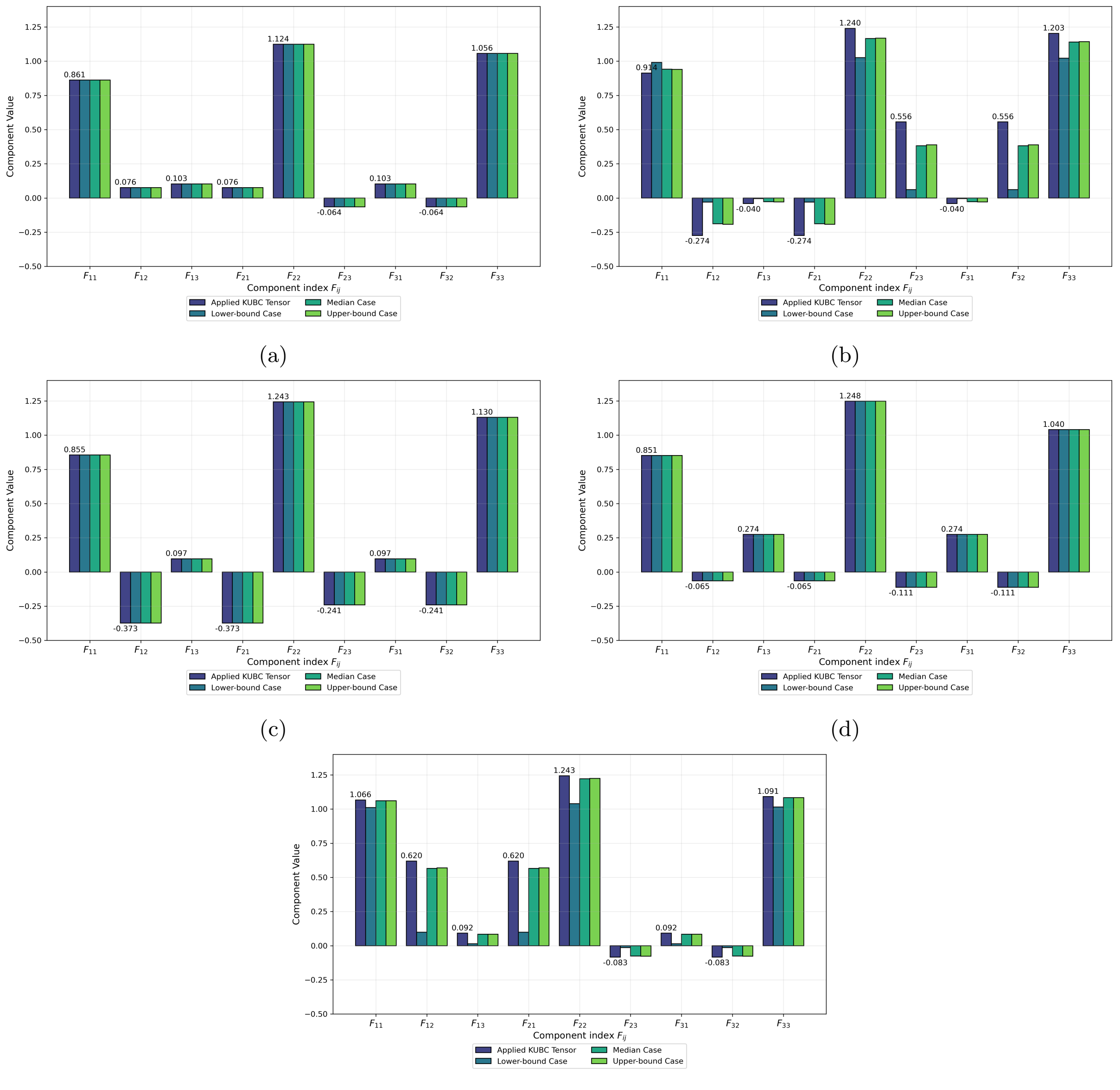

(a) (b) (c) (d) (e)

Figure 3.17: Components of the applied KUBC left stretch tensor alongside the components of the homogenised deformation gradient result for each hydrogel stiffness case of (a) Cluster Centre 1, (b) Cluster Centre 2, (c) Cluster Centre 3, (d) Cluster Centre 4, and (e) Cluster Centre 5.

ocardium, and total regions, in Figure 3.20. The box-plots include the outliers from each dataset, providing an indication of the overall range of observed stress values. This range is not necessarily apparent in the KDEs of Figure 3.19, as the number of outliers is small compared to the total number of stress values. Although Figure 3.19 and Figure 3.20 depict the same set of results, they offer different insights: the KDEs emphasize the shapes of the distributions of the stress magnitudes, while the box-plots more clearly indicate the spread of the data and outliers in the stress magnitude data. It is worth noting that for Cluster Centre 2 (Figure 3.20b), Cluster Centre 3 (Figure 3.20c), and Cluster Centre 5 (Figure 3.20e), the outlying stress magnitudes were often far greater than the median stress values (i.e. $\tau_{\max} \gg \tau_{\text{median}}$). In these cases, the outlying stress magnitudes exceeded 1×10^5 kPa. For reference, tensile tests conducted on human coronary artery samples by Karimi et al. (2013) reported a maximum ultimate strength of 3.59×10^3 kPa. Even though their study did not make use of rat myocardium specifically, it provides a broad indication of the reasonable elastic limits of soft tissue. This suggests that, under certain loading conditions, the stresses observed in the simulations far exceed reasonable elastic limits, and that the assumption of elastic material behaviour may be insufficient.

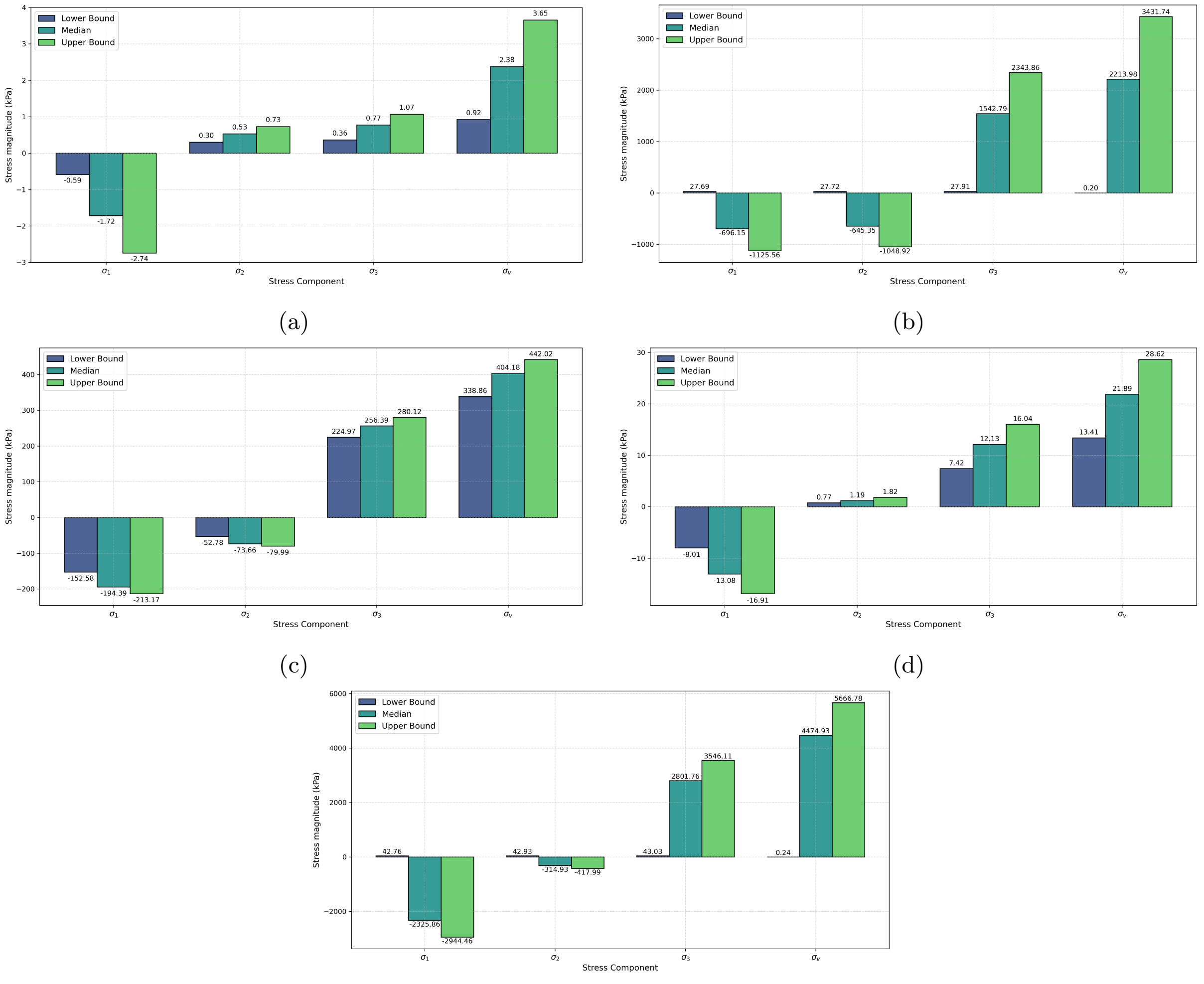

(a) (b)

(c) (d)

(e)

Figure 3.18: Homogenised principal and von Mises stresses for each hydrogel stiffness case of (a) Cluster Centre 1, (b) Cluster Centre 2, (c) Cluster Centre 3, (d) Cluster Centre 4, and (e) Cluster Centre 5.

To allow for an improved visualisation of the distributions of the Kirchhoff magnitudes on the undeformed mesh, a segment corresponding to one-eighth of the total mesh volume was excluded from Figure 3.4. The material distributions of myocardium and hydrogel on the resulting mesh are shown in Figure 3.21. As a general observation, the peak stresses occurred on the boundaries between the myocardium and the hydrogel injectate, this is particularly noticeable in Figures 3.23, 3.24 and 3.26. In these cases, stresses in the boundary regions often exceeded 1×10^5 kPa.

Figures 3.22 to 3.26 show the distributions of the Kirchhoff stress magnitudes on the undeformed mesh for each case, and each hydrogel material parameter subcase. For Cluster Centre 1 (Figure 3.22) and Cluster Centre 4 (Figure 3.25), which represented the least strenuous loading conditions, the stresses in the hydrogel regions exceeded those in the myocardial regions, and increased with increasing hydrogel stiffness. For Cluster Centre 2 (Figure 3.23) and Cluster Centre 5 (Figure 3.26), which represented the most strenuous loading conditions, the peak stresses occurred on the boundary regions between the hydrogel and myocardium. These peak stresses correspond with the exceedingly large outlier values seen in Figure 3.20b and Figure 3.20e. It was observed that for Cluster Centre 3 (Figure 3.24), the stress distribution became increasingly homogenous as the hydrogel stiffness was increased. This can also be observed in Figure 3.19c, where the overall stress distribution narrowed as the hydrogel stiffness was increased.

To allow for a visualisation of the Kirchhoff stress magnitudes on the deformed mesh, a cubic segment was extracted from the original microstructural mesh. This segment, shown in Figure 3.27 shared the same centre as the original mesh, but has one-eighth the total volume. Figures 3.28 to 3.32 show the

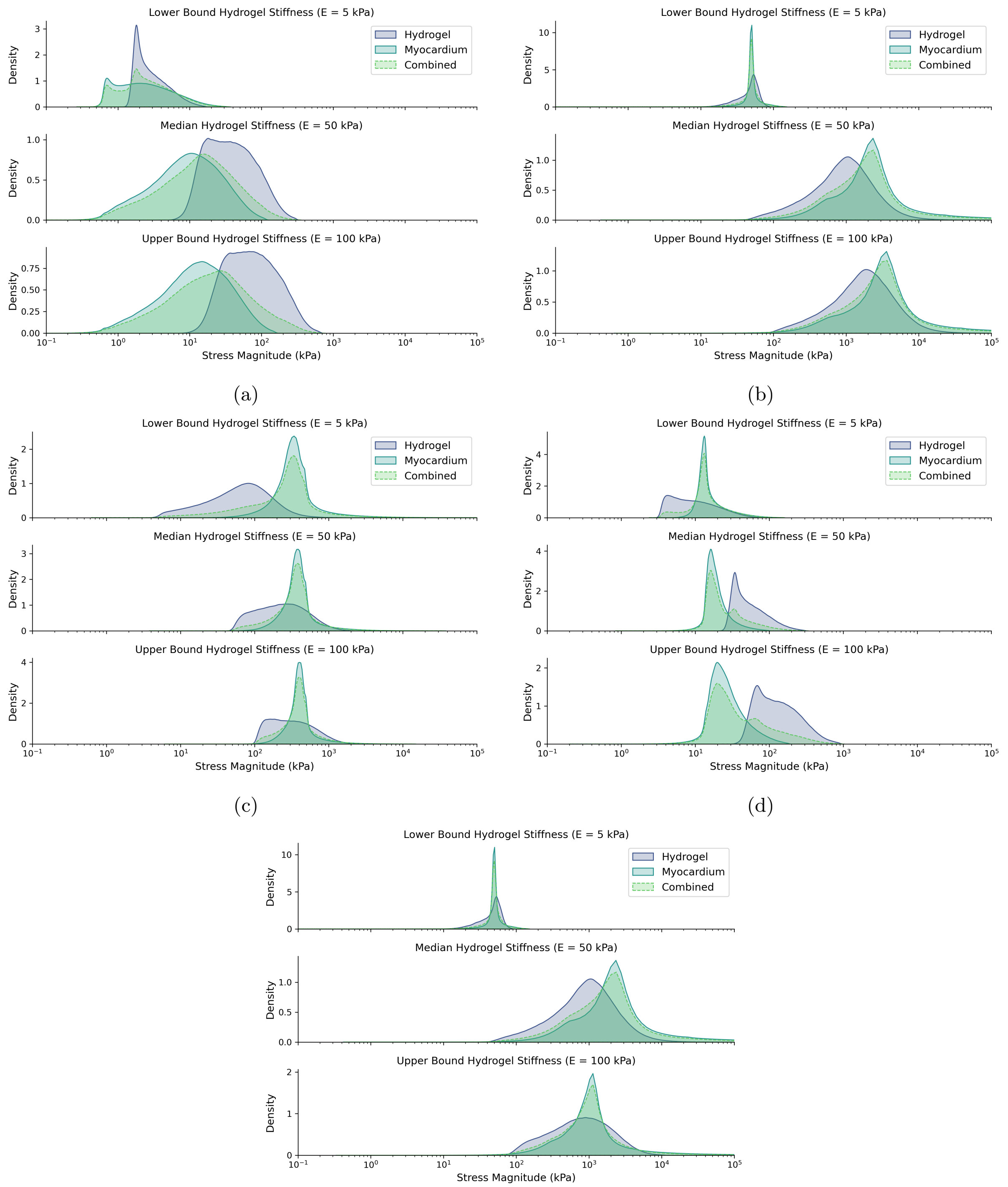

(a)

(b)

(c)

(d)

(e)

Figure 3.19: Quadrature point Kirchhoff stress distributions for each hydrogel stiffness case of (a) Cluster Centre 1, (b) Cluster Centre 2, (c) Cluster Centre 3, (d) Cluster Centre 4, and (e) Cluster Centre 5.

Kirchhoff stress distributions on this segment of the mesh in the deformed state. The same general observations made for the undeformed visualisations can be made for the deformed visualisations where, for example, stresses in excess of 1×10^5 kPa were primarily concentrated on the boundary regions between the myocardium and hydrogel. This is particularly apparent in Figures 3.29, 3.30 and 3.32.

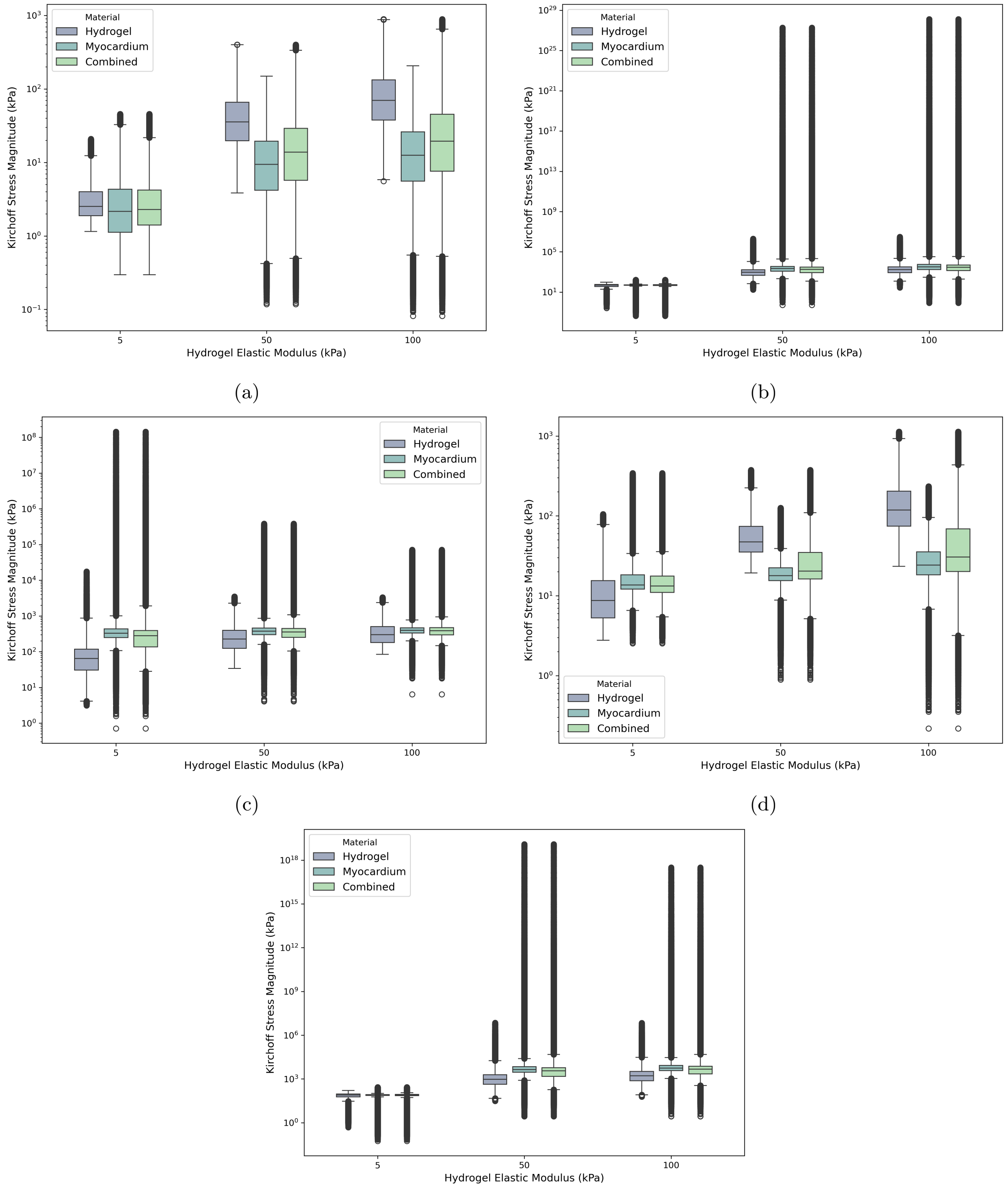

(a)

(b)

(c)

(d)

(e)

Figure 3.20: Quadrature point Kirchhoff stress distributions for each hydrogel stiffness case of (a) Cluster Centre 1, (b) Cluster Centre 2, (c) Cluster Centre 3, (d) Cluster Centre 4, and (e) Cluster Centre 5.

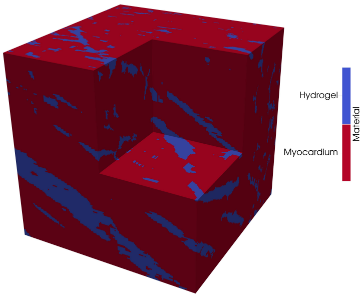

Figure 3.21: Material distributions on the undeformed mesh, with one-eighth of the volume excluded.

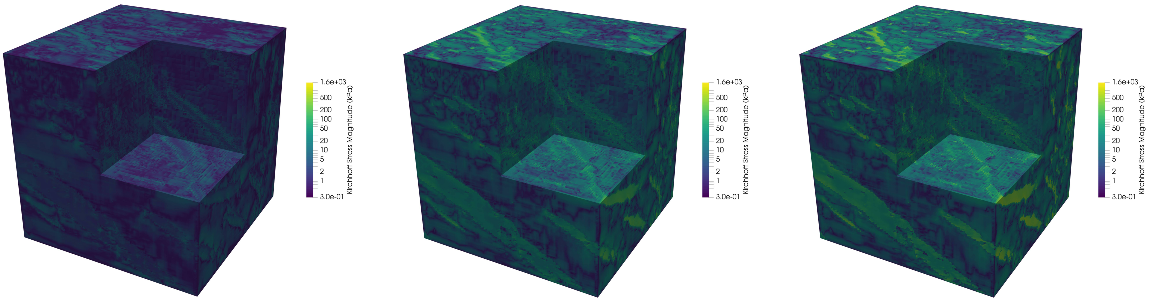

(a) (b) (c)

Figure 3.22: Visualisations of the Kirchhoff stress distributions for Cluster Centre 1, showing the results for the (a) lower-bound ($E = 5$kPa), (b) median ($E = 50$kPa), and (c) upper-bound ($E = 100$kPa) hydrogel stiffness cases.

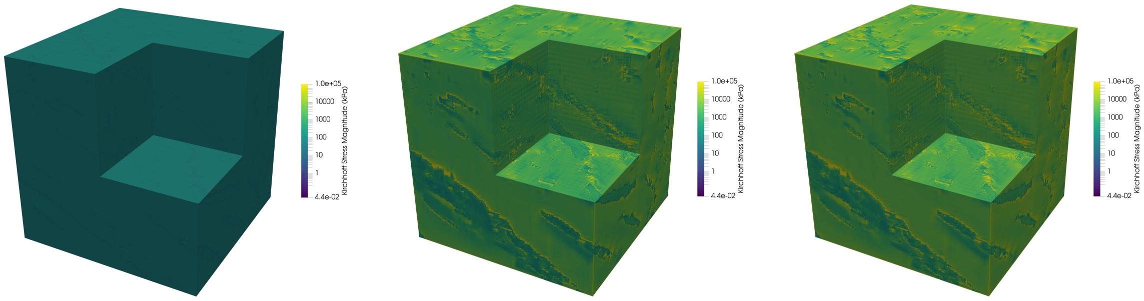

(a) (b) (c)

Figure 3.23: Visualisations of the Kirchhoff stress distributions for Cluster Centre 2, showing the results for the (a) lower-bound ($E = 5$kPa), (b) median ($E = 50$kPa), and (c) upper-bound ($E = 100$kPa) hydrogel stiffness cases.

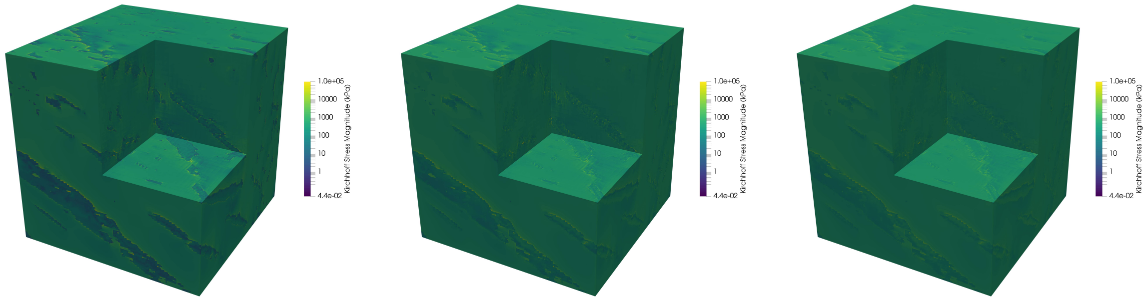

(a) (b) (c)

Figure 3.24: Visualisations of the Kirchhoff stress distributions for Cluster Centre 3, showing the results for the (a) lower-bound ($E = 5$kPa), (b) median ($E = 50$kPa), and (c) upper-bound ($E = 100$kPa) hydrogel stiffness cases.

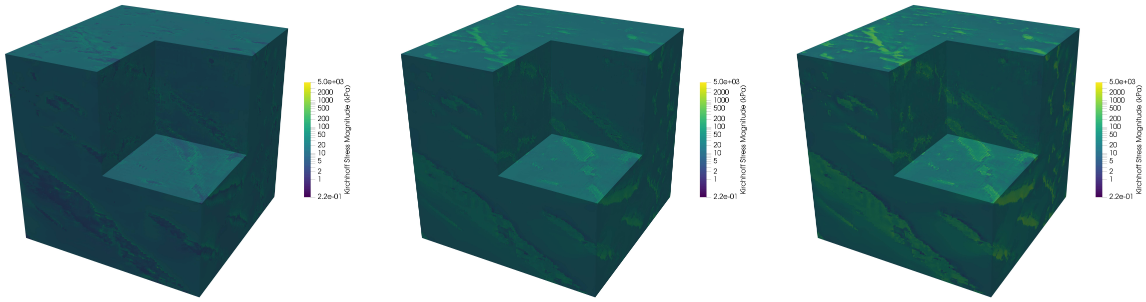

(a) (b) (c)

Figure 3.25: Visualisations of the Kirchhoff stress distributions for Cluster Centre 4, showing the results for the (a) lower-bound ($E = 5$kPa), (b) median ($E = 50$kPa), and (c) upper-bound ($E = 100$kPa) hydrogel stiffness cases.

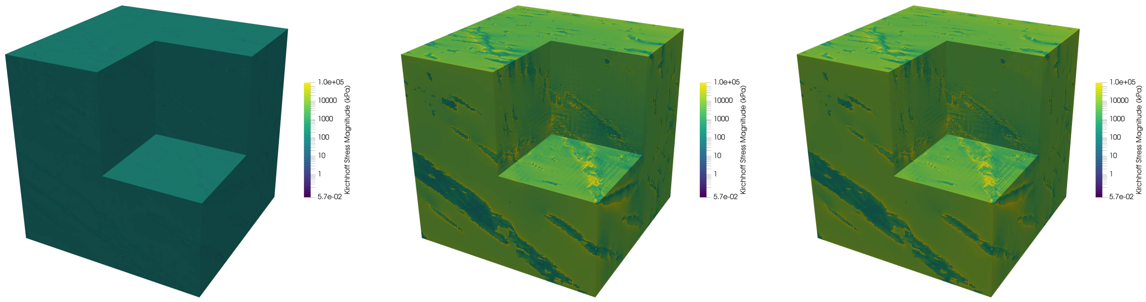

(a) (b) (c)

Figure 3.26: Visualisations of the Kirchhoff stress distributions for Cluster Centre 5, showing the results for the (a) lower-bound ($E = 5$kPa), (b) median ($E = 50$kPa), and (c) upper-bound ($E = 100$kPa) hydrogel stiffness cases.

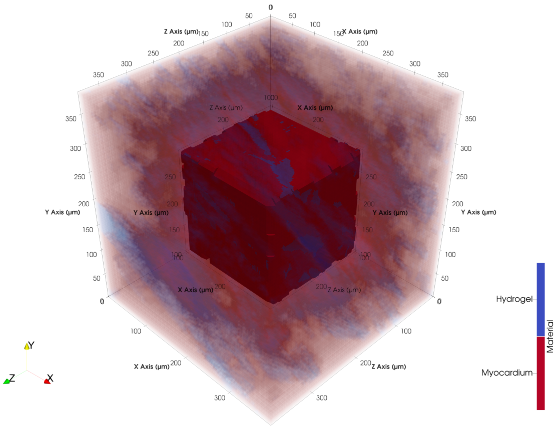

Figure 3.27: Segment of the original mesh used for deformed visualisations. The full-size mesh has been made semi-transparent.

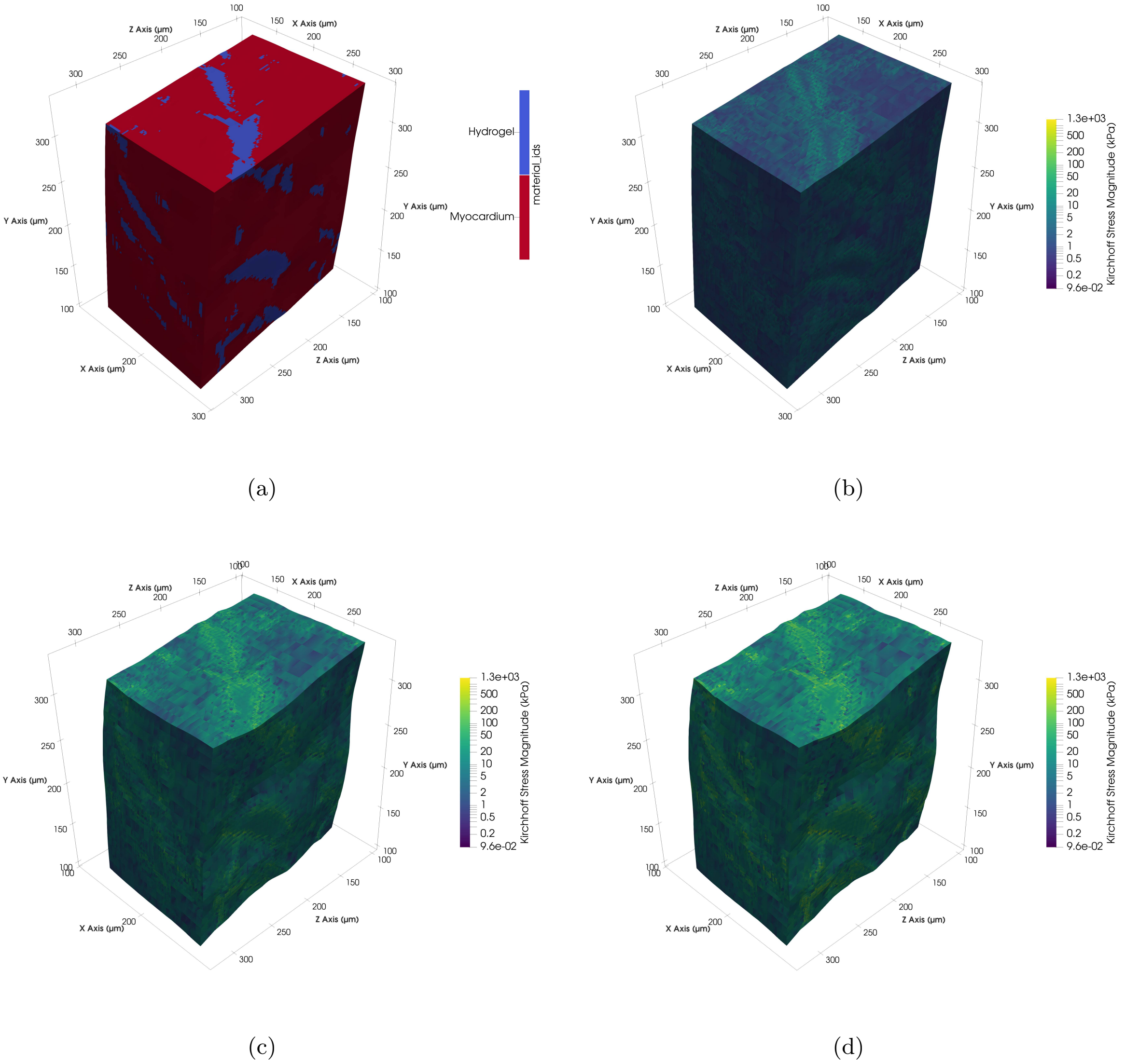

(a)

(b)

(c)

(d)

Figure 3.28: Visualisations, for Cluster Centre 1, of a deformed central segment of the microstructural mesh, showing (a) the material types and the results for the (b) lower-bound ($E = 5$kPa), (c) median ($E = 50$kPa), and (d) upper-bound ($E = 100$kPa) hydrogel stiffness cases.

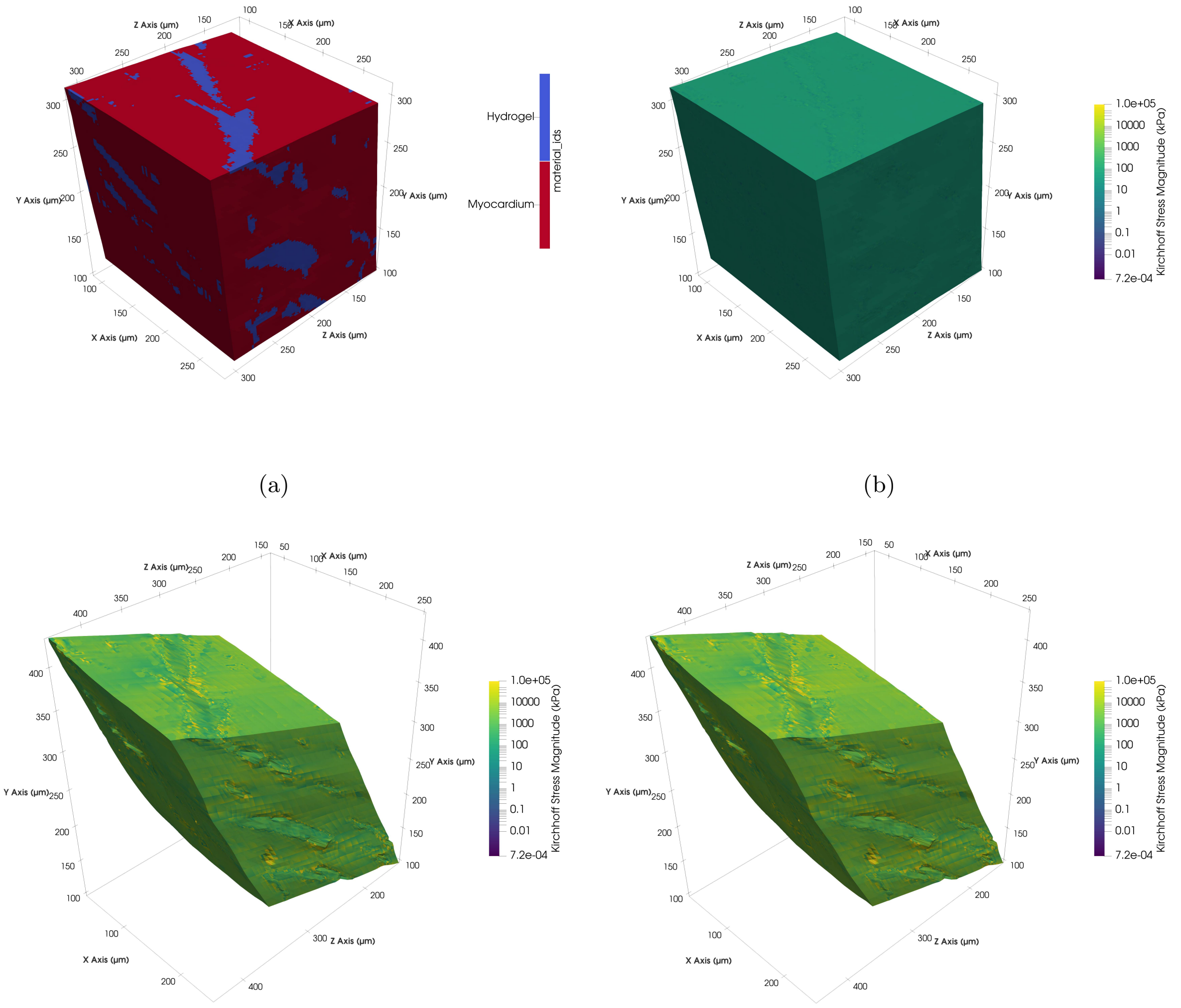

(a) (b)

(c) (d)

Figure 3.29: Visualisations, for Cluster Centre 2, of a deformed central segment of the microstructural mesh, showing (a) the material types and the results for the (b) lower-bound ($E = 5$kPa), (c) median ($E = 50$kPa), and (d) upper-bound ($E = 100$kPa) hydrogel stiffness cases.

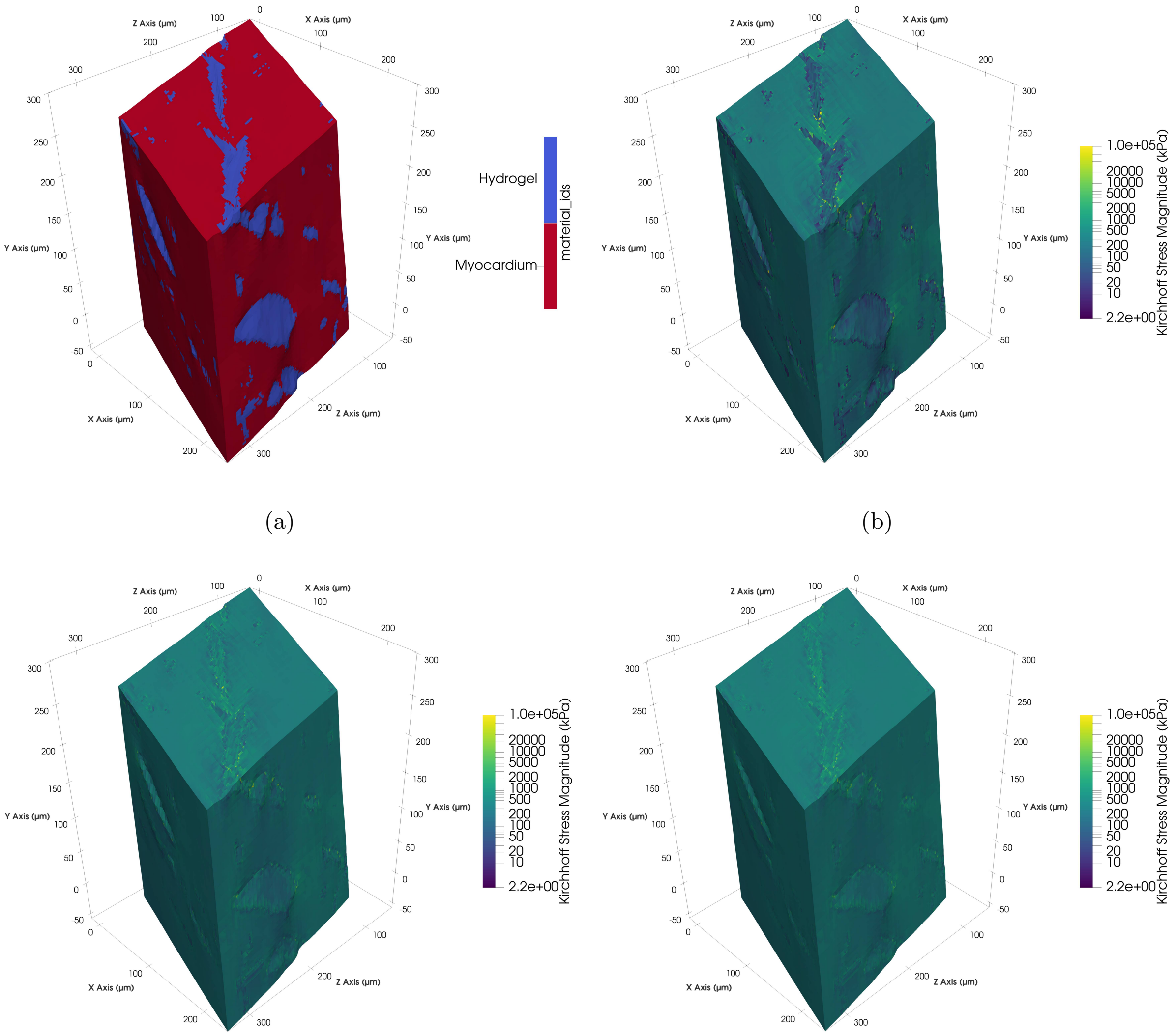

(a)

(b)

(c)

(d)

Figure 3.30: Visualisations, for Cluster Centre 3, of a deformed central segment of the microstructural mesh, showing (a) the material types and the results for the (b) lower-bound ($E = 5$kPa), (c) median ($E = 50$kPa), and (d) upper-bound ($E = 100$kPa) hydrogel stiffness cases.

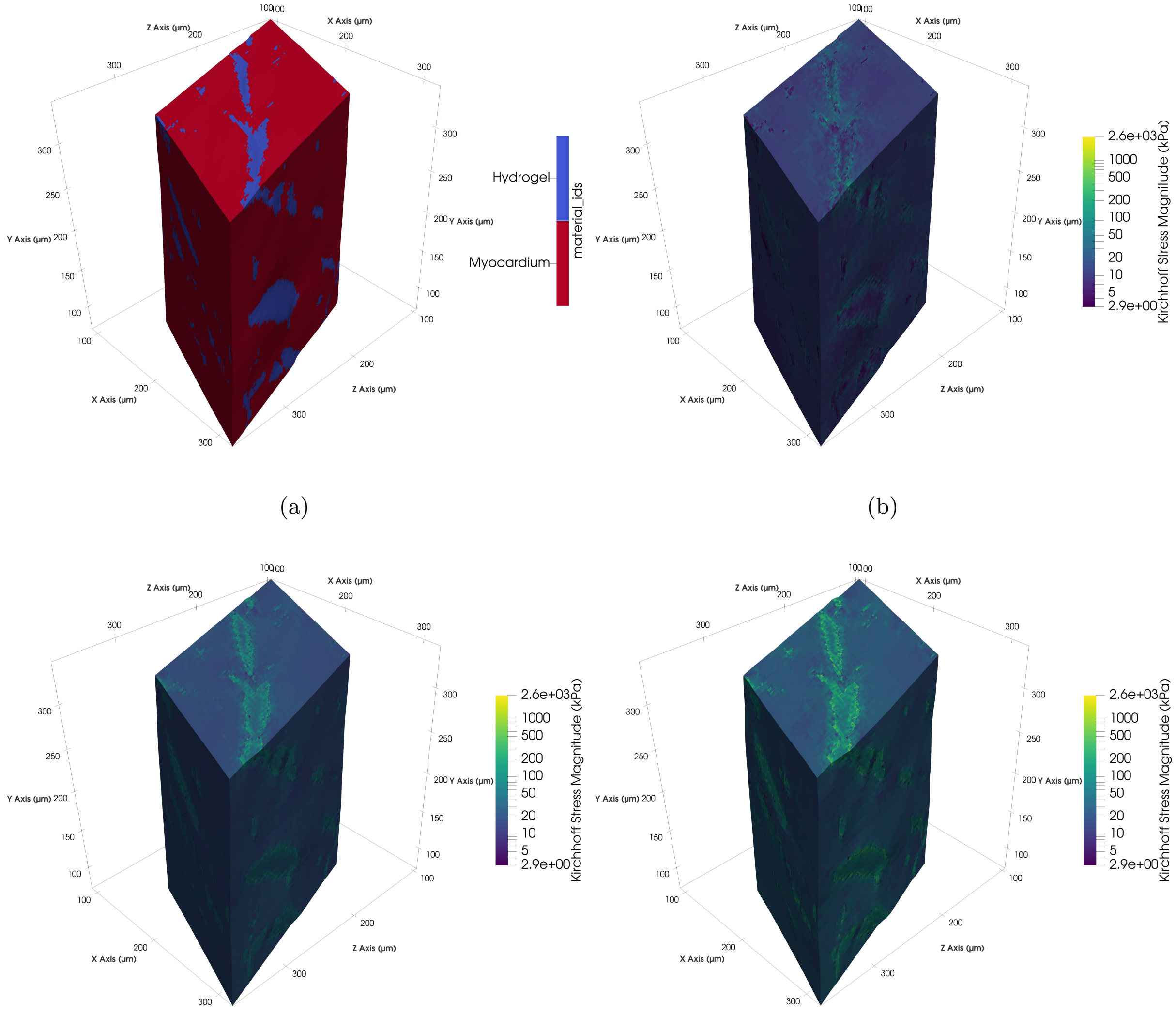

(a) (b)

(c) (d)

Figure 3.31: Visualisations, for Cluster Centre 4, of a deformed central segment of the microstructural mesh, showing (a) the material types and the results for the (b) lower-bound ($E = 5$kPa), (c) median ($E = 50$kPa), and (d) upper-bound ($E = 100$kPa) hydrogel stiffness cases.

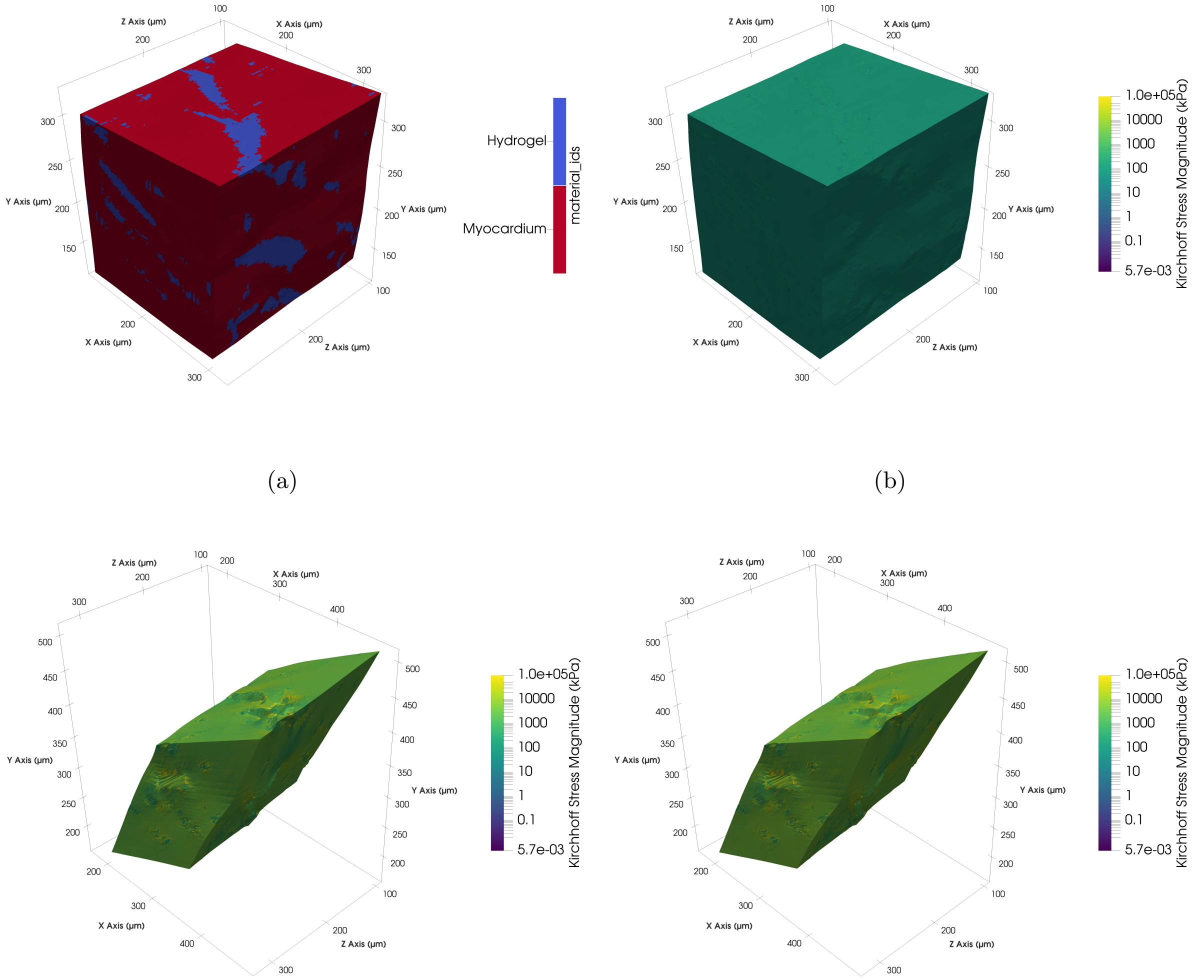

(a) (b)

(c) (d)

Figure 3.32: Visualisations, for Cluster Centre 5, of a deformed central segment of the microstructural mesh, showing (a) the material types and the results for the (b) lower-bound ($E = 5\text{kPa}$), (c) median ($E = 50\text{kPa}$), and (d) upper-bound ($E = 100\text{kPa}$) hydrogel stiffness cases.

Chapter 4

Discussion

This study aimed to develop a computational framework for use in investigating the microstructural mechanical response of myocardium with hydrogel biomaterial injectate inclusions, when subjected to the actions of the cardiac cycle. The hydrogel injectate was assumed to behave as an elastic solid, although in reality it exhibits both solid-like and fluid-like behaviour. The validity of this assumption was evaluated through a set of computational case studies, and the framework was developed in such a way as to allow for extension into models such as viscoelasticity and poroelasticity.

A finite-element geometry of the microstructure of rat myocardium with hydrogel biomaterial inclusions, was developed using confocal microscopy imaging data. Using the open-source C++ finite-element library deal.II, a finite-element solver was developed, capable of solving problems using multiple hyperelastic material models, and of applying boundary conditions derived from macroscale *in silico* cardiac strain data. The behaviour of the hydrogel injectate was modelled using an isotropic, Neo-Hookean hyperelastic model, while the behaviour of the myocardium was modelled using a variation of the anisotropic hyperelastic model developed by Holzapfel et al. (2009). Logarithmic strain data were extracted from an existing macroscale ABAQUS model of rat myocardium, and used to develop a set of five boundary conditions which were then applied to the microstructural geometry. To demonstrate the capacity of the developed program, case studies were conducted using the set of boundary conditions and a range of hydrogel stiffness parameters.

The following sections discuss the aspects of the geometry and program developed in this study, as well as the results of the case studies.

4.1 Geometry development

As part of the present study, a detailed microstructural mesh, shown in Figure 3.4 was reconstructed from high-resolution confocal microscopy data made available from Sands et al. (2005). The available dataset, as seen in Figure 2.3 consisted of 2D image slices of a myocardial tissue block, extracted from the left ventricular wall of a rat specimen. In this study, a region-growing image processing algorithm was developed and implemented to segment the original image dataset into two regions representing myocardium and interstitial cavities. It was then presumed that, following an injection of hydrogel biomaterial, the interstitial regions would be filled with hydrogel injectate. Under this assumption, the segmented image data was used to generate a deal.II triangulation (mesh) object, wherein myocardium and hydrogel regions could be identified and described by distinct constitutive models. This was accomplished through the binarisation of the segmented image data, followed by the use of the mesh generation capabilities of the deal.II library. Although the present study makes use of two material domains, and therefore at most two constitutive models, the developed program is capable of handling any number of material domains and corresponding constitutive models. The resulting geometry is a high-resolution representation of the information contained in the original confocal microscopy dataset, where each cell of the geometry corresponds to a pixel from the original dataset. Due to computational resource limitations, the geometry used in this study represents a subset of the original image dataset, however the method that was developed can be used to reconstruct finite-element meshes from 3D image datasets of any size.

The reconstructed geometry used in this study does not necessitate idealisations of myocardial tissue structure or hydrogel injectate distribution. In contrast, numerous previous macroscale models have made use of such idealisations to reduce computational expense, such as (Kichula et al. 2014; Wenk et al. 2009; H. Wang et al. 2017; Lee et al. 2014) as per Sack et al. (2016). In a microstructural setting, Sirry et al. (2013) generated finite-element geometries with detailed hydrogel injectate distributions, using cardiac MRI data obtained from rat specimens following an injection of hydrogel biomaterial, although these geometries were not used for any computational studies in the original paper.

4.2 Finite-element solver development

The finite-element solver developed in this study allows for the implementation of hyperelastic material models defined by a strain energy function, provided that expressions for the Kirchhoff stress tensor and spatial elasticity tensor can be derived in terms of the deformation gradient. Both isotropic and anisotropic material models have been implemented, and the solver allows for the use of compressible or isochoric-volumetric split model variations. These capabilities are demonstrated in the case studies conducted in this study. In a manner similar to Wise et al. (2016), an isotropic Neo-Hookean model was used to describe the behaviour of the hydrogel injectate; and a variation of the anisotropic model developed by (Holzapfel et al. 2009) was used to describe the behaviour of the myocardium. The latter of these two models has been used extensively in literature to describe the behaviour of passive myocardium, as per (Sack et al. 2016). The fact that the solver was developed using deal.II provides a basis for extension into more advanced models aiming to more accurately describe the behaviour of hydrogel. Feng et al. (2020) implemented a poroelastic model using deal.II, and their model could be implemented in the developed solver, although doing so fell outside the scope of the present study. Comellas et al. (2020) implemented a viscoelastic model using deal.II, however implementing this model also fell outside the scope of the present study.

Furthermore, the solver is able to output homogenised metrics, such as the homogenised first Piola-Kirchhoff stress and the homogenised deformation gradient. The solver is also capable of applying thermodynamically-admissible boundary conditions, in the form of kinematic uniform boundary conditions, to a microstructure. These functions provide a means to analyse the macroscale mechanical response, of myocardium with hydrogel injectate inclusions, based on microscale simulations; however conducting an in-depth investigation of this sort fell outside the scope of the present study.

4.3 Application of developed framework

4.3.1 Boundary conditions

The present study developed a method for applying boundary conditions derived from macroscopic ABAQUS models of myocardium, to a microstructurally representative geometry. Logarithmic strain data, over three cardiac cycles, were extracted from an existing macroscale biventricular ABAQUS model of rat myocardium. The logarithmic strain dataset was then processed, using the the method described in Section 2.3.1, to produce kinematically uniform boundary conditions which satisfied the Hill-Mandel Principle, and were able to be applied to the microstructural geometry. The developed program is capable of applying a single target strain state, as demonstrated in case study 2, and of applying a time-dependent set of strain states (representing a loading path), as demonstrated in case study 1. The ability to replicate time-dependent loading paths using the microstructural geometry further indicates that the program could be extended to models beyond hyperelasticity that are loading-path dependent, such as viscoelasticity and poroelasticity.

4.3.2 Case studies

To facilitate the demonstration of the capabilities of the finite-element program developed in this study, a series of computational case studies were conducted. The first case study was conducted on an idealised microstructural mesh, representing a myocardial tissue block with a cylindrical hydrogel injectate inclusion, and the second case study was conducted on a realistic microstructural mesh which was reconstructed from confocal microscopic medical imaging data. While these case studies were not intended for biological analysis, they validate the program's ability to simulate the mechanical response of microstructural geometries under boundary conditions derived from the results of macroscale cardiac *in* *silico* models.

Idealised mesh

The case study using the idealised mesh demonstrated that the developed computational tool is capable of producing homogenised and quadrature point-specific results when time-dependent boundary conditions have been applied. The agreement between the applied kinematic uniform boundary conditions and the homogenised deformation gradient indicates that the solver correctly implements boundary constraints for the cases where only an isotropic hyperelastic material model has been used, as well as when an anisotropic hyperelastic model is introduced for the myocardium. The stress distributions obtained at the quadrature points further indicate that the tool can resolve local stress variations within the material domains. It was observed that the magnitudes of the resulting stresses increased significantly when an anisotropic hyperelastic model was introduced for the myocardium, and furthermore, that the peak stress magnitudes occurred on the boundary regions between the myocardium and the hydrogel injectate. This difference in the magnitudes of the observed stresses can likely be attributed to the fact that the anisotropic model given by Equations (2.2.45) and (2.2.46) includes exponential terms, whereas the isotropic, Neo-Hookean model given by Equations (2.2.38) and (2.2.39) does not.

Realistic mesh

The case study using the realistic microstructural mesh further demonstrated the program's ability to handle complex geometries and material heterogeneity. The reconstructed geometry, based on confocal microscopy data, allowed for the differentiation of myocardium and hydrogel regions, and the applied strain states resulted in stress distributions which could be extracted for each material domain. The results confirm that the program can accommodate multiple material domains and isotropic as well as anisotropic constitutive models. Importantly, the results indicate that under more strenuous loading conditions during the cardiac cycle, the program is unable to completely resolve the solution to match the applied target strain state, and produces stress magnitudes which far exceed reasonable elastic material limits. This can be seen in Figures 3.20b and 3.20e, indicating that under certain loading conditions, the assumption of elastic material behaviour is not sufficient, as there are areas where the stress exceeds any reasonable elastic limits. This outcome supports the need to extend the developed program beyond hyperelastic material models, which assume that the hydrogel behaves in a completely solid-like way. In Figures 3.22 to 3.26 and 3.28 to 3.32 it was observed that the excessive stress magnitudes tended to occur on the boundary regions between the myocardium and hydrogel domains. Figure 3.20c indicates that, under certain loading conditions, increasing the hydrogel stiffness led to increases in the overall stresses in the hydrogel and myocardium regions, but a reduction in the maximum stresses observed in both the hydrogel and myocardium. This outcome aligns with the findings of H. Wang et al. (2017), in which increases in the stiffness parameters for the hydrogel injectate led to greater reductions in the observed myocardial stresses.

Furthermore, the simulations conducted on the realistic microstructural mesh revealed the potential disadvantages of geometric idealisations of the distribution of hydrogel injectate. The stress distributions seen in Figures 3.22 to 3.26 and 3.28 to 3.32 were strongly linked to the distribution pattern of the hydrogel injectate, with significant stress concentrations occurring on the boundary regions of the hydrogel domain. When compared to the stress distributions seen in Figure 3.16, it can be seen that idealisations of the distribution of hydrogel injectate lead to similarly idealised stress distributions, which may potentially limit the accuracy of predictions regarding mechanical interactions between the hydrogel and the surrounding tissue.

4.4 Overall remarks

The framework presented in this study provides a platform for conducting microstructural modelling investigations into the mechanical response of myocardium following an injection of hydrogel biomaterial. Importantly, the presented framework reduced the need for geometric idealisations of the cardiac microstructure and the distribution of hydrogel injectate. In the present study, the assumption was made that both the myocardium and the hydrogel injectate behave as elastic solids, and the validity of this assumption was evaluated by applying boundary conditions derived from a macroscale finite-element model of rat myocardium. The framework was developed in an extensible manner using deal.II, so that more advanced descriptions of material behaviour, including models such as poroelasticity which make use of multiple governing equations, could be implemented. It was found that, in more strenuous cardiac loading cases, the observed stresses in the microstructure were excessive, and that in these cases the assumption of elastic material behaviour was insufficient. This provides a justification for extending the model beyond hyperelasticity to more advanced models such as viscoelasticity and poroelasticity. Both viscoelasticity and poroelasticity have been implemented in deal.II, by Comellas et al. (2020) and Feng et al. (2020), respectively; although their work was not conducted in the current context of myocardial interactions with hydrogel injectate. These models are able to describe material behaviour which is history-dependent, and in preparation for these extensions, the ability of the developed solver to implement time-dependent boundary conditions was demonstrated in Section 3.2.2 - "Case study 1 - Idealised geometry with time-dependent KUBCs applied". If such extensions are implemented, and the resulting *in silico* outcomes have been shown to be in line with observed experimental results, the framework will be able to provide more reliable predictions regarding the mechanical interaction of myocardium and hydrogel injectate.

The framework benefits the state of the art of current computational modelling of hydrogel injectate therapies by providing a basis for microstructural modelling investigations which: do not necessitate idealisations of the myocardial structure or the distribution of hydrogel injectate, make use of thermodynamically-admissible boundary conditions which can be derived from macroscale cardiac models, and describe the behaviour of the myocardium and hydrogel injectate with varying levels of complexity. As an example, Sirry et al. (2013) developed a highly realistic geometry of the structure of myocardium and the distribution of hydrogel injectate, using MRI imaging data; however they did not conduct any computational investigations using this geometry, a limitation which could be addressed using the developed framework. A further example is provided by Ngoepe et al. (2019), which investigated the flow of PEG hydrogel in a cardiac microstructure. Their study also made use of a highly realistic geometry, derived from confocal microscopy imaging data, and the hydrogel injectate was idealised to behave as a non-Newtonian fluid. The framework presented in this study, provided it is extended beyond hyperelasticity, would benefit such studies by allowing for more realistic descriptions of the behaviour of hydrogel injectate.

One potential use of an extended version of the developed framework is in optimising the material parameters of hydrogel injectate, to improve its mechanical compatibility with myocardium. An example of such an investigation is seen in H. Wang et al. (2017), where increasing the stiffness of the hydrogel was shown to reduce the observed stresses in the myocardium. However, their study was conducted using a macroscale FE model, and idealised the distribution of hydrogel injectate using ellipsoidal inclusions. The framework presented in this study provides the basis for similar investigations, using a microstructural modelling approach, and with a reduced need for geometric idealisations. Such investigations would be conducted with the ultimate aim of informing future designs of hydrogel injectate therapies, and improving the efficacy of these therapies as a treatment modality for myocardial infarction.

Chapter 5

Conclusion

This study aimed to develop a computational framework capable of investigating the mechanical response of a myocardial tissue block with hydrogel injectate inclusions, and to demonstrate the simulation capabilities of the framework using various material model combinations and boundary condition applications. To achieve these aims, the following objectives were defined:

1. To develop a representative microstructural geometry comprised of myocardium and hydrogel injectate.
2. To implement isotropic and anisotropic hyperelastic material models, which allow for the variation of material parameters.
3. To develop appropriate boundary conditions which can be used to replicate the actions of the cardiac cycle.
4. To demonstrate the capabilities of the developed framework using a range of input conditions.

All objectives were achieved, and the outcomes have been presented in the previous chapter. The following section summarises the methods and models developed in this study, and presents recommendations for future work based on their limitations.

5.1 Geometry development (objective 1)

A 3D microstructural finite-element mesh was reconstructed from *ex vivo* confocal microscopy imaging data of a rat myocardial tissue block, using a region-growing image segmentation algorithm. The developed geometry included a realistic representation of the myocardial structure, including the structure of the interstitial cavities and laminar sheets. This approach enabled the differentiation of the geometry into myocardial tissue regions and cavity regions, the latter of which was assumed to be occupied with hydrogel injectate. This study made use of a subset of the complete confocal microscopy image dataset, however the developed method for geometry reconstruction can be scaled to larger medical imaging datasets.

These findings fulfilled objective 1 of the study.

Limitations

To ensure the case studies presented in this study were computationally feasible, a finite-element geometry with dimensions of 0.386 mm in the radial, longitudinal, and circumferential dimensions was used. This represents a subset of the full image dataset, which has dimensions of 4.25 mm, 1.12 mm, and 0.88 mm in the radial, longitudinal, and circumferential directions respectively. For similar computational feasibility reasons, the present study did not make use of an adaptively refined mesh, and instead utilised a one-to-one ratio in assigning each image voxel to a cell in the geometry. Additionally, a single set of anisotropic fibre directions was used for the microstructural geometry, which is a simplification. In reality, the fibre directions likely vary throughout the microstructure.

Recommendations

Increasing the overall dimensions of the finite-element geometry would be recommended, to include more details of the cardiac microstructure. This would allow for an investigation into the minimum mesh size required to constitute an RVE, which could be done by iteratively expanding the size of the mesh, and observing the changes in the homogenised response. Furthermore, the use of adaptive mesh refinement techniques would improve the predictive capacity of the developed computational tool, especially in regions that exhibit high stress concentration behaviour, such as the borders between myocardial tissue and interstitial cavities. Additionally, the models could be made more accurate through the use of a more advanced description of the variation of fibre directions within the cardiac microstructure.

5.2 Constitutive models (objective 2)

The developed finite-element program supports hyperelastic material models derived from strain energy functions, accommodating both isotropic and anisotropic behaviour. Isochoric-volumetric split formulations were used for both myocardium and hydrogel injectate, demonstrating the program's ability to implement these constitutive models. The modular code development structure of the program also allows for the inclusion of additional hyperelastic material models, extending the applicability of the framework.

These findings fulfilled objective 2 of the study.

Limitations

In its present state, the program only allows for the definition of compressible and isochoric-volumetric split hyperelastic material models. Furthermore, the material behaviour of the myocardium was described using a constitutive model developed for passive myocardium, as opposed to including a description of the active, contractile behaviour. Additionally, in the presented case studies, a single set of material parameters was used to describe the myocardium, and three sets of material parameters were used to describe the behaviour of the hydrogel injectate. This simplification may not fully capture the variability of myocardial tissue or hydrogel properties.

Recommendations

To allow for the implementation of a broader range of material models, it is recommended that the program be extended to incorporate fully incompressible material models. This would remove the need for explicit descriptions of the volumetric strain energy terms, and instead rely on a mixed displacement-pressure finite element formulation. Further investigation into a broader range of possible myocardial and hydrogel material parameter combinations is also recommended. It is further recommended that the behaviour of the myocardium be separated into active and passive components, allowing each component to be described by a separate constitutive law. Additionally, the program can be extended to allow for loading-path dependent models, such as viscoelasticity and poroelasticity, to more realistically describe the behaviour of the hydrogel injectate. The fact that the program was developed in deal.II facilitates these extensions in certain cases. For example, in the case of viscoelasticity and poroelasticity, studies have already implemented these models using deal.II, although this was not done in a cardiovascular modelling context.

5.3 Boundary conditions (objective 3)

A method was developed to apply boundary conditions derived from macroscale ABAQUS models to the microstructural geometry. By processing logarithmic strain data from a biventricular model, kinematically uniform boundary conditions were generated in a manner consistent with the Hill-Mandel Principle. The capability of the program in applying both single strain-states and time-dependant loading paths was demonstrated, using a set of five kinematic uniform boundary conditions.

These findings fulfilled objective 3 of the study.

Limitations

To ensure the computational feasibility of the case studies, a limited subset of five kinematically uniform boundary conditions were used to demonstrate the program's capabilities. These boundary conditions were derived from a larger set of 2 180 104 possible boundary conditions, each corresponding to a quadrature point in the original macroscale model. Furthermore, only peak cardiac strain magnitudes were applied to the microstructural cardiac geometry, as opposed to the full dataset which spans over three cardiac cycles. These simplifications reduced computational expense, but may not fully capture the range of possible macroscale loading conditions.

Recommendations

It is recommended that future work should incorporate of a greater number of boundary conditions to improve the predictive capacity of the microstructural simulations. New methodologies for selecting representative sample spaces from macroscale model data, such as those developed by Benaimeche et al. (2022) and Chaouch et al. (2024) may provide an improved methodology for investigating a more complete range of possible macroscale cardiac loading conditions.

5.4 Demonstration of the capacity of the developed computational tool (objective 4)

The results of the case studies demonstrate that the developed computational tool is capable of solving finite element problems involving complex microstructural geometries, multiple material domains, and both isotropic and anisotropic constitutive models. The program successfully applied both time-dependent and single-state kinematic uniform boundary conditions derived from macroscale strain data and produced homogenised and quadrature point-specific stress distributions, demonstrating its functionality in simulating microstructural mechanical behaviour.

These findings fulfilled objective 4 of the study.

Limitations

While the program effectively captured the response of the microstructural geometry under various loading conditions, certain cases revealed an inability to fully resolve the target strain states. In some instances, the computed stress magnitudes exceeded reasonable elastic material limits, suggesting that the exclusive use of hyperelastic models may be insufficient to represent the true mechanical response of the myocardium-hydrogel system. Additionally, computational resource constraints limited the size of the reconstructed geometry, as well as the ability to apply time-dependent loading conditions to the realistic microstructural geometry

Recommendations

It is strongly recommended that descriptions of material behaviour beyond hyperelasticity be investigated in future work. These include models which incorporate time- and rate-dependent material responses, such as viscoelasticity and poroelasticity. Such models may allow for the capturing of the potential viscous behaviour of the hydrogel injectate, which is relevant when the stresses in the hydrogel exceed the expected elastic limits of the material. It is further recommended that future work makes use of more expansive computational resources, to allow for the investigation of larger microstructural volumes and boundary conditions which replicate the actions of the cardiac cycle across larger ranges in time. Moreover, the use of distributed memory parallelisation using the Message Passing Interface (MPI), would be an improvement over the currently implemented shared memory parallelisation. The use of MPI would lead to major improvements in scalability of the framework, by allowing more expansive sets of computational resources, such as high-performance computing clusters, to be leveraged.

5.5 Final remarks

In conclusion, the present study developed a framework for conducting microstructural modelling investigations into the mechanical response of myocardium with hydrogel injectate inclusions. Key aspects included the construction of a finite-element mesh from high-resolution confocal microscopy imaging data, the extraction of boundary conditions from a macroscale model of rat myocardium, and the development of a finite-element solver. The myocardium and hydrogel injectate were assumed to behave as elastic solids, and it was shown that, under certain loading conditions, this assumption was insufficient, and that an extension to more advanced models describing material behaviour is justified. The framework was developed in deal.II to facilitate these extensions into, for example, history-dependent models such as viscoelasticity and poroelasticity, which have been implemented using deal.II in existing literature.

The framework presented in this study provides an extendable basis for microscale *in silico* investigations of the effects of hydrogel injectate therapies for MI; with: a reduced need for geometric idealisations, methods for determining appropriate thermodynamically-admissible boundary conditions, and functionality through which both homogenised (macroscale) and microscale mechanical responses can be observed. Ultimately, this framework paves the way for more accurate microscale predictions of hydrogel injectate behaviour in cardiac tissue, which can be used to inform the development of more effective hydrogel injectate therapies for myocardial infarction.

Bibliography

Africa, Pasquale C., Daniel Arndt, Wolfgang Bangerth, Bruno Blais, Marc Fehling, Rene Gassmöller, Timo Heister, Luca Heltai, Sebastian Kinnewig, Martin Kronbichler, Matthias Maier, Peter Munch, Magdalena Schreter-Fleischhacker, Jan P. Thiele, Bruno Turcksin, David Wells, and Vladimir Yushutin (2024). "The deal.II library, Version 9.6". In: *Journal of Numerical Mathematics* 32.4, pp. 369–380. DOI: `10.1515/jnma-2024-0137`. URL: `https://dealii.org`.

Alheit, Benjamin (2022). "Multiscale modelling of sutures in a high-performing biological protective structure: the turtle shell". University of Cape Town. URL: `http://hdl.handle.net/11427/36670`.

Alzahrani, Yahya and Boubakeur Boufama (2021). "Biomedical Image Segmentation: A Survey". In: *SN Computer Science* 2.4. ISSN: 2662-995X. DOI: `10.1007/s42979-021-00704-7`. URL: `https://doi.org/10.1007/s42979-021-00704-7`.

Annibali, G., I. Scrocca, T. C. Aranzulla, E. Meliga, F. Maiellaro, and G. Musumeci (2022). """No-Reflow" Phenomenon: A Contemporary Review". In: *J Clin Med* 11.8. ISSN: 2077-0383 (Print) 2077-0383 (Electronic) 2077-0383 (Linking). DOI: `10.3390/jcm11082233`. URL: `https://www.ncbi.nlm.nih.gov/pubmed/35456326`.

Arndt, Daniel, Wolfgang Bangerth, Denis Davydov, Timo Heister, Luca Heltai, Martin Kronbichler, Matthias Maier, Jean-Paul Pelteret, Bruno Turcksin, and David Wells (2021). "The deal.II finite element library: Design, features, and insights". In: *Computers & Mathematics with Applications* 81, pp. 407–422. ISSN: 0898-1221. DOI: `10.1016/j.camwa.2020.02.022`. URL: `https://arxiv.org/abs/1910.13247`.

Arts, T., R. S. Reneman, and P. C. Veenstra (1979). "A model of the mechanics of the left ventricle". In: *Ann Biomed Eng* 7.3-4, pp. 299–318. ISSN: 0090-6964 (Print) 0090-6964 (Linking). DOI: `10.1007/BF02364118`. URL: `https://www.ncbi.nlm.nih.gov/pubmed/547767`.

Ashammakhi, N., S. Ahadian, M. A. Darabi, M. El Tahchi, J. Lee, K. Suthiwanich, A. Sheikhi, M. R. Dokmeci, R. Oklu, and A. Khademhosseini (2019). "Minimally Invasive and Regenerative Therapeutics". In: *Adv Mater* 31.1, e1804041. ISSN: 1521-4095 (Electronic) 0935-9648 (Print) 0935-9648 (Linking). DOI: `10.1002/adma.201804041`. URL: `https://www.ncbi.nlm.nih.gov/pubmed/30565732`.

Asti, Annalia and Luciana Gioglio (2014). "Natural and Synthetic Biodegradable Polymers: Different Scaffolds for Cell Expansion and Tissue Formation". In: *The International Journal of Artificial Organs* 37.3, pp. 187–205. ISSN: 0391-3988 1724-6040. DOI: `10.5301/ijao.5000307`.

Baillargeon, B., N. Rebelo, D. D. Fox, R. L. Taylor, and E. Kuhl (2014). "The Living Heart Project: A robust and integrative simulator for human heart function". In: *Eur J Mech A Solids* 48, pp. 38–47. ISSN: 0997-7538 (Print) 1873-7285 (Electronic) 0997-7538 (Linking). DOI: `10.1016/j.euromechsol.2014.04.001`. URL: `https://www.ncbi.nlm.nih.gov/pubmed/25267880`.

Bastings, M. M., S. Koudstaal, R. E. Kieltyka, Y. Nakano, A. C. Pape, D. A. Feyen, F. J. van Slochteren, P. A. Doevendans, J. P. Sluijter, E. W. Meijer, S. A. Chamuleau, and P. Y. Dankers (2014). "A fast pH-switchable and self-healing supramolecular hydrogel carrier for guided, local catheter injection in the infarcted myocardium". In: *Adv Healthc Mater* 3.1, pp. 70–8. ISSN: 2192-2659 (Electronic) 2192-2640 (Linking). DOI: `10.1002/adhm.201300076`. URL: `https://www.ncbi.nlm.nih.gov/pubmed/23788397`.

Benaimeche, Mohamed Amine, Julien Yvonnet, Benoit Bary, and Qi-Chang He (2022). "A k-means clustering machine learning-based multiscale method for anelastic heterogeneous structures with internal variables". In: *International Journal for Numerical Methods in Engineering* 123.9, pp. 2012–2041. DOI: `https://doi.org/10.1002/nme.6925`. eprint: `https://onlinelibrary.wiley.com/doi/pdf/10.1002/nme.6925`. URL: `https://onlinelibrary.wiley.com/doi/abs/10.1002/nme.6925`.

Blankstein, R. (2012). "Cardiology patient page. Introduction to noninvasive cardiac imaging". In: *Circulation* 125.3, e267–71. ISSN: 1524-4539 (Electronic) 0009-7322 (Linking). DOI: `10.1161/CIRCULATIONAHA.110.017665`. URL: `https://www.ncbi.nlm.nih.gov/pubmed/22271850`.

Bonet, Javier and Richard D. Wood (2008). *Nonlinear continuum mechanics for finite element analysis.* 2nd ed. Cambridge University Press.

Bradski, Gary (2000). “The OpenCV library.” In: *Dr. Dobb’s Journal: Software Tools for the Professional Programmer* 25.11, pp. 120–123. URL: `https://opencv.org`.

Braunwald, E. (2012). “The treatment of acute myocardial infarction: the Past, the Present, and the Future”. In: *Eur Heart J Acute Cardiovasc Care* 1.1, pp. 9–12. ISSN: 2048-8726 (Print) 2048-8734 (Electronic) 2048-8726 (Linking). DOI: `10.1177/2048872612438026`. URL: `https://www.ncbi.nlm.nih.gov/pubmed/24062883`.

Celermajer, D. S., C. K. Chow, E. Marijon, N. M. Anstey, and K. S. Woo (2012). “Cardiovascular disease in the developing world: prevalences, patterns, and the potential of early disease detection”. In: *J Am Coll Cardiol* 60.14, pp. 1207–16. ISSN: 1558-3597 (Electronic) 0735-1097 (Linking). DOI: `10.1016/j.jacc.2012.03.074`. URL: `https://www.ncbi.nlm.nih.gov/pubmed/22858388`.

Chaouch, Souhail and Julien Yvonnet (2024). “An unsupervised machine learning approach to reduce nonlinear FE2 multiscale calculations using macro clustering”. In: *Finite Elements in Analysis and Design* 229, p. 104069. ISSN: 0168-874X. DOI: `https://doi.org/10.1016/j.finel.2023.104069`. URL: `https://www.sciencedirect.com/science/article/pii/S0168874X23001622`.

Christman, K. L., H. H. Fok, R. E. Sievers, Q. Fang, and R. J. Lee (2004). “Fibrin glue alone and skeletal myoblasts in a fibrin scaffold preserve cardiac function after myocardial infarction”. In: *Tissue Eng* 10.3-4, pp. 403–9. ISSN: 1076-3279 (Print) 1076-3279 (Linking). DOI: `10.1089/107632704323061762`. URL: `https://www.ncbi.nlm.nih.gov/pubmed/15165457`.

Cleveland Clinic (2022). *Fibrinolytic (Thrombolytic) Therapy.* Accessed: 2024-06-30. URL: `https://my.clevelandclinic.org/health/treatments/22772-thrombolytic-fibrinolytic-therapy`.

Colquitt, Richard B., Douglas A. Colquhoun, and Robert H. Thiele (2011). “In silico modelling of physiologic systems”. In: *Best Practice & Research Clinical Anaesthesiology* 25.4, pp. 499–510. ISSN: 1521-6896. DOI: `10.1016/j.bpa.2011.08.006`. URL: `https://doi.org/10.1016/j.bpa.2011.08.006`.

Comellas, Ester, Silvia Budday, Jean-Paul Pelteret, Gerhard A. Holzapfel, and Paul Steinmann (2020). “Modeling the porous and viscous responses of human brain tissue behavior”. In: *Computer Methods in Applied Mechanics and Engineering* 369, p. 113128. ISSN: 0045-7825. DOI: `https://doi.org/10.1016/j.cma.2020.113128`. URL: `https://www.sciencedirect.com/science/article/pii/S0045782520303133`.

Dai, W., L. E. Wold, J. S. Dow, and R. A. Kloner (2005). “Thickening of the infarcted wall by collagen injection improves left ventricular function in rats: a novel approach to preserve cardiac function after myocardial infarction”. In: *J Am Coll Cardiol* 46.4, pp. 714–9. ISSN: 0735-1097 (Print) 0735-1097 (Linking). DOI: `10.1016/j.jacc.2005.04.056`. URL: `https://www.ncbi.nlm.nih.gov/pubmed/16098441`.

Deng, B., L. Shen, Y. Wu, Y. Shen, X. Ding, S. Lu, J. Jia, J. Qian, and J. Ge (2015). “Delivery of alginate-chitosan hydrogel promotes endogenous repair and preserves cardiac function in rats with myocardial infarction”. In: *J Biomed Mater Res A* 103.3, pp. 907–18. ISSN: 1552-4965 (Electronic) 1549-3296 (Linking). DOI: `10.1002/jbm.a.35232`. URL: `https://www.ncbi.nlm.nih.gov/pubmed/24827141`.

Do, A. V., B. Khorsand, S. M. Geary, and A. K. Salem (2015). “3D Printing of Scaffolds for Tissue Regeneration Applications”. In: *Adv Healthc Mater* 4.12, pp. 1742–62. ISSN: 2192-2659 (Electronic) 2192-2640 (Print) 2192-2640 (Linking). DOI: `10.1002/adhm.201500168`. URL: `https://www.ncbi.nlm.nih.gov/pubmed/26097108`.

Dobner, S., D. Bezuidenhout, P. Govender, P. Zilla, and N. Davies (2009). “A synthetic non-degradable polyethylene glycol hydrogel retards adverse post-infarct left ventricular remodeling”. In: *J Card Fail* 15.7, pp. 629–36. ISSN: 1532-8414 (Electronic) 1071-9164 (Linking). DOI: `10.1016/j.cardfail.2009.03.003`. URL: `https://www.ncbi.nlm.nih.gov/pubmed/19700140`.

Dokos, S., B. H. Smaill, A. A. Young, and I. J. LeGrice (2002). “Shear properties of passive ventricular myocardium”. In: *Am J Physiol Heart Circ Physiol* 283.6, H2650–9. ISSN: 0363-6135 (Print) 0363-6135 (Linking). DOI: `10.1152/ajpheart.00111.2002`. URL: `https://www.ncbi.nlm.nih.gov/pubmed/12427603`.

Dorsey, S. M., J. R. McGarvey, H. Wang, A. Nikou, L. Arama, K. J. Koomalsingh, N. Kondo, 3rd Gorman J. H., J. J. Pilla, R. C. Gorman, J. F. Wenk, and J. A. Burdick (2015). “MRI evaluation of injectable hyaluronic acid-based hydrogel therapy to limit ventricular remodeling after myocardial infarction”. In: *Biomaterials* 69, pp. 65–75. ISSN: 1878-5905 (Electronic) 0142-9612 (Print) 0142-9612 (Linking). DOI: `10.1016/j.biomaterials.2015.08.011`. URL: `https://www.ncbi.nlm.nih.gov/pubmed/26280951`.

Feng, James J. and Y.-N. Young (2020). “Boundary conditions at a gel-fluid interface”. In: *Phys. Rev. Fluids* 5 (12), p. 124304. DOI: `10.1103/PhysRevFluids.5.124304`. URL: `https://link.aps.org/doi/10.1103/PhysRevFluids.5.124304`.

Fomovsky, G. M. and J. W. Holmes (2010). “Evolution of scar structure, mechanics, and ventricular function after myocardial infarction in the rat”. In: *Am J Physiol Heart Circ Physiol* 298.1, H221–8. ISSN: 1522-1539 (Electronic) 0363-6135 (Print) 0363-6135 (Linking). DOI: `10.1152/ajpheart.00495.2009`. URL: `https://www.ncbi.nlm.nih.gov/pubmed/19897714`.

Frey, N., A. Linke, T. Suselbeck, J. Muller-Ehmsen, P. Vermeersch, D. Schoors, M. Rosenberg, F. Bea, S. Tuvia, and J. Leor (2014). “Intracoronary delivery of injectable bioabsorbable scaffold (IK-5001) to treat left ventricular remodeling after ST-elevation myocardial infarction: a first-in-man study”. In: *Circ Cardiovasc Interv* 7.6, pp. 806–12. ISSN: 1941-7632 (Electronic) 1941-7640 (Linking). DOI: `10.1161/CIRCINTERVENTIONS.114.001478`. URL: `https://www.ncbi.nlm.nih.gov/pubmed/25351198`.

Fu, Y., K. Xu, X. Zheng, A. J. Giacomin, A. W. Mix, and W. J. Kao (2012). “3D cell entrapment in crosslinked thiolated gelatin-poly(ethylene glycol) diacrylate hydrogels”. In: *Biomaterials* 33.1, pp. 48–58. ISSN: 1878-5905 (Electronic) 0142-9612 (Print) 0142-9612 (Linking). DOI: `10.1016/j.biomaterials.2011.09.031`. URL: `https://www.ncbi.nlm.nih.gov/pubmed/21955690`.

Fujimoto, K. L., Z. Ma, D. M. Nelson, R. Hashizume, J. Guan, K. Tobita, and W. R. Wagner (2009). “Synthesis, characterization and therapeutic efficacy of a biodegradable, thermoresponsive hydrogel designed for application in chronic infarcted myocardium”. In: *Biomaterials* 30.26, pp. 4357–68. ISSN: 1878-5905 (Electronic) 0142-9612 (Print) 0142-9612 (Linking). DOI: `10.1016/j.biomaterials.2009.04.055`. URL: `https://www.ncbi.nlm.nih.gov/pubmed/19487021`.

George, J. C., J. Goldberg, M. Joseph, N. Abdulhameed, J. Crist, H. Das, and V. J. Pompili (2008). “Transvenous intramyocardial cellular delivery increases retention in comparison to intracoronary delivery in a porcine model of acute myocardial infarction”. In: *J Interv Cardiol* 21.5, pp. 424–31. ISSN: 1540-8183 (Electronic) 0896-4327 (Print) 0896-4327 (Linking). DOI: `10.1111/j.1540-8183.2008.00390.x`. URL: `https://www.ncbi.nlm.nih.gov/pubmed/19012733`.

Göktepe, S., S. N. S. Acharya, J. Wong, and E. Kuhl (2010). “Computational modeling of passive myocardium”. In: *International Journal for Numerical Methods in Biomedical Engineering* 27.1, pp. 1–12. ISSN: 2040-7939 2040-7947. DOI: `10.1002/cnm.1402`.

Grover, G. N., N. Rao, and K. L. Christman (2014). “Myocardial matrix-polyethylene glycol hybrid hydrogels for tissue engineering”. In: *Nanotechnology* 25.1, p. 014011. ISSN: 1361-6528 (Electronic) 0957-4484 (Print) 0957-4484 (Linking). DOI: `10.1088/0957-4484/25/1/014011`. URL: `https://www.ncbi.nlm.nih.gov/pubmed/24334615`.

Guan, Debao, Faizan Ahmad, Peter Theobald, Shwe Soe, Xiaoyu Luo, and Hao Gao (2019). “On the AIC-based model reduction for the general Holzapfel–Ogden myocardial constitutive law”. In: *Biomechanics and Modeling in Mechanobiology* 18, pp. 1213–1232.

Guccione, Julius M., Ghassan S. Kassab, and Mark B. Ratcliffe (2010). *Computational Cardiovascular Mechanics*. ISBN: 978-1-4419-0730-1. DOI: `10.1007/978-1-4419-0730-1`.

Guccione, Julius M., L. K. Waldman, and A. D. McCulloch (1993). “Mechanics of active contraction in cardiac muscle: Part II–Cylindrical models of the systolic left ventricle”. In: *J Biomech Eng* 115.1, pp. 82–90. ISSN: 0148-0731 (Print) 0148-0731 (Linking). DOI: `10.1115/1.2895474`. URL: `https://www.ncbi.nlm.nih.gov/pubmed/8445902`.

Gurev, V., T. Lee, J. Constantino, H. Arevalo, and N. A. Trayanova (2011). “Models of cardiac electromechanics based on individual hearts imaging data: image-based electromechanical models of the heart”. In: *Biomech Model Mechanobiol* 10.3, pp. 295–306. ISSN: 1617-7940 (Electronic) 1617-7959 (Print) 1617-7940 (Linking). DOI: `10.1007/s10237-010-0235-5`. URL: `https://www.ncbi.nlm.nih.gov/pubmed/20589408`.

Haddad, S. M. H. and A. Samani (2018). “A finite element model of myocardial infarction using a composite material approach”. In: *Comput Methods Biomech Biomed Engin* 21.1, pp. 33–46. ISSN: 1476-8259 (Electronic) 1025-5842 (Linking). DOI: `10.1080/10255842.2017.1416355`. URL: `https://www.ncbi.nlm.nih.gov/pubmed/29252005`.

Hale, S. L., W. Dai, J. S. Dow, and R. A. Kloner (2008). “Mesenchymal stem cell administration at coronary artery reperfusion in the rat by two delivery routes: a quantitative assessment”. In: *Life Sci* 83.13-14, pp. 511–5. ISSN: 0024-3205 (Print) 0024-3205 (Linking). DOI: `10.1016/j.lfs.2008.07.020`. URL: `https://www.ncbi.nlm.nih.gov/pubmed/18755200`.

Hasan, A., A. Khattab, M. A. Islam, K. A. Hweij, J. Zeitouny, R. Waters, M. Sayegh, M. M. Hossain, and A. Paul (2015). “Injectable Hydrogels for Cardiac Tissue Repair after Myocardial Infarction”. In:

Adv Sci (Weinh) 2.11, p. 1500122. ISSN: 2198-3844 (Print) 2198-3844 (Electronic) 2198-3844 (Linking). DOI: `10.1002/advs.201500122`. URL: `https://www.ncbi.nlm.nih.gov/pubmed/27668147`.

Helm, P., M. F. Beg, M. I. Miller, and R. L. Winslow (2005). "Measuring and mapping cardiac fiber and laminar architecture using diffusion tensor MR imaging". In: *Ann N Y Acad Sci* 1047, pp. 296–307. ISSN: 0077-8923 (Print) 0077-8923 (Linking). DOI: `10.1196/annals.1341.026`. URL: `https://www.ncbi.nlm.nih.gov/pubmed/16093505`.

Henning, Robert J. (2012). "Stem Cells in Cardiac Repair – Recent Developments and Future Directions". In: *Interventional Cardiology Review* 7.1. ISSN: 1756-1477. DOI: `10.15420/icr.2012.7.1.10`.

– (2013). "Stem cells for cardiac repair: problems and possibilities". In: *Future Cardiol* 9.6, pp. 875–84. ISSN: 1744-8298 (Electronic) 1479-6678 (Linking). DOI: `10.2217/fca.13.78`. URL: `https://www.ncbi.nlm.nih.gov/pubmed/24180543`.

Holzapfel, G. A. and R. W. Ogden (2009). "Constitutive modelling of passive myocardium: a structurally based framework for material characterization". In: *Philos Trans A Math Phys Eng Sci* 367.1902, pp. 3445–75. ISSN: 1364-503X (Print) 1364-503X (Linking). DOI: `10.1098/rsta.2009.0091`. URL: `https://www.ncbi.nlm.nih.gov/pubmed/19657007`.

Hou, D., E. A. Youssef, T. J. Brinton, P. Zhang, P. Rogers, E. T. Price, A. C. Yeung, B. H. Johnstone, P. G. Yock, and K. L. March (2005). "Radiolabeled cell distribution after intramyocardial, intracoronary, and interstitial retrograde coronary venous delivery: implications for current clinical trials". In: *Circulation* 112.9 Suppl, pp. I150–6. ISSN: 1524-4539 (Electronic) 0009-7322 (Linking). DOI: `10.1161/CIRCULATIONAHA.104.526749`. URL: `https://www.ncbi.nlm.nih.gov/pubmed/16159808`.

Huang, K., E. W. Ozpinar, T. Su, J. Tang, D. Shen, L. Qiao, S. Hu, Z. Li, H. Liang, K. Mathews, V. Scharf, D. O. Freytes, and K. Cheng (2020). "An off-the-shelf artificial cardiac patch improves cardiac repair after myocardial infarction in rats and pigs". In: *Sci Transl Med* 12.538. ISSN: 1946-6242 (Electronic) 1946-6234 (Print) 1946-6234 (Linking). DOI: `10.1126/scitranslmed.aat9683`. URL: `https://www.ncbi.nlm.nih.gov/pubmed/32269164`.

Ifkovits, J. L., E. Tous, M. Minakawa, M. Morita, J. D. Robb, K. J. Koomalsingh, 3rd Gorman J. H., R. C. Gorman, and J. A. Burdick (2010). "Injectable hydrogel properties influence infarct expansion and extent of postinfarction left ventricular remodeling in an ovine model". In: *Proc Natl Acad Sci U S A* 107.25, pp. 11507–12. ISSN: 1091-6490 (Electronic) 0027-8424 (Print) 0027-8424 (Linking). DOI: `10.1073/pnas.1004097107`. URL: `https://www.ncbi.nlm.nih.gov/pubmed/20534527`.

Institute for Health Metrics and Evaluation (2024). *Global Burden of Disease 2021: Findings from the GBD 2021 Study*. URL: `https://www.healthdata.org/research-analysis/library/global-burden-disease-2021-findings-gbd-2021-study`.

Janz, R. F. and A. F. Grimm (1972). "Finite-element model for the mechanical behavior of the left ventricle. Prediction of deformation in the potassium-arrested rat heart". In: *Circ Res* 30.2, pp. 244–52. ISSN: 0009-7330 (Print) 0009-7330 (Linking). DOI: `10.1161/01.res.30.2.244`. URL: `https://www.ncbi.nlm.nih.gov/pubmed/5061321`.

Jardim, Sandra, João António, and Carlos Mora (2023). "Image thresholding approaches for medical image segmentation-short literature review". In: *Procedia Computer Science* 219, pp. 1485–1492.

Jasim, Wala'a and Rana Mohammed (2021). "A Survey on Segmentation Techniques for Image Processing". In: *Iraqi Journal for Electrical and Electronic Engineering* 17.2, pp. 73–93. ISSN: 2078-6069. DOI: `10.37917/ijeee.17.2.10`. URL: `https://doi.org/10.37917/ijeee.17.2.10`.

Jeon, O., J. E. Samorezov, and E. Alsberg (2014). "Single and dual crosslinked oxidized methacrylated alginate/PEG hydrogels for bioadhesive applications". In: *Acta Biomater* 10.1, pp. 47–55. ISSN: 1878-7568 (Electronic) 1742-7061 (Print) 1742-7061 (Linking). DOI: `10.1016/j.actbio.2013.09.004`. URL: `https://www.ncbi.nlm.nih.gov/pubmed/24035886`.

Jiang, X. J., T. Wang, X. Y. Li, D. Q. Wu, Z. B. Zheng, J. F. Zhang, J. L. Chen, B. Peng, H. Jiang, C. Huang, and X. Z. Zhang (2009). "Injection of a novel synthetic hydrogel preserves left ventricle function after myocardial infarction". In: *J Biomed Mater Res A* 90.2, pp. 472–7. ISSN: 1552-4965 (Electronic) 1549-3296 (Linking). DOI: `10.1002/jbm.a.32118`. URL: `https://www.ncbi.nlm.nih.gov/pubmed/18546187`.

John Hopkins Medicine (n.d.). *Coronary Artery Bypass Graft Surgery*. Accessed: 2024-06-30. URL: `https://www.hopkinsmedicine.org/health/treatment-tests-and-therapies/coronary-artery-bypass-graft-surgery`.

Johnson, T. D. and K. L. Christman (2013). "Injectable hydrogel therapies and their delivery strategies for treating myocardial infarction". In: *Expert Opin Drug Deliv* 10.1, pp. 59–72. ISSN: 1744-7593 (Electronic) 1742-5247 (Linking). DOI: `10.1517/17425247.2013.739156`. URL: `https://www.ncbi.nlm.nih.gov/pubmed/23140533`.

Kadner, K., S. Dobner, T. Franz, D. Bezuidenhout, M. S. Sirry, P. Zilla, and N. H. Davies (2012). "The beneficial effects of deferred delivery on the efficiency of hydrogel therapy post myocardial infarction". In: *Biomaterials* 33.7, pp. 2060–6. ISSN: 1878-5905 (Electronic) 0142-9612 (Linking). DOI: `10.1016/j.biomaterials.2011.11.031`. URL: `https://www.ncbi.nlm.nih.gov/pubmed/22153866`.

Kalogeris, T., C. P. Baines, M. Krenz, and R. J. Korthuis (2016). "Ischemia/Reperfusion". In: *Compr Physiol* 7.1, pp. 113–170. ISSN: 2040-4603 (Electronic) 2040-4603 (Linking). DOI: `10.1002/cphy.c160006`. URL: `https://www.ncbi.nlm.nih.gov/pubmed/28135002`.

Karimi, Alireza, Mahdi Navidbakhsh, Ahmad Shojaei, and Shahab Faghihi (2013). "Measurement of the uniaxial mechanical properties of healthy and atherosclerotic human coronary arteries". In: *Materials Science and Engineering: C* 33.5, pp. 2550–2554. ISSN: 0928-4931. DOI: `10.1016/j.msec.2013.02.016`. URL: `https://doi.org/10.1016/j.msec.2013.02.016`.

Kichula, E. T., H. Wang, S. M. Dorsey, S. E. Szczesny, D. M. Elliott, J. A. Burdick, and J. F. Wenk (2014). "Experimental and computational investigation of altered mechanical properties in myocardium after hydrogel injection". In: *Ann Biomed Eng* 42.7, pp. 1546–56. ISSN: 1573-9686 (Electronic) 0090-6964 (Print) 0090-6964 (Linking). DOI: `10.1007/s10439-013-0937-9`. URL: `https://www.ncbi.nlm.nih.gov/pubmed/24271262`.

Kofidis, T., D. R. Lebl, E. C. Martinez, G. Hoyt, M. Tanaka, and R. C. Robbins (2005). "Novel injectable bioartificial tissue facilitates targeted, less invasive, large-scale tissue restoration on the beating heart after myocardial injury". In: *Circulation* 112.9 Suppl, pp. I173–7. ISSN: 1524-4539 (Electronic) 0009-7322 (Linking). DOI: `10.1161/CIRCULATIONAHA.104.526178`. URL: `https://www.ncbi.nlm.nih.gov/pubmed/16159811`.

Kortsmit, Jeroen, Neil H. Davies, Renee Miller, J. R. Macadangdang, P. Zilla, and T. Franz (2013). "The effect of hydrogel injection on cardiac function and myocardial mechanics in a computational post-infarction model". In: *Comput Methods Biomech Biomed Engin* 16.11, pp. 1185–95. ISSN: 1476-8259 (Electronic) 1025-5842 (Linking). DOI: `10.1080/10255842.2012.656611`. URL: `https://www.ncbi.nlm.nih.gov/pubmed/22439799`.

Kortsmit, Jeroen, Neil H. Davies, Renee Miller, Peter Zilla, and Thomas Franz (2014). "Computational predictions of improved of wall mechanics and function of the infarcted left ventricle at early and late remodelling stages: comparison of layered and bulk hydrogel injectates". In: *Advances in biomechanics and applications* 1.1, pp. 41–55. ISSN: 2287-2094. DOI: `10.12989/aba.2013.1.1.041`.

Krishnamurthy, A., C. T. Villongco, J. Chuang, L. R. Frank, V. Nigam, E. Belezzuoli, P. Stark, D. E. Krummen, S. Narayan, J. H. Omens, A. D. McCulloch, and R. C. Kerckhoffs (2013). "Patient-Specific Models of Cardiac Biomechanics". In: *J Comput Phys* 244, pp. 4–21. ISSN: 0021-9991 (Print) 0021-9991 (Linking). DOI: `10.1016/j.jcp.2012.09.015`. URL: `https://www.ncbi.nlm.nih.gov/pubmed/23729839`.

Lamata, P., R. Casero, V. Carapella, S. A. Niederer, M. J. Bishop, J. E. Schneider, P. Kohl, and V. Grau (2014). "Images as drivers of progress in cardiac computational modelling". In: *Prog Biophys Mol Biol* 115.2-3, pp. 198–212. ISSN: 1873-1732 (Electronic) 0079-6107 (Print) 0079-6107 (Linking). DOI: `10.1016/j.pbiomolbio.2014.08.005`. URL: `https://www.ncbi.nlm.nih.gov/pubmed/25117497`.

Landa, N., L. Miller, M. S. Feinberg, R. Holbova, M. Shachar, I. Freeman, S. Cohen, and J. Leor (2008). "Effect of injectable alginate implant on cardiac remodeling and function after recent and old infarcts in rat". In: *Circulation* 117.11, pp. 1388–96. ISSN: 1524-4539 (Electronic) 0009-7322 (Linking). DOI: `10.1161/CIRCULATIONAHA.107.727420`. URL: `https://www.ncbi.nlm.nih.gov/pubmed/18316487`.

Le Visage, C., O. Gournay, N. Benguirat, S. Hamidi, L. Chaussumier, N. Mougenot, J. A. Flanders, R. Isnard, J. B. Michel, S. Hatem, D. Letourneur, and F. Norol (2012). "Mesenchymal stem cell delivery into rat infarcted myocardium using a porous polysaccharide-based scaffold: a quantitative comparison with endocardial injection". In: *Tissue Eng Part A* 18.1-2, pp. 35–44. ISSN: 1937-335X (Electronic) 1937-3341 (Print) 1937-3341 (Linking). DOI: `10.1089/ten.TEA.2011.0053`. URL: `https://www.ncbi.nlm.nih.gov/pubmed/21770864`.

Lee, L. C., S. T. Wall, M. Genet, A. Hinson, and J. M. Guccione (2014). "Bioinjection treatment: effects of post-injection residual stress on left ventricular wall stress". In: *J Biomech* 47.12, pp. 3115–9. ISSN: 1873-2380 (Electronic) 0021-9290 (Print) 0021-9290 (Linking). DOI: `10.1016/j.jbiomech.2014.06.026`. URL: `https://www.ncbi.nlm.nih.gov/pubmed/25065728`.

Legner, D., S. Skatulla, M. Bewu J, R. R. Rama, B. D. Reddy, C. Sansour, N. H. Davies, and T. Franz (2014). "Studying the influence of hydrogel injections into the infarcted left ventricle using the element-free Galerkin method". In: *Int J Numer Method Biomed Eng* 30.3, pp. 416–29. ISSN: 2040-7947 (Electronic) 2040-7939 (Linking). DOI: `10.1002/cnm.2610`. URL: `https://www.ncbi.nlm.nih.gov/pubmed/24574184`.

LeGrice, I. J., Y. Takayama, and J. W. Covell (1995). “Transverse Shear Along Myocardial Cleavage Planes Provides a Mechanism for Normal Systolic Wall Thickening”. In: *Circulation Research* 77.1, pp. 182–193. ISSN: 0009-7330. DOI: `10.1161/01.res.77.1.182`. URL: `https://doi.org/10.1161/01.res.77.1.182`.

Leor, J., S. Tuvia, V. Guetta, F. Manczur, D. Castel, U. Willenz, O. Petnehazy, N. Landa, M. S. Feinberg, E. Konen, O. Goitein, O. Tsur-Gang, M. Shaul, L. Klapper, and S. Cohen (2009). “Intracoronary injection of in situ forming alginate hydrogel reverses left ventricular remodeling after myocardial infarction in Swine”. In: *J Am Coll Cardiol* 54.11, pp. 1014–23. ISSN: 1558-3597 (Electronic) 0735-1097 (Linking). DOI: `10.1016/j.jacc.2009.06.010`. URL: `https://www.ncbi.nlm.nih.gov/pubmed/19729119`.

Li, L., F. Yu, L. Zheng, R. Wang, W. Yan, Z. Wang, J. Xu, J. Wu, D. Shi, L. Zhu, X. Wang, and Q. Jiang (2019). “Natural hydrogels for cartilage regeneration: Modification, preparation and application”. In: *J Orthop Translat* 17, pp. 26–41. ISSN: 2214-031X (Print) 2214-0328 (Electronic) 2214-031X (Linking). DOI: `10.1016/j.jot.2018.09.003`. URL: `https://www.ncbi.nlm.nih.gov/pubmed/31194006`.

Lin, C. C. and K. S. Anseth (2009). “PEG hydrogels for the controlled release of biomolecules in regenerative medicine”. In: *Pharm Res* 26.3, pp. 631–43. ISSN: 0724-8741 (Print) 1573-904X (Electronic) 0724-8741 (Linking). DOI: `10.1007/s11095-008-9801-2`. URL: `https://www.ncbi.nlm.nih.gov/pubmed/19089601`.

Lopez-Perez, A., R. Sebastian, and J. M. Ferrero (2015). “Three-dimensional cardiac computational modelling: methods, features and applications”. In: *Biomed Eng Online* 14, p. 35. ISSN: 1475-925X (Electronic) 1475-925X (Linking). DOI: `10.1186/s12938-015-0033-5`. URL: `https://www.ncbi.nlm.nih.gov/pubmed/25928297`.

Lu, W. N., S. H. Lu, H. B. Wang, D. X. Li, C. M. Duan, Z. Q. Liu, T. Hao, W. J. He, B. Xu, Q. Fu, Y. C. Song, X. H. Xie, and C. Y. Wang (2009). “Functional improvement of infarcted heart by co-injection of embryonic stem cells with temperature-responsive chitosan hydrogel”. In: *Tissue Eng Part A* 15.6, pp. 1437–47. ISSN: 1937-335X (Electronic) 1937-3341 (Linking). DOI: `10.1089/ten.tea.2008.0143`. URL: `https://www.ncbi.nlm.nih.gov/pubmed/19061432`.

Mackerle, J. (2005). “Finite element modelling and simulations in cardiovascular mechanics and cardiology: a bibliography 1993-2004”. In: *Comput Methods Biomech Biomed Engin* 8.2, pp. 59–81. ISSN: 1025-5842 (Print) 1025-5842 (Linking). DOI: `10.1080/10255840500141486`. URL: `https://www.ncbi.nlm.nih.gov/pubmed/16154871`.

Marino, Michele (2019). “Constitutive Modeling of Soft Tissues”. In: *Encyclopedia of Biomedical Engineering*, pp. 81–110. ISBN: 9780128051443. DOI: `10.1016/b978-0-12-801238-3.99926-4`.

Martino, M. M., P. S. Briquez, A. Ranga, M. P. Lutolf, and J. A. Hubbell (2013). “Heparin-binding domain of fibrin(ogen) binds growth factors and promotes tissue repair when incorporated within a synthetic matrix”. In: *Proc Natl Acad Sci U S A* 110.12, pp. 4563–8. ISSN: 1091-6490 (Electronic) 0027-8424 (Print) 0027-8424 (Linking). DOI: `10.1073/pnas.1221602110`. URL: `https://www.ncbi.nlm.nih.gov/pubmed/23487783`.

McGarvey, J. R., D. Mojsejenko, S. M. Dorsey, A. Nikou, J. A. Burdick, 3rd Gorman J. H., B. M. Jackson, J. J. Pilla, R. C. Gorman, and J. F. Wenk (2015). “Temporal Changes in Infarct Material Properties: An In Vivo Assessment Using Magnetic Resonance Imaging and Finite Element Simulations”. In: *Ann Thorac Surg* 100.2, pp. 582–9. ISSN: 1552-6259 (Electronic) 0003-4975 (Print) 0003-4975 (Linking). DOI: `10.1016/j.athoracsur.2015.03.015`. URL: `https://www.ncbi.nlm.nih.gov/pubmed/26095107`.

Miller, R., N. H. Davies, J. Kortsmit, P. Zilla, and T. Franz (2013). “Outcomes of myocardial infarction hydrogel injection therapy in the human left ventricle dependent on injectate distribution”. In: *Int J Numer Method Biomed Eng* 29.8, pp. 870–84. ISSN: 2040-7947 (Electronic) 2040-7939 (Linking). DOI: `10.1002/cnm.2551`. URL: `https://www.ncbi.nlm.nih.gov/pubmed/23640777`.

Miller, R., D. Marlevi, W. Zhang, M. Hirschvogel, M. Hadjicharalambous, A. Capilnasiu, M. Balmus, S. Hager, J. Jilberto, M. Bonini, A. Wittgenstein, Y. Ahmed, and D. Nordsletten (2022). “Modeling Biomechanics in the Healthy and Diseased Heart”. In: ISBN: 978-3-030-88083-5. DOI: `10.1007/978-3-030-88084-2_5`.

Morris, Paul D., Andrew Narracott, Hendrik von Tengg-Kobligk, Daniel Alejandro Silva Soto, Sarah Hsiao, Angela Lungu, Paul Evans, Neil W. Bressloff, Patricia V. Lawford, D. Rodney Hose, et al. (2016). “Computational fluid dynamics modelling in cardiovascular medicine”. In: *Heart* 102.1, pp. 18–28.

Motchon, Y. D., Kevin L. Sack, M. S. Sirry, M. Kruger, E. Pauwels, D. Van Loo, A. De Muynck, L. Van Hoorebeke, Neil H. Davies, and Thomas Franz (2023). “Effect of biomaterial stiffness on cardiac mechanics in a biventricular infarcted rat heart model with microstructural representation of in situ intramyocardial injectate". In: *International Journal for Numerical Methods in Biomedical Engineering* 39.5, e3693. DOI: `https://doi.org/10.1002/cnm.3693`. eprint: `https://onlinelibrary.wiley.com/doi/pdf/10.1002/cnm.3693`. URL: `https://onlinelibrary.wiley.com/doi/abs/10.1002/cnm.3693`.

Nakamuta, J. S., M. E. Danoviz, F. L. Marques, L. dos Santos, C. Becker, G. A. Goncalves, P. F. Vassallo, I. T. Schettert, P. J. Tucci, and J. E. Krieger (2009). "Cell therapy attenuates cardiac dysfunction post myocardial infarction: effect of timing, routes of injection and a fibrin scaffold". In: *PLoS One* 4.6, e6005. ISSN: 1932-6203 (Electronic) 1932-6203 (Linking). DOI: `10.1371/journal.pone.0006005`. URL: `https://www.ncbi.nlm.nih.gov/pubmed/19547700`.

Neal, M. L. and R. Kerckhoffs (2010). "Current progress in patient-specific modeling". In: *Brief Bioinform* 11.1, pp. 111–26. ISSN: 1477-4054 (Electronic) 1467-5463 (Print) 1467-5463 (Linking). DOI: `10.1093/bib/bbp049`. URL: `https://www.ncbi.nlm.nih.gov/pubmed/19955236`.

Nedkoff, Lee, Tom Briffa, Dawit Zemedikun, Saranne Herrington, and F. Lucy Wright (2023). "Global Trends in Atherosclerotic Cardiovascular Disease". In: *Clinical Therapeutics* 45.11, pp. 1087–1091. ISSN: 0149-2918. DOI: `10.1016/j.clinthera.2023.09.020`. URL: `https://doi.org/10.1016/j.clinthera.2023.09.020`.

Nelson, D. M., Z. Ma, K. L. Fujimoto, R. Hashizume, and W. R. Wagner (2011). "Intra-myocardial biomaterial injection therapy in the treatment of heart failure: Materials, outcomes and challenges". In: *Acta Biomater* 7.1, pp. 1–15. ISSN: 1878-7568 (Electronic) 1742-7061 (Print) 1742-7061 (Linking). DOI: `10.1016/j.actbio.2010.06.039`. URL: `https://www.ncbi.nlm.nih.gov/pubmed/20619368`.

Ngoepe, Malebogo, Andreas Passos, Stavroula Balabani, Jesse King, Anastasia Lynn, Jasanth Moodley, Liam Swanson, Deon Bezuidenhout, Neil H. Davies, and Thomas Franz (2019). "A Preliminary Computational Investigation Into the Flow of PEG in Rat Myocardial Tissue for Regenerative Therapy". In: *Frontiers in Cardiovascular Medicine* 6. ISSN: 2297-055X. DOI: `10.3389/fcvm.2019.00104`. URL: `https://www.frontiersin.org/journals/cardiovascular-medicine/articles/10.3389/fcvm.2019.00104`.

Nguyen, Danh, Olufemi Kadri, and Roman Voronov (2020). "An Introductory Overview of Image-Based Computational Modeling in Personalized Cardiovascular Medicine". In: *Frontiers in Bioengineering and Biotechnology* 8, p. 529365. DOI: `10.3389/fbioe.2020.529365`.

NHS (n.d.). *Primary percutaneous coronary intervention (PPCI).* Accessed: 2024-06-30. URL: `https://royalpapworth.nhs.uk/our-services/cardiology-services/cath-labs/primary-percutaneous-coronary-intervention-ppci`.

Nielsen, P. M., I. J. Le Grice, B. H. Smaill, and P. J. Hunter (1991). "Mathematical model of geometry and fibrous structure of the heart". In: *Am J Physiol* 260.4 Pt 2, H1365–78. ISSN: 0002-9513 (Print) 0002-9513 (Linking). DOI: `10.1152/ajpheart.1991.260.4.H1365`. URL: `https://www.ncbi.nlm.nih.gov/pubmed/2012234`.

Owen, B., N. Bojdo, A. Jivkov, B. Keavney, and A. Revell (2018). "Structural modelling of the cardiovascular system". In: *Biomech Model Mechanobiol* 17.5, pp. 1217–1242. ISSN: 1617-7940 (Electronic) 1617-7959 (Print) 1617-7940 (Linking). DOI: `10.1007/s10237-018-1024-9`. URL: `https://www.ncbi.nlm.nih.gov/pubmed/29911296`.

Place, E. S., J. H. George, C. K. Williams, and M. M. Stevens (2009). "Synthetic polymer scaffolds for tissue engineering". In: *Chem Soc Rev* 38.4, pp. 1139–51. ISSN: 0306-0012 (Print) 0306-0012 (Linking). DOI: `10.1039/b811392k`. URL: `https://www.ncbi.nlm.nih.gov/pubmed/19421585`.

Pollock, J. D. and A. N. Makaryus (2017). "Physiology, Cardiac Cycle". In: *StatPearls.* Treasure Island (FL): StatPearls Publishing Copyright © 2024, StatPearls Publishing LLC. URL: `https://europepmc.org/article/NBK/nbk459327`.

Pope, Adèle J., Gregory B. Sands, Bruce H. Smaill, and Ian J. LeGrice (2008). "Three-dimensional transmural organization of perimysial collagen in the heart". In: *American Journal of Physiology-Heart and Circulatory Physiology* 295.3, H1243–H1252. ISSN: 0363-6135. DOI: `10.1152/ajpheart.00484.2008`. URL: `https://doi.org/10.1152/ajpheart.00484.2008`.

Quarteroni, Alfio, Toni Lassila, Simone Rossi, and Riccardo Ruiz-Baier (2017). "Integrated Heart–Coupling multiscale and multiphysics models for the simulation of the cardiac function". In: *Computer Methods in Applied Mechanics and Engineering* 314, pp. 345–407. ISSN: 0045-7825. DOI: `https://doi.org/10.1016/j.cma.2016.05.031`. URL: `https://www.sciencedirect.com/science/article/pii/S0045782516304662`.

Rane, A. A., J. S. Chuang, A. Shah, D. P. Hu, N. D. Dalton, Y. Gu, K. L. Peterson, J. H. Omens, and K. L. Christman (2011). "Increased infarct wall thickness by a bio-inert material is insufficient to prevent negative left ventricular remodeling after myocardial infarction". In: *PLoS One* 6.6, e21571.

ISSN: 1932-6203 (Electronic) 1932-6203 (Linking). DOI: `10.1371/journal.pone.0021571`. URL: `https://www.ncbi.nlm.nih.gov/pubmed/21731777`.

Reddy, K., A. Khaliq, and Robert J. Henning (2015). “Recent advances in the diagnosis and treatment of acute myocardial infarction”. In: *World J Cardiol* 7.5, pp. 243–76. ISSN: 1949-8462 (Print) 1949-8462 (Electronic). DOI: `10.4330/wjc.v7.i5.243`. URL: `https://www.ncbi.nlm.nih.gov/pubmed/26015857`.

Reed, G. W., J. E. Rossi, and C. P. Cannon (2017). “Acute myocardial infarction”. In: *Lancet* 389.10065, pp. 197–210. ISSN: 1474-547X (Electronic) 0140-6736 (Linking). DOI: `10.1016/S0140-6736(16)30677-8`. URL: `https://www.ncbi.nlm.nih.gov/pubmed/27502078`.

Rodell, C. B., M. E. Lee, H. Wang, S. Takebayashi, T. Takayama, T. Kawamura, J. S. Arkles, N. N. Dusaj, S. M. Dorsey, W. R. Witschey, J. J. Pilla, 3rd Gorman J. H., J. F. Wenk, J. A. Burdick, and R. C. Gorman (2016). “Injectable Shear-Thinning Hydrogels for Minimally Invasive Delivery to Infarcted Myocardium to Limit Left Ventricular Remodeling”. In: *Circ Cardiovasc Interv* 9.10. ISSN: 1941-7632 (Electronic) 1941-7640 (Print) 1941-7640 (Linking). DOI: `10.1161/CIRCINTERVENTIONS.116.004058`. URL: `https://www.ncbi.nlm.nih.gov/pubmed/27729419`.

Rustad, K. C., V. W. Wong, M. Sorkin, J. P. Glotzbach, M. R. Major, J. Rajadas, M. T. Longaker, and G. C. Gurtner (2012). “Enhancement of mesenchymal stem cell angiogenic capacity and stemness by a biomimetic hydrogel scaffold”. In: *Biomaterials* 33.1, pp. 80–90. ISSN: 1878-5905 (Electronic) 0142-9612 (Print) 0142-9612 (Linking). DOI: `10.1016/j.biomaterials.2011.09.041`. URL: `https://www.ncbi.nlm.nih.gov/pubmed/21963148`.

Sabbah, H. N., M. Wang, R. C. Gupta, S. Rastogi, I. Ilsar, M. S. Sabbah, S. Kohli, S. Helgerson, and R. J. Lee (2013). “Augmentation of left ventricular wall thickness with alginate hydrogel implants improves left ventricular function and prevents progressive remodeling in dogs with chronic heart failure”. In: *JACC Heart Fail* 1.3, pp. 252–8. ISSN: 2213-1787 (Electronic) 2213-1779 (Print) 2213-1779 (Linking). DOI: `10.1016/j.jchf.2013.02.006`. URL: `https://www.ncbi.nlm.nih.gov/pubmed/23998003`.

Sack, Kevin L., E. Aliotta, D. B. Ennis, J. S. Choy, G. S. Kassab, J. M. Guccione, and T. Franz (2018). “Construction and Validation of Subject-Specific Biventricular Finite-Element Models of Healthy and Failing Swine Hearts From High-Resolution DT-MRI”. In: *Front Physiol* 9, p. 539. ISSN: 1664-042X (Print) 1664-042X (Electronic) 1664-042X (Linking). DOI: `10.3389/fphys.2018.00539`. URL: `https://www.ncbi.nlm.nih.gov/pubmed/29896107`.

Sack, Kevin L., Eric Aliotta, Jenny S. Choy, Daniel B. Ennis, Neil H. Davies, Thomas Franz, Ghassan S. Kassab, and Julius M. Guccione (2020). “Intra-myocardial alginate hydrogel injection acts as a left ventricular mid-wall constraint in swine”. In: *Acta Biomaterialia* 111, pp. 170–180. ISSN: 1742-7061. DOI: `10.1016/j.actbio.2020.04.033`. URL: `https://doi.org/10.1016/j.actbio.2020.04.033`.

Sack, Kevin L., N. H. Davies, J. M. Guccione, and T. Franz (2016). “Personalised computational cardiology: Patient-specific modelling in cardiac mechanics and biomaterial injection therapies for myocardial infarction”. In: *Heart Fail Rev* 21.6, pp. 815–826. ISSN: 1573-7322 (Electronic) 1382-4147 (Print) 1382-4147 (Linking). DOI: `10.1007/s10741-016-9528-9`. URL: `https://www.ncbi.nlm.nih.gov/pubmed/26833320`.

Saeb, Saba, Paul Steinmann, and Ali Javili (2016). “Aspects of computational homogenization at finite deformations: a unifying review from Reuss’ to Voigt’s bound”. In: *Applied Mechanics Reviews* 68.5, p. 050801.

Saludas, L., S. Pascual-Gil, F. Prosper, E. Garbayo, and M. Blanco-Prieto (2017). “Hydrogel based approaches for cardiac tissue engineering”. In: *Int J Pharm* 523.2, pp. 454–475. ISSN: 1873-3476 (Electronic) 0378-5173 (Linking). DOI: `10.1016/j.ijpharm.2016.10.061`. URL: `https://www.ncbi.nlm.nih.gov/pubmed/27989830`.

Sands, Gregory B., Dane A. Gerneke, Darren A. Hooks, Colin R. Green, Bruce H. Smaill, and Ian J. Legrice (2005). “Automated imaging of extended tissue volumes using confocal microscopy”. In: *Microscopy Research and Technique* 67.5, pp. 227–239. DOI: `https://doi.org/10.1002/jemt.20200`. eprint: `https://analyticalsciencejournals.onlinelibrary.wiley.com/doi/pdf/10.1002/jemt.20200`. URL: `https://analyticalsciencejournals.onlinelibrary.wiley.com/doi/abs/10.1002/jemt.20200`.

Sarig, U. and M. Machluf (2011). “Engineering cell platforms for myocardial regeneration”. In: *Expert Opin Biol Ther* 11.8, pp. 1055–77. ISSN: 1744-7682 (Electronic) 1471-2598 (Linking). DOI: `10.1517/14712598.2011.578574`. URL: `https://www.ncbi.nlm.nih.gov/pubmed/21542780`.

Sedlakova, V., S. Mourcos, J. Pupkaite, Y. Lunn, S. Visintini, I. Guzman-Soto, M. Ruel, E. Suuronen, and E. I. Alarcon (2024). “Biomaterials for direct cardiac repair-A rapid scoping review 2012-2022”.

In: *Acta Biomater* 180, pp. 61–81. ISSN: 1878-7568 (Electronic) 1742-7061 (Linking). DOI: `10.1016/j.actbio.2024.04.008`. URL: `https://www.ncbi.nlm.nih.gov/pubmed/38588997`.

Seif-Naraghi, S. B., J. M. Singelyn, M. A. Salvatore, K. G. Osborn, J. J. Wang, U. Sampat, O. L. Kwan, G. M. Strachan, J. Wong, P. J. Schup-Magoffin, R. L. Braden, K. Bartels, J. A. DeQuach, M. Preul, A. M. Kinsey, A. N. DeMaria, N. Dib, and K. L. Christman (2013). "Safety and efficacy of an injectable extracellular matrix hydrogel for treating myocardial infarction". In: *Sci Transl Med* 5.173, 173ra25. ISSN: 1946-6242 (Electronic) 1946-6234 (Print) 1946-6234 (Linking). DOI: `10.1126/scitranslmed.3005503`. URL: `https://www.ncbi.nlm.nih.gov/pubmed/23427245`.

Sepantafar, M., R. Maheronnaghsh, H. Mohammadi, S. Rajabi-Zeleti, N. Annabi, N. Aghdami, and H. Baharvand (2016). "Stem cells and injectable hydrogels: Synergistic therapeutics in myocardial repair". In: *Biotechnol Adv* 34.4, pp. 362–379. ISSN: 1873-1899 (Electronic) 0734-9750 (Linking). DOI: `10.1016/j.biotechadv.2016.03.003`. URL: `https://www.ncbi.nlm.nih.gov/pubmed/26976812`.

Singelyn, J. M., P. Sundaramurthy, T. D. Johnson, P. J. Schup-Magoffin, D. P. Hu, D. M. Faulk, J. Wang, K. M. Mayle, K. Bartels, M. Salvatore, A. M. Kinsey, A. N. Demaria, N. Dib, and K. L. Christman (2012). "Catheter-deliverable hydrogel derived from decellularized ventricular extracellular matrix increases endogenous cardiomyocytes and preserves cardiac function post-myocardial infarction". In: *J Am Coll Cardiol* 59.8, pp. 751–63. ISSN: 1558-3597 (Electronic) 0735-1097 (Print) 0735-1097 (Linking). DOI: `10.1016/j.jacc.2011.10.888`. URL: `https://www.ncbi.nlm.nih.gov/pubmed/22340268`.

Singh, R. K., D. Seliktar, and A. J. Putnam (2013). "Capillary morphogenesis in PEG-collagen hydrogels". In: *Biomaterials* 34.37, pp. 9331–40. ISSN: 1878-5905 (Electronic) 0142-9612 (Print) 0142-9612 (Linking). DOI: `10.1016/j.biomaterials.2013.08.016`. URL: `https://www.ncbi.nlm.nih.gov/pubmed/24021759`.

Sirry, Mazin S., Neil H. Davies, Karen Kadner, Laura Dubuis, Muhammad G. Saleh, Ernesta M. Meintjes, Bruce S. Spottiswoode, Peter Zilla, and Thomas Franz (2013). "Micro-structurally detailed model of a therapeutic hydrogel injectate in a rat biventricular cardiac geometry for computational simulations". In: *Computer Methods in Biomechanics and Biomedical Engineering* 18.3, pp. 325–331. ISSN: 1476-8259. DOI: `10.1080/10255842.2013.793765`.

Skaalure, S. C., S. O. Dimson, A. M. Pennington, and S. J. Bryant (2014). "Semi-interpenetrating networks of hyaluronic acid in degradable PEG hydrogels for cartilage tissue engineering". In: *Acta Biomater* 10.8, pp. 3409–20. ISSN: 1878-7568 (Electronic) 1742-7061 (Linking). DOI: `10.1016/j.actbio.2014.04.013`. URL: `https://www.ncbi.nlm.nih.gov/pubmed/24769116`.

Sommer, Gerhard, Andreas J. Schriefl, Michaela Andrä, Michael Sacherer, Christian Viertler, Heimo Wolinski, and Gerhard A. Holzapfel (2015). "Biomechanical properties and microstructure of human ventricular myocardium". In: *Acta Biomaterialia* 24, pp. 172–192. ISSN: 1742-7061. DOI: `https://doi.org/10.1016/j.actbio.2015.06.031`. URL: `https://www.sciencedirect.com/science/article/pii/S1742706115300039`.

Souza Neto, E. A. de, P. J. Blanco, P. J. Sánchez, and R. A. Feijóo (2015). "An RVE-based multiscale theory of solids with micro-scale inertia and body force effects". In: *Mechanics of Materials* 80, pp. 136–144. ISSN: 0167-6636. DOI: `https://doi.org/10.1016/j.mechmat.2014.10.007`.

Statistics South Africa (2024). *Mortality and causes of death in South Africa, 2020: Findings from death notification.* STATISTICAL RELEASE P0309.3. URL: `https://www.statssa.gov.za/publications/P03093/P030932020.pdf`.

Stevens, C. and P. J. Hunter (2003). "Sarcomere length changes in a 3D mathematical model of the pig ventricles". In: *Prog Biophys Mol Biol* 82.1-3, pp. 229–41. ISSN: 0079-6107 (Print) 0079-6107 (Linking). DOI: `10.1016/s0079-6107(03)00023-3`. URL: `https://www.ncbi.nlm.nih.gov/pubmed/12732282`.

Streeter D. D., Jr. and W. T. Hanna (1973). "Engineering mechanics for successive states in canine left ventricular myocardium. II. Fiber angle and sarcomere length". In: *Circ Res* 33.6, pp. 656–64. ISSN: 0009-7330 (Print) 0009-7330 (Linking). DOI: `10.1161/01.res.33.6.656`. URL: `https://www.ncbi.nlm.nih.gov/pubmed/4762007`.

Thygesen, K., J. S. Alpert, A. S. Jaffe, B. R. Chaitman, J. J. Bax, D. A. Morrow, H. D. White, and Infarction Executive Group on behalf of the Joint European Society of Cardiology /American College of Cardiology /American Heart Association /World Heart Federation Task Force for the Universal Definition of Myocardial (2018). "Fourth Universal Definition of Myocardial Infarction (2018)". In: *Circulation* 138.20, e618–e651. ISSN: 1524-4539 (Electronic) 0009-7322 (Linking). DOI: `10.1161/CIR.0000000000000617`. URL: `https://www.ncbi.nlm.nih.gov/pubmed/30571511`.

Torquato, Salvatore et al. (2002). *Random heterogeneous materials: microstructure and macroscopic properties.* Vol. 16. Springer.

Tous, E., B. Purcell, J. L. Ifkovits, and J. A. Burdick (2011). "Injectable acellular hydrogels for cardiac repair". In: *J Cardiovasc Transl Res* 4.5, pp. 528–42. ISSN: 1937-5395 (Electronic) 1937-5387 (Linking). DOI: `10.1007/s12265-011-9291-1`. URL: `https://www.ncbi.nlm.nih.gov/pubmed/21710332`.

Trayanova, Natalia, Aurore Lyon, Julie Shade, and Jordi Heijman (2023). "Computational modeling of cardiac electrophysiology and arrhythmogenesis". In: *Physiological Reviews* 104. DOI: `10.1152/physrev.00017.2023`.

Wall, S. T., J. C. Walker, K. E. Healy, M. B. Ratcliffe, and J. M. Guccione (2006). "Theoretical impact of the injection of material into the myocardium: a finite element model simulation". In: *Circulation* 114.24, pp. 2627–35. ISSN: 1524-4539 (Electronic) 0009-7322 (Linking). DOI: `10.1161/CIRCULATIONAHA.106.657270`. URL: `https://www.ncbi.nlm.nih.gov/pubmed/17130342`.

Wang, H., C. B. Rodell, M. E. Lee, N. N. Dusaj, 3rd Gorman J. H., J. A. Burdick, R. C. Gorman, and J. F. Wenk (2017). "Computational sensitivity investigation of hydrogel injection characteristics for myocardial support". In: *J Biomech* 64, pp. 231–235. ISSN: 1873-2380 (Electronic) 0021-9290 (Print) 0021-9290 (Linking). DOI: `10.1016/j.jbiomech.2017.08.024`. URL: `https://www.ncbi.nlm.nih.gov/pubmed/28888476`.

Wang, L. L., Y. Liu, J. J. Chung, T. Wang, A. C. Gaffey, M. Lu, C. A. Cavanaugh, S. Zhou, R. Kanade, P. Atluri, E. E. Morrisey, and J. A. Burdick (2017). "Local and sustained miRNA delivery from an injectable hydrogel promotes cardiomyocyte proliferation and functional regeneration after ischemic injury". In: *Nat Biomed Eng* 1, pp. 983–992. ISSN: 2157-846X (Print) 2157-846X (Electronic) 2157-846X (Linking). DOI: `10.1038/s41551-017-0157-y`. URL: `https://www.ncbi.nlm.nih.gov/pubmed/29354322`.

Wang, T., X. J. Jiang, T. Lin, S. Ren, X. Y. Li, X. Z. Zhang, and Q. Z. Tang (2009a). "The inhibition of postinfarct ventricle remodeling without polycythaemia following local sustained intramyocardial delivery of erythropoietin within a supramolecular hydrogel". In: *Biomaterials* 30.25, pp. 4161–7. ISSN: 1878-5905 (Electronic) 0142-9612 (Linking). DOI: `10.1016/j.biomaterials.2009.04.033`. URL: `https://www.ncbi.nlm.nih.gov/pubmed/19539990`.

Wang, T., D. Q. Wu, X. J. Jiang, X. Z. Zhang, X. Y. Li, J. F. Zhang, Z. B. Zheng, R. Zhuo, H. Jiang, and C. Huang (2009b). "Novel thermosensitive hydrogel injection inhibits post-infarct ventricle remodelling". In: *Eur J Heart Fail* 11.1, pp. 14–9. ISSN: 1388-9842 (Print) 1388-9842 (Linking). DOI: `10.1093/eurjhf/hfn009`. URL: `https://www.ncbi.nlm.nih.gov/pubmed/19147452`.

Wann, S. and J. Tunio (2010). "Current challenges and future directions in cardiac imaging". In: *J Saudi Heart Assoc* 22.3, pp. 121–4. ISSN: 1016-7315 (Print) 2212-5043 (Electronic) 1016-7315 (Linking). DOI: `10.1016/j.jsha.2010.04.010`. URL: `https://www.ncbi.nlm.nih.gov/pubmed/23960604`.

Wassenaar, J. W., R. Gaetani, J. J. Garcia, R. L. Braden, C. G. Luo, D. Huang, A. N. DeMaria, J. H. Omens, and K. L. Christman (2016). "Evidence for Mechanisms Underlying the Functional Benefits of a Myocardial Matrix Hydrogel for Post-MI Treatment". In: *J Am Coll Cardiol* 67.9, pp. 1074–1086. ISSN: 1558-3597 (Electronic) 0735-1097 (Print) 0735-1097 (Linking). DOI: `10.1016/j.jacc.2015.12.035`. URL: `https://www.ncbi.nlm.nih.gov/pubmed/26940929`.

Wenk, J. F., P. Eslami, Z. Zhang, C. Xu, E. Kuhl, 3rd Gorman J. H., J. D. Robb, M. B. Ratcliffe, R. C. Gorman, and J. M. Guccione (2011). "A novel method for quantifying the in-vivo mechanical effect of material injected into a myocardial infarction". In: *Ann Thorac Surg* 92.3, pp. 935–41. ISSN: 1552-6259 (Electronic) 0003-4975 (Print) 0003-4975 (Linking). DOI: `10.1016/j.athoracsur.2011.04.089`. URL: `https://www.ncbi.nlm.nih.gov/pubmed/21871280`.

Wenk, J. F., S. T. Wall, R. C. Peterson, S. L. Helgerson, H. N. Sabbah, M. Burger, N. Stander, M. B. Ratcliffe, and J. M. Guccione (2009). "A method for automatically optimizing medical devices for treating heart failure: designing polymeric injection patterns". In: *J Biomech Eng* 131.12, p. 121011. ISSN: 1528-8951 (Electronic) 0148-0731 (Linking). DOI: `10.1115/1.4000165`. URL: `https://www.ncbi.nlm.nih.gov/pubmed/20524734`.

Williams, C., E. Budina, W. L. Stoppel, K. E. Sullivan, S. Emani, S. M. Emani, and 3rd Black L. D. (2015). "Cardiac extracellular matrix-fibrin hybrid scaffolds with tunable properties for cardiovascular tissue engineering". In: *Acta Biomater* 14, pp. 84–95. ISSN: 1878-7568 (Electronic) 1742-7061 (Print) 1742-7061 (Linking). DOI: `10.1016/j.actbio.2014.11.035`. URL: `https://www.ncbi.nlm.nih.gov/pubmed/25463503`.

Wilson, Alexander J., Gregory B. Sands, Ian J. LeGrice, Alistair A. Young, and Daniel B. Ennis (2022). "Myocardial mesostructure and mesofunction". In: *American Journal of Physiology-Heart and Circulatory Physiology* 323.2, H257–H275. ISSN: 1522-1539. DOI: `10.1152/ajpheart.00059.2022`. URL: `http://dx.doi.org/10.1152/ajpheart.00059.2022`.

Wise, P., N. H. Davies, M. S. Sirry, J. Kortsmit, L. Dubuis, C. K. Chai, F. P. Baaijens, and T. Franz (2016). “Excessive volume of hydrogel injectates may compromise the efficacy for the treatment of acute myocardial infarction”. In: *Int J Numer Method Biomed Eng* 32.12. ISSN: 2040-7947 (Electronic) 2040-7939 (Linking). DOI: `10.1002/cnm.2772`. URL: `https://www.ncbi.nlm.nih.gov/pubmed/26822845`.

World Health Organization (2021). *Cardiovascular diseases (CVDs).* Accessed: 2024-06-30. URL: `https://www.who.int/news-room/fact-sheets/detail/cardiovascular-diseases-(cvds)`.

World Heath Organization (2022). *WHO Mortality Database.* URL: `https://platform.who.int/mortality/countries/country-details/MDB/south-africa?countryProfileId=52258f2a-d18a-4217-a3ef-f189ae33bb7a`.

Wu, J., F. Zeng, X. P. Huang, J. C. Chung, F. Konecny, R. D. Weisel, and R. K. Li (2011). “Infarct stabilization and cardiac repair with a VEGF-conjugated, injectable hydrogel”. In: *Biomaterials* 32.2, pp. 579–86. ISSN: 1878-5905 (Electronic) 0142-9612 (Linking). DOI: `10.1016/j.biomaterials.2010.08.098`. URL: `https://www.ncbi.nlm.nih.gov/pubmed/20932570`.

Wu, Tengling and Wenguang Liu (2022). “Functional hydrogels for the treatment of myocardial infarction”. In: *NPG Asia Materials* 14.1. ISSN: 1884-4049 1884-4057. DOI: `10.1038/s41427-021-00330-y`.

Xu, G., X. Wang, C. Deng, X. Teng, E. J. Suuronen, Z. Shen, and Z. Zhong (2015). “Injectable biodegradable hybrid hydrogels based on thiolated collagen and oligo(acryloyl carbonate)-poly(ethylene glycol)-oligo(acryloyl carbonate) copolymer for functional cardiac regeneration”. In: *Acta Biomater* 15, pp. 55–64. ISSN: 1878-7568 (Electronic) 1742-7061 (Linking). DOI: `10.1016/j.actbio.2014.12.016`. URL: `https://www.ncbi.nlm.nih.gov/pubmed/25545323`.

Yan, Wenjun, Yunlong Xia, Huishou Zhao, Xiaoming Xu, Xinliang Ma, and Ling Tao (2024). “Stem cell-based therapy in cardiac repair after myocardial infarction: Promise, challenges, and future directions”. In: *Journal of Molecular and Cellular Cardiology* 188, pp. 1–14. ISSN: 0022-2828. DOI: `10.1016/j.yjmcc.2023.12.009`. URL: `https://doi.org/10.1016/j.yjmcc.2023.12.009`.

Yvonnet, Julien (2019). *Computational homogenization of heterogeneous materials with finite elements.* Vol. 258. Springer.

Zhu, D., Z. Li, K. Huang, T. G. Caranasos, J. S. Rossi, and K. Cheng (2021). “Minimally invasive delivery of therapeutic agents by hydrogel injection into the pericardial cavity for cardiac repair”. In: *Nat Commun* 12.1, p. 1412. ISSN: 2041-1723 (Electronic) 2041-1723 (Linking). DOI: `10.1038/s41467-021-21682-7`. URL: `https://www.ncbi.nlm.nih.gov/pubmed/33658506`.

Zhu, Y., Y. Matsumura, and W. R. Wagner (2017). “Ventricular wall biomaterial injection therapy after myocardial infarction: Advances in material design, mechanistic insight and early clinical experiences”. In: *Biomaterials* 129, pp. 37–53. ISSN: 1878-5905 (Electronic) 0142-9612 (Print) 0142-9612 (Linking). DOI: `10.1016/j.biomaterials.2017.02.032`. URL: `https://www.ncbi.nlm.nih.gov/pubmed/28324864`.